공학박사 학위논문

Integrated Fluid-Structure Simulation for Coupled Phenomena of a Solid Propellant Rocket Interior

고체 로켓 연소실 내부 복합 현상에 대한 유체-구조 연성 해석

2014년 2월

서울대학교 대학원

기계항공공학부

한 상 호

Integrated Fluid-Structure Simulation for Coupled Phenomena of a Solid Propellant Rocket Interior

고체 로켓 연소실 내부 복합 현상에 대한 유체-구조 연성 해석

지도교수 김 종 암

이 논문을 공학박사 학위논문으로 제출함
2013 년 12 월

서울대학교 대학원
기계항공공학부
한 상 호

한상호의 공학박사 학위논문을 인준함
2013 년 12월

위 원 장 鄭仁碩 (인)
부위원장 金鍾岩 (인)
위　　원 金奎弘 (인)
위　　원 吳鍾倫 (인)
위　　원 李知浩 (인)

Abstract

Integrated Fluid-Structure Simulation for Coupled Phenomena of a Solid Propellant Rocket Interior

Han, Sangho
School of Mechanical and Aerospace Engineering
The Graduate School
Seoul National University

The interior phenomena in solid rocket exhibit highly unsteady, multi-scale, and multi-physics features because fluid, structure, and combustion generate a non-linear feedback cycle by influencing one another inside the combustion chamber. In order to integrated fluid-structure-combustion simulation to understand the highly unsteady, multi-physics phenomena inside of solid rocket motor interior, fully integrated computational simulations inside solid propellant rocket are carried out to examine the nonlinear feedback interaction between fluid, structure and combustion module. The Arbitrary Lagrangian Eulerian (ALE) description is employed to efficiently tracking the burning process along grain surface. An automatic re-meshing algorithm is added to the FSbI process to accurately analyze unsteady fluid-structure coupling phenomena with deforming solid grain during simulation. The developed solver is then applied to the full-burning simulation of a solid propellant grain, which is a highly-coupled unsteady phenomenon between gas flow and propellant structure. Based on the integrated computed results, detailed ignition mechanism and flame propagation process along propellant grain surface are investigated. In particular, flame propagation delay and secondary burning phenomena are explained from the physical and numerical perspectives. Furthermore, virtual contact line method is introduced to overcome the boots contact problem occurring in the gas flow-propellant interaction, and the deforming behavior of full-burning solid propellant is examined.

Keywords: Solid propellant rocket, Fluid-structure interaction, Arbitrary Lagrangian-Eulerian method, Common-refinement data transfer, Dynamic mesh treatment

Student Number: 2007-30203
Name: Han, Sangho

Table of Contents

공학박사 학위논문 1
ABSTRACT I
NOMENCLATURE V
LIST OF TABLES VIII
LIST OF FIGURES IX
CHAPTER I 1
INTRODUCTION 1
1.1 Fluid-structure simulation for solid rocket interior 1
1.2 Dissertation Objectives: A Summary 5
1.3 Outline of Dissertation 6
CHAPTER II 7
NUMERICAL METHOD I 7
2.1 The arbitrary Lagrangian-Eulerian method 7
2.2 Descriptions of motion 11
2.3 The fundamental ALE equation 19
2.4 The ALE forms of governing equations 25
CHAPTER III 28
NUMERICAL METHODS II 28
3.1 Fluid solver 28
3.2 Structural solver 46
3.3 Combustion solver 51
3.4 Spatial and temporal data transfer scheme 56
3.5 Dynamic mesh treatment 59
3.6 Surface regression model 60
3.7 Virtual contact line method 62
CHAPTER IV 65

SIMULATION RESULTS..65

4.1 Validation problem..65

4.2 Validation problem..70

4.3 Rocket modeling and thermal analysis..76

4.4 Rocket simulation results..81

CHAPTER V...106

CONCLUDING REMARKS & FUTURE WORKS..............................106

5.1 Concluding Remarks..106

5.2 Future work..107

APPENDIX..108

A1. Common refinement data transfer scheme for 3-D rocket...........108

REFERENCES...121

국문 초록...132

Nomenclature

χ = the coordinate of referential domain

ρ = density

c = relative velocity between material velocity and mesh velocity

v = velocity of flow particle

E = total energy of flow particle

σ = Cauchy stress tensor

b = specific body force

ξ = coordinate of reference domain

u = magnitude of displacement of reference domain

$\hat{u}$ = magnitude of displacement of referential domain

$\frac{\partial u}{\partial X}$ = the displacement vector

$\frac{\partial \widehat{X}}{\partial t}$ = the mesh velocity

$\hat{X}$ = mapping function of mesh motion

C_{ijkl} = elastic constant

f = applied external force

F = inviscid flux vectors

G = viscous flux vectors

v_x = x-directional velocity component of fluid particle

v_y = y-directional velocity component of fluid particle

τ_f = shear stress tensor of fluid particle

λ_i = principal stretch

σ_0^n = elastic component of stress

h_j^n = visco-elastic stress contribution of the *j-th* Maxwell element

τ = the ratio of the damping to the spring coefficient

γ_j = the ratio of the Maxwell device modulus

c_p = the specific heat

M = the mass flux per unit area of solid propellant

λ_s = the thermal conductivity of propellant

h = the film coefficient of propellant surface

T_e = temperature of fluid domain at fluid-solid interface

T_s = the temperature of solid surface at fluid-solid interface

T_* = the flame temperature

T_*^0 = the adiabatic flame temperature

r_{bs} = the steady state burning rate

p_{ref} = the reference pressure for burning rate calculation

t_s = traction of solid surface at fluid-solid interface

t_f = traction of fluid surface at fluid-solid interface

List of Tables

Table 4.1 Propellant burning properties of TPEM rocket motor
Table 4.2 Boundary condition for FSbI analysis
Table 4.3 Material properties of solid propellant
Table A.1 Comparison of relative time cost

List of Figures

Figure 1.1	The component of solid rocket motor
Figure 1.2	The concept of FSI simulation procedure for solid rocket interior phenomena
Figure 2.1	One dimensional example of Lagrangian, Eulerian and ALE mesh and particle motion
Figure 2.2	Lagrangian versus ALE description
Figure 2.3	Lagrangian description of motion
Figure 2.4	The motion of the ALE computational mesh is independent of the material motion.
Figure 3.1	Combustion area locates between solid and fluid interface.
Figure 3.2	The difference of boundary conditions of fluid region: pre-ignited wall condition versus ignited mass flow rate condition
Figure 3.3	Loosely coupled scheme and strong coupled scheme for FSI time marching
Figure 3.4	Conventional serial staggered procedure
Figure 3.5	Solid domain with corners
Figure 3.6	(a) problem of convex corner (b) re-positioning concept of regression model
Figure 3.7	Virtual contact line
Figure 3.8	Integration flow chart for FSI rocket simulation
Figure 4.1	Geometry of panel flutter and non-matching fluid-solid interface
Figure 4.2	Theoretical result of stability boundary (Nelson and Cunningham, Ref. 28)
Figure 4.3	Numerical results: dynamics response at the panel center

Figure 4.4 Geometric shape of TPEM solid rocket motor
Figure 4.5 Flame propagation process of TPEM rocket motor
Figure 4.6 FSbI simulation results of TPEM motor (displacement legend for structural contour
Figure 4.7 Full-burning shape of contained propellant
Figure 4.8 Pressure history between experimental data and numerical results
Figure 4.9 Rocket geometry for simulation
Figure 4.10 Relaxation curves of solid propellant
Figure 4.11 Numerical results: comparison of thermal analysis
Figure 4.12 Numerical results: geometrical change of the boots' part due to thermal deformation
Figure 4.13 Numerical results: ignition, flame propagation, and flow development process in combustion chamber (inviscid flow solver)
Figure 4.14 Numerical results: FSbI simulation with viscous flow solver
Figure 4.15 Numerical results: comparison at the same time of Euler and N-S results
Figure 4.16 Numerical results: jet plume size comparisons
Figure 4.17 Numerical results: igniter outlet comparison at the same time of Euler and N-S result
Figure 4.18 Numerical results: flame propagation delay around the corners
Figure 4.19 Numerical results: flow separation near boots' entrance and secondary burning on inclined grain surface
Figure 4.20 Numerical results: flame propagation near the boots' entrance using inviscid flow solver
Figure 4.21 Numerical results: locations of measurement & density history in the chamber

Figure 4.22 Numerical results: FSbI simulation with viscous flow solver
Figure 4.23 Numerical results: pressure development history during the ignition phase
Figure 4.24 Numerical results: Mach number, temperature, and pressure contour at the chamber forehead
Figure 4.25 Numerical results: history of structural displacement
Figure 4.26 Numerical results: the boots' contact problem
Figure 4.27 Virtual contact line
Figure 4.28 Numerical results: structural deformation contour of propellant grain
Figure 4.29 Numerical results: pressure history in the chamber during the FSbI simulation
Figure 4.30 Numerical results: steady-state flow variable contours in the combustion chamber
Figure 4.31 Numerical results: geometric changes process of propellant grain and fluidic domain
Figure A.1 General procedure of common-refinement method
Figure A.2 Subfacets on a common surface
Figure A.3 Constructing subfacets process
Figure A.4 Subfacet triangulation process
Figure A.5 Example of making common-refinement surface
Figure A.6 Mesh condition for validation case
Figure A.7 Comparison of relative errors (left), Contour of peak function after repetitive data transfer (right, solid : exact solution , dashed : numerical result)
Figure A.8 Data transfer results

Figure A.9 Comparison of relative errors(left), comparison of conservation errors(right)
Figure A.10 Non-matching geometry of solid propellant rocket interior
Figure A.11 Comparison of L2 & Sobolev minimization test (a) L2 minimization (b) Sobolev minimization
Figure A.12 Data transfer results
Figure A.13 Comparison of relative errors (left), comparison of conservation errors (right)

Chapter I

INTRODUCTION

1.1 Fluid-structure simulation for solid rocket interior

Solid propellant rockets produce thrust force by burning contained propellant grain in combustion chamber, and by ejecting high-speed gas through supersonic nozzle. Due to the nonlinear visco-elastic behavior of propellant grain and the hot exhaustion gas formed during burning process, complex multi-physical phenomena occur in the interior of combustion chamber during ignition process [1].

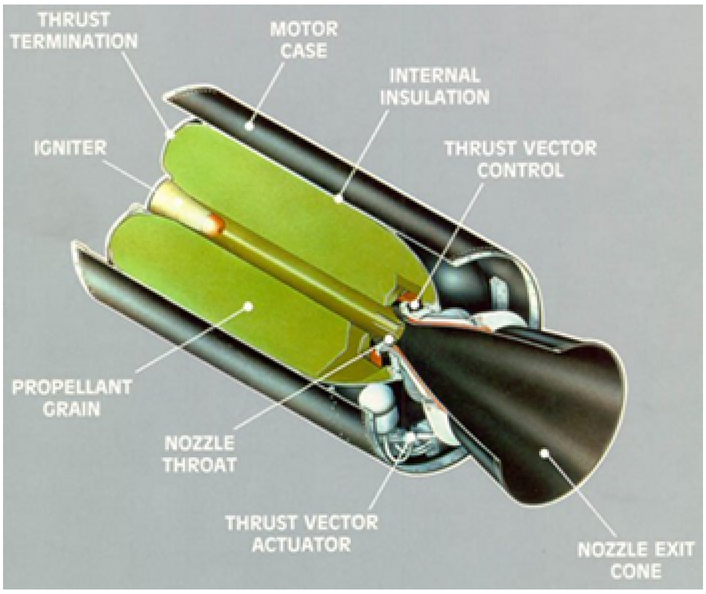

Figure 1.1 The component of solid rocket motor

(https://engineering.purdue.edu/~propulsi/propulsion/rockets/solids.html)

At the early stage of ignition, deformation of propellant grain is observed near igniter. Soon thereafter, a high-pressure flow, is explosively generated by flame propagation along the entire grain surface, imposes severe structural load on the solid propellant, and the grain becomes globally deformed. In addition, the burning process of the grain surface reduces the volume of the contained propellant and changes its shape [2]. Thus, it is extremely complicated to accurately predict the deformed shape of the propellant grain during combustion process. Additionally, the volumetric deformation of the propellant grain leads to a change of fluid domain, and flow characteristics are significantly varied. The flow characteristics due to burning process and domain deformation trigger a change in burning rate and pressure distribution on the propellant surface. Consequently, major factors governing the multi-physics inside solid rocket are the high-temperature and high-pressure gas flow, the structural deformation of the propellant grain, and the combustion process between the gas flow and the propellant. Each module (fluid, structure, and combustion) generates a non-linear feedback cycle by influencing one another. As a result, the interior phenomena in solid rocket exhibit highly unsteady, multi-scale, and multi-physics features. Such multi-physical process takes place during a very short period after ignition, and most of the unexpected abnormal accidents leading to fatal malfunction (for example, crack development, deflagration to detonation transition, and so on) occur at this period [3]. Thus, an in-depth understanding on the multi-physical behavior inside rocket combustion chamber is extremely important.

Due to physical complexity and strong interactions among multiple disciplines, much of the previous researches have been heavily dependent on experiments, while numerical analyses have been conducted to show some limited feature around specific physical region [4-6]. Experimental research, however, can be dangerous and expensive to perform, and it is not easy to measure all physical quantities that are necessary to investigate the physical phenomena inside rocket motor. On the other hand, most of the previous numerical researches mainly focused on unveiling single physics that is highly restrictive in understanding physical phenomena as a whole [7, 8]. This manifests the necessity of an integrated simulation by coupling fluid, structure and combustion. From this perspective, the present dissertation intends to develop an integrated analysis solver by coupling fluid, structure and combustion module to understand the unsteady features in combustion chamber and to investigate the multi-physical phenomena taking place inside the chamber during solid rocket operation [9, 10].

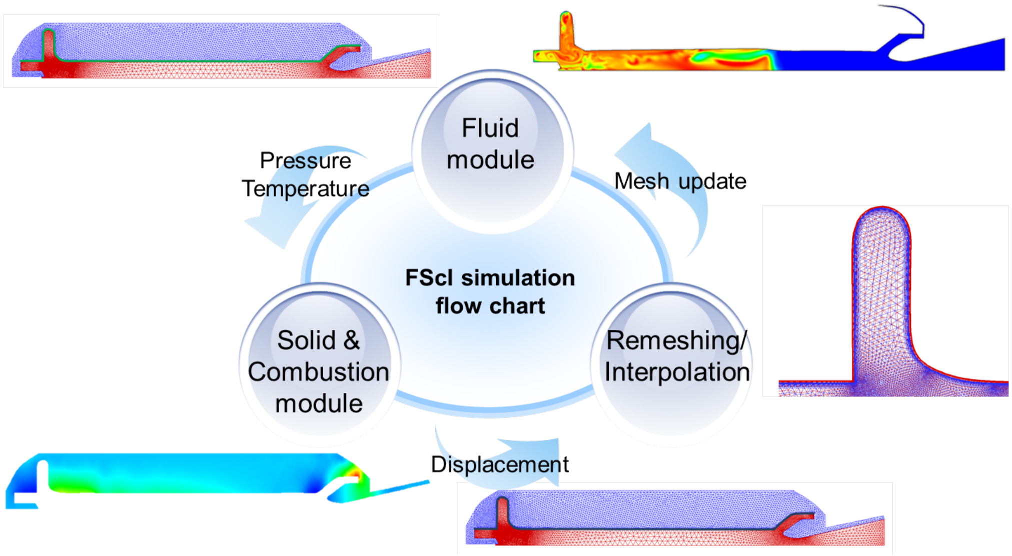

Figure 1.2 The concept of FSI simulation procedure for solid rocket interior phenomena

In order to develop the integrated analysis solver, key numerical components are firstly developed. The Arbitrary Lagrangian Eulerian (ALE) kinematical description, which combines the advantages of classical Lagrangian and Eulerian ones, is adopted for the clear delineation of dynamic fluid-structure surface. A 2-D axisymmetric unstructured code based on the ALE formulation is developed as a flow solver, and the ALE-based, nonlinear elastic/visco-elastic code is also developed for structure module. A 1-D based transient burning model and regression model are adopted to efficiently simulate the combustion process along the propellant-fluid boundary. In addition, a robust and efficient automatic re-meshing program is developed to handle deformable geometry while maintaining the initial mesh quality. A data transfer scheme along the non-matching interfaces between fluid and solid interface is also implemented. Each fluid, structure and combustion module is combined by a staggered time-marching procedure. The integrated program is then applied to the simulation of a 2-D axisymmetric solid rocket interior model including a pyrogen type igniter. Computational results are presented to show the burning process and characteristics along the propellant grain surface, the flow development process inside combustion chamber, and the structural deformation and burnback tendency of the propellant grain from the initial to the full burning state.

1.2 Dissertation Objectives: A Summary

In order to develop the integrated analysis solver, key numerical components are firstly developed. The Arbitrary Lagrangian Eulerian (ALE) kinematical description, which combines the advantages of classical Lagrangian and Eulerian ones, is adopted for the clear delineation of dynamic fluid-structure surface. A 2-D axisymmetric unstructured code based on the ALE formulation is developed as a flow solver, and the ALE-based, nonlinear elastic/visco-elastic code is also developed for structure module. A 1-D based transient burning model and regression model are adopted to efficiently simulate the combustion process along the propellant-fluid boundary. In addition, a robust and efficient automatic re-meshing program is developed to handle deformable geometry while maintaining the initial mesh quality. A data transfer scheme along the non-matching interfaces between fluid and solid interface is also implemented. Each fluid, structure and combustion module is combined by a staggered time-marching procedure. The integrated program is then applied to the simulation of a 2-D axisymmetric solid rocket interior model including a pyrogen type igniter. Computational results are presented to show the burning process and characteristics along the propellant grain surface, the flow development process inside combustion chamber, and the structural deformation and burnback tendency of the propellant grain from the initial to the full burning state.

1.3 Outline of Dissertation

After introduction about complex coupled physics inside chamber and fluid-structure interaction simulation, the basic ideas of arbitrary Lagrnagian-Eulerian method, a hybrid approach combining the advantages of the Lagrangian and Eulerian formulations, are introduced with classical kinematical description and the changes of governing equations in chapter 2.

The chapter 3 explains various numerical schemes and techniques which are used in fluid-structure interaction simulation considering combustion effect of solid propellant. Firstly, numerical schemes used for the fluid analysis modules are shown. Secondly, the structural analysis method, non-linear hyper-elastic model and visco-elastic model, is explained. After that, the combustion model, the virtual 1-D burning model is described briefly. Data transfer schemes and temporal integrated schemes use in the coupling simulations would be follows. Finally, a mesh automation technique and a handling of surface mesh node are explained.

The chapter 4 contains numerical simulation results. Firstly, the validation problem for FSI capability (panel flutter) will be shown. After then, at the solid rocket modelling and thermal analysis results will be explained. Finally, conclusions of this dissertation and some suggestion for future work are given in chapter 5.

Chapter II

NUMERICAL METHOD I

2.1 The arbitrary Lagrangian-Eulerian method

The numerical simulation of multi-dimensional and multi-physics problems in fluid dynamics and nonlinear solid mechanics often requires coping with strong distortions of the continuum under consideration while allowing for a clear delineation of free surfaces and fluid–fluid, solid–solid, or fluid–structure interfaces. A fundamentally important consideration when developing a computer aided analysis program for simulating problems in this class is the choice of an appropriate kinematical description of the continuum. In fact, such a choice determines the relationship between the deforming continuum, the finite grid and mesh of computing zones, and thus conditions the ability of the numerical method to deal with large distortions and provide an accurate resolution of material interfaces and moving boundaries.

The algorithms of continuum mechanics usually make use of two classical descriptions of motion: the Lagrangian description and the Eulerian description. The arbitrary Lagrangian–Eulerian (ALE, in short) description was developed in an attempt to combine the advantages of the above classical kinematical descriptions, while minimizing their respective drawbacks as far as possible. Lagrangian algorithms, in which each individual node of the computational mesh follows the associated material particle during motion (Figure 2.1), are mainly used in structural mechanics. The Lagrangian description allows an easy tracking of free surfaces and interfaces between different materials. It also facilitates the treatment of materials with history-dependent constitutive relations. Its weakness is its inability to follow large distortions of the computational domain without recourse to frequent remeshing operations. Eulerian algorithms are widely used in fluid dynamics. Here, as shown in Figure 2.1, the computational mesh is fixed and the continuum moves with respect to the grid. In the Eulerian description, large distortions in the continuum motion can be handled with relative ease, but generally at the expense of precise interface definition and the resolution of flow details. [12,13,48-51]

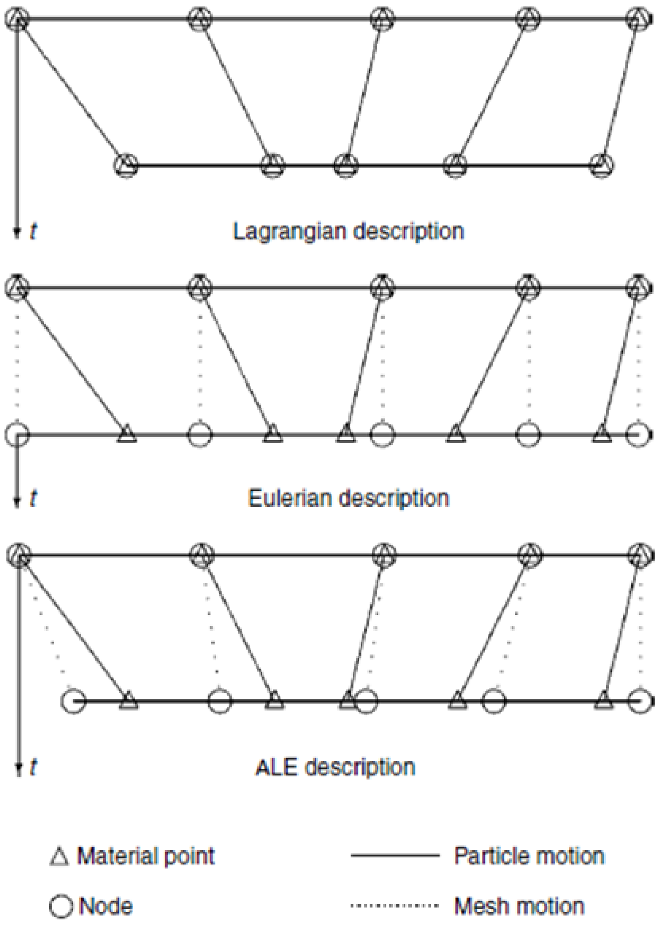

Figure 2.1 One dimensional example of Lagrangian, Eulerian and ALE mesh and particle motion

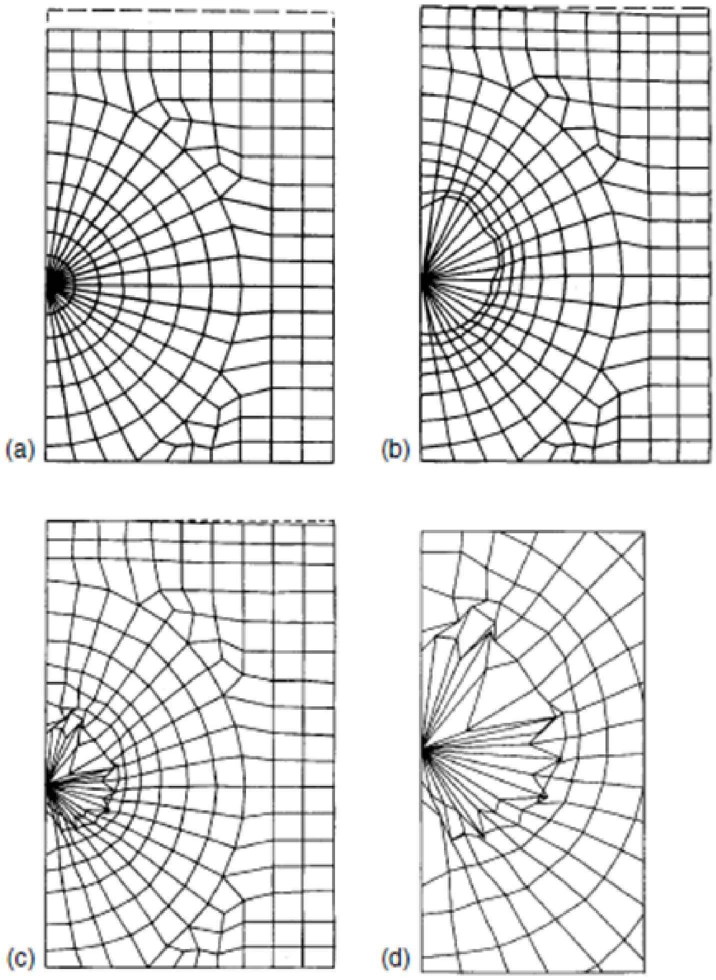

Figure 2.2 Lagrangian versus ALE description: (a) initial FE mesh: (b) ALE mesh at t = 1 ms; (c) Lagrangian mesh at t = 1 ms; (d) details of interface in Lagrangian description [12]

Because of the shortcomings of purely Lagrangian and purely Eulerian descriptions, a technique has been developed that succeeds, to a certain extent, in combining the best features of both the Lagrangian and the Eulerian approaches. Such a technique is known as the arbitrary Lagrangian–Eulerian (ALE) description. In the ALE description, the nodes of the computational mesh may be moved with the continuum in normal Lagrangian fashion, or be fixed in Eulerian manner, or, as suggested in Figure 2.1, be moved in some arbitrarily specified way to give a continuous rezoning capability. Because of this freedom in moving the computational mesh offered by the ALE description, greater distortions of the continuum can be handled than would be allowed by a purely Lagrangian method, with more resolution than that afforded by a purely Eulerian approach. The simple example in Figure 2.2 illustrates the ability of the ALE description to accommodate significant distortions of the computational mesh, while preserving the clear delineation of interfaces typical of a purely Lagrangian approach. A coarse finite element mesh is used to model the detonation of an explosive charge in an extremely strong cylindrical vessel partially filled with water. A comparison is made of the mesh configurations at time $t = 1.0$ ms obtained respectively, with the ALE description (with automatic continuous rezoning) and with a purely Lagrangian mesh description. As further evidenced by the details of the charge–water interface, the Lagrangian approach suffers from a severe degradation of the computational mesh, in contrast with the ability of the ALE approach to maintain quite a regular mesh configuration of the charge–water interface.

2.2 Descriptions of motion

Since the ALE description of motion is a generalization of the Lagrangian and Eulerian descriptions, we start with a brief reminder of these classical descriptions of motion. I closely follow the presentation by Donea and Huerta [52].

2.2.1. Lagrangian and Eulerian viewpoints

Two domains are commonly used in continuum mechanics: the material domain $R_X \subset R^{nsd}$, with ^{nsd} spatial dimensions, made up of material particles X, and the spatial domain R_x, consisting of spatial points x.

The Lagrangian viewpoint consists of following the material particles of the continuum in their motion. To this end, one introduces, as suggested in Figure 2.3, a computational grid, which follows the continuum in its motion, the grid nodes being permanently connected to the same material points. The material coordinates, X, allow us to identify the reference configuration, R_X. The motion of the material points relates the material coordinates, X, to the spatial ones, x. It is defined by an application φ such that

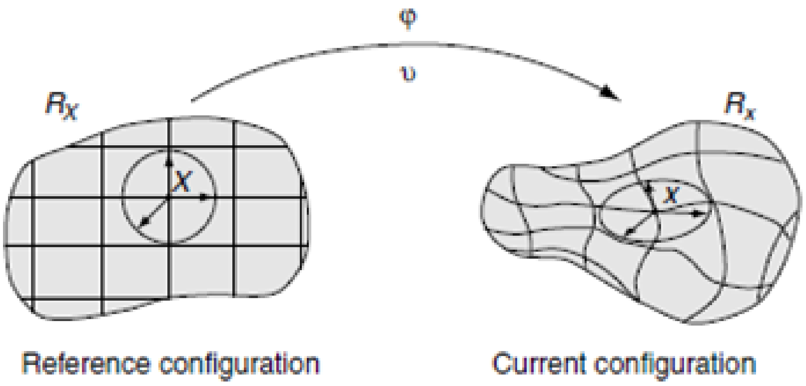

Figure 2.3 Lagrangian description of motion

$$\begin{aligned} \varphi : R_{\mathrm{X}} \times [t_0, t_{final}] &\mapsto R_x \times [t_0, t_{final}] \\ (\mathrm{X}, t) &\mapsto \varphi(\mathrm{X}, t) = (x, t) \end{aligned} \tag{2.1}$$

which allows us to link X and x in time by the law of motion, namely

$$x = x(X, t), \;\; t = t \tag{2.2}$$

which explicitly states the particular nature of φ: first, the spatial coordinates x depend both on the material particle X and time t, and, second, physical time is measured by the same variable t in both material and spatial domains. For every fixed instant t, the mapping φ defines a configuration in the spatial domain. It is convenient to employ a matrix representation for the gradient of φ,

$$\frac{\partial \varphi}{\partial (X, t)} = \begin{pmatrix} \dfrac{\partial x}{\partial X} & v \\ 0^T & 1 \end{pmatrix} \tag{2.3}$$

where 0^T is a null row-vector and the material velocity v is

$$v(X, t) = \left. \frac{\partial x}{\partial t} \right|_x \tag{2.4}$$

With $\Big|_x$ meaning “holding the material coordinate x fixed”. Obviously, the one-to-one mapping φ must verify det(∂x/∂X) > 0 (nonzero to impose a one-to-one correspondence and positive to avoid orientation change of the reference axes) at each point X and instant $t > t_0$. This allows us to keep track of the history of motion and, by the inverse transformation (X, t) = φ^{-1}(x, t), to identify, at any instant, the initial position of the material particle occupying position x at time t .

Since the material points coincide with the same grid points during the whole motion, there are no convective effects in Lagrangian calculations: the material derivative reduces to a simple time derivative. The fact that each finite element of a Lagrangian mesh always contains the same material particles represents a significant advantage from the computational viewpoint, especially in problems involving materials with history-dependent behavior. This aspect is discussed in detail by Bonet and Wood [53]. However, when large material deformations do occur, for instance vortices in fluids, Lagrangian algorithms undergo a loss in accuracy, and may even be unable to finish a calculation, due to excessive distortions of the computational mesh linked to the material.

The difficulties caused by an excessive distortion of the finite element grid are overcome in the Eulerian formulation. The basic idea in the Eulerian formulation, which is very popular in fluid mechanics, consists in examining, as time evolves, the physical quantities associated with the fluid particles passing through a fixed region of space. In an Eulerian description, the finite element mesh is thus fixed and the continuum moves and deforms with respect to the computational grid. The conservation equations are formulated in terms of the spatial coordinates x and the time t . Therefore, the Eulerian description of motion only involves variables and functions having an instantaneous significance in a fixed region of space. The material velocity v at a given mesh node corresponds to the velocity of the material point coincident at the considered time t with the considered node. The velocity v is consequently expressed with respect to the fixed-element mesh without any reference to the initial configuration of the continuum and the material coordinates X: v = v(x, t).

Since the Eulerian formulation dissociates the mesh nodes from the material particles, convective effects appear because of the relative motion between the deforming material and the computational grid. Eulerian algorithms present numerical difficulties due to the nonsymmetric character of convection operators, but permit an easy treatment of complex material motion. By contrast with the Lagrangian description, serious difficulties are now found in following deforming material interfaces and mobile boundaries.

2.2.2 ALE kinematical description

The above reminder of the classical Lagrangian and Eulerian descriptions has highlighted the advantages and drawbacks of each individual formulation. It has also shown the potential interest in a generalized description capable of combining at best the interesting aspects of the classical mesh descriptions while minimizing their drawbacks as far as possible. Such a generalized description is termed arbitrary Lagrangian–Eulerian (ALE) description. ALE methods were first proposed in the finite difference and finite volume context. Original developments were made, among others, by Noh [53], Franck and Lazarus [54], Trulio [55], and Hirt et al. [12]; this last contribution has been reprinted in 1997. The method was subsequently adopted in the finite element context and early applications are to be found in the work of Donea et al. [13], Belytschko and Kennedy [48], and Hughes et al. [56].

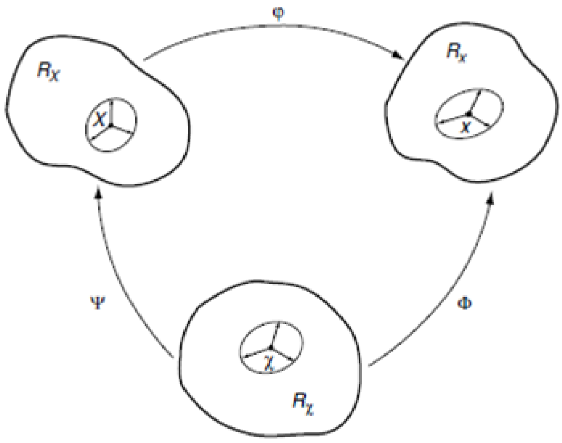

Figure 2.4 The motion of the ALE computational mesh is independent of the material motion. [12]

In the ALE description of motion, neither the material configuration R_X nor the spatial configuration Rx is taken as the reference. Thus, a third domain is needed: the referential configuration Rχ where reference coordinates χ are introduced to identify the grid points. Figure 2.4 shows these domains and the one-to-one transformations relating the configurations. The referential domain Rχ is mapped into the material and spatial domains by Ψ and Φ, respectively. The particle motion ϕ may then be expressed as $\varphi = \Phi \circ \Psi^{-1}$, clearly showing that, of course, the three mappings Φ, Ψ, and φ are not independent. The mapping of Φ from the referential domain to the spatial domain, which can be understood as the motion of the grid points in the spatial domain, is represented by

$$\begin{aligned} \Phi : R_\chi \times [t_0, t_{final}] &\mapsto R_x \times [t_0, t_{final}] \\ (\chi, t) &\mapsto \Phi(\chi, t) = (x, t) \end{aligned} \tag{2.5}$$

and its gradient is

$$\frac{\partial \Phi}{\partial(\chi,t)} = \begin{pmatrix} \dfrac{\partial x}{\partial \chi} & \hat{v} \\ 0^T & 1 \end{pmatrix} \square \tag{2.6}$$

where now, the mesh velocity

$$\hat{v}(\chi,t) = \left.\frac{\partial x}{\partial t}\right|_{\chi} \tag{2.7}$$

is involved. Note that both the material and the mesh move with respect to the laboratory (spatial). Thus, the corresponding material and mesh velocities have been defined by deriving the equations of material motion and mesh motion respectively with respect to time (see equations 2.4 and 2.7). Finally, regarding Ψ, it is convenient to represent directly its inverse Ψ^{-1},

$$\begin{aligned} \Psi^{-1} = R_X \times [t_0, t_{final}] &\mapsto R_{\chi} \times [t_0, t_{final}] \\ (X,t) &\mapsto \Psi^{-1}(X,t) = (\chi,t) \end{aligned} \tag{2.8}$$

and its gradient is

$$\frac{\partial \Psi^{-1}}{\partial(\chi,t)} = \begin{pmatrix} \dfrac{\partial \chi}{\partial X} & w \\ 0^T & 1 \end{pmatrix} \tag{2.9}$$

where the velocity w is defined as

$$w=\left.\frac{\partial\chi}{\partial t}\right|_{X} \tag{2.10}$$

and can be interpreted as the particle velocity in the referential domain, since it measures the time variation of the referential coordinate χ holding the material particle X fixed. The relation between velocities v, $\hat{v}$, and w can be obtained by differentiating $\varphi = \Phi \circ \Psi^{-1}$,

$$\begin{aligned}\frac{\partial\varphi}{\partial(X,t)}(X,t)&=\frac{\partial\Phi}{\partial(\chi,t)}(\Psi^{-1}(X,t))\frac{\partial\Psi^{-1}}{\partial(X,t)}(X,t)\\&=\frac{\partial\Phi}{\partial(\chi,t)}(\chi,t))\frac{\partial\Psi^{-1}}{\partial(X,t)}(X,t)\end{aligned} \tag{2.11}$$

or, in matrix format:

□

$$\begin{pmatrix}\dfrac{\partial x}{\partial X} & v\\ 0^{T} & 1\end{pmatrix}=\begin{pmatrix}\dfrac{\partial x}{\partial\chi} & \hat{v}\\ 0^{T} & 1\end{pmatrix}\begin{pmatrix}\dfrac{\partial\chi}{\partial X} & w\\ 0^{T} & 1\end{pmatrix} \tag{2.12}$$

which yields, after block multiplication,

$$v=\hat{v}+\frac{\partial x}{\partial\chi}\cdot w \tag{2.13}$$

This equation may be rewritten as

$$c := v - \hat{v} = \frac{\partial x}{\partial \chi} \cdot w \tag{2.14}$$

thus defining the convective velocity c, that is, the relative velocity between the material and the mesh. The convective velocity c (see equation 2. 14), should not be confused with w (see equation 2. 10). As stated before, w is the particle velocity as seen from the referential domain Rχ, whereas c is the particle velocity relative to the mesh as seen from the spatial domain Rx (both v and $\hat{v}$ are variations of coordinate x). In fact, equation (2. 14) implies that c = w if and only if ∂x/∂χ = I (where I is the identity tensor), that is, when the mesh motion is purely translational, without rotations or deformations of any kind.

After the fundamentals on ALE kinematics have been presented, it should be remarked that both Lagrangian or Eulerian formulations may be obtained as particular cases. With the choice Ψ = I , equation (2.3) reduces to X ≡ χ and a Lagrangian description results: the material and mesh velocities, equations (2.4) and (2.7), coincide, and the convective velocity c (see equation 2.14), is null (there are no convective terms in the conservation laws). If, on the other hand, $\Phi = \mathrm{I}$, equation (2.2) simplifies into x ≡ χ, thus implying a Eulerian description: a null mesh velocity is obtained from equation (2.7) and the convective velocity c is simply identical to the material velocity v. In the ALE formulation, the freedom of moving the mesh is very attractive. It helps to combine the respective advantages of the Lagrangian and Eulerian formulations. This could, however, be overshadowed by the burden of specifying grid velocities well suited to the particular problem under consideration. As a consequence, the practical implementation of the ALE description requires that an automatic mesh-displacement prescription algorithm be supplied.

2.3 The fundamental ALE equation

In order to express the conservation laws for mass, momentum, and energy in an ALE framework, a relation between material (or total) time derivative, which is inherent in conservation laws, and referential time derivative is needed.

2.3.1 Material, spatial, and referential time derivatives

In order to relate the time derivative in the material, spatial, and referential domains, let a scalar physical quantity be described by f (x, t), f^* (χ, t), and f** (X, t) in the spatial, referential, and material domains respectively. Stars are employed to emphasize that the functional forms are, in general, different. Since the particle motion ϕ is a mapping, the spatial description f (x, t), and the material description f**(X, t) of the physical quantity can be related as

$$f^{**}(X,t) = f(\varphi(X,t),t) \quad or \quad f^{**} = f \circ \varphi \tag{2.15}$$

The gradient of this expression can be easily expressed as ∂f

$$\frac{\partial f^{**}}{\partial(X,t)}(X,t) = \frac{\partial f}{\partial(x,t)}(x,t)\frac{\partial \varphi}{\partial(X,t)}(X,t) \tag{2.16}$$

which is amenable to the matrix form

$$\begin{pmatrix} \dfrac{\partial f^{**}}{\partial X} & \dfrac{\partial f^{**}}{\partial t} \end{pmatrix} = \begin{pmatrix} \dfrac{\partial f}{\partial x} & \dfrac{\partial f}{\partial t} \end{pmatrix} \begin{pmatrix} \dfrac{\partial x}{\partial X} & v \\ 0^T & 1 \end{pmatrix} \tag{2.17}$$

which renders, after block multiplication, the first expression, which is obvious, that is, $(\partial f^{**}/\partial X) = (\partial f/\partial x)(\partial x/\partial X)$; however, the second one is more interesting:

$$\frac{\partial f^{**}}{\partial t} = \frac{\partial f}{\partial t} + \frac{\partial f}{\partial x} \cdot v \tag{2.18}$$

Note that this is the well-known equation that relates the material and the spatial time derivatives. Dropping the stars to ease the notation, this relation is finally casted as

$$\left.\frac{\partial f}{\partial t}\right|_X = \left.\frac{\partial f}{\partial t}\right|_x + v \cdot \nabla f \quad or \quad \frac{df}{dt} = \frac{\partial f}{\partial t} + v \cdot \nabla f \tag{2.19}$$

which can be interpreted in the usual way: the variation of a physical quantity for a given particle X is the local variation plus a convective term taking into account the relative motion between the material and spatial (laboratory) systems. Moreover, in order not to overload the rest of the text with notation, except for the specific sections, the material time derivative is denoted as

$$\frac{d\,\cdot}{dt} := \left.\frac{\partial\,\cdot}{\partial t}\right|_X \tag{2.20}$$

and the spatial time derivative as

$$\frac{d\,\cdot}{dt} := \left.\frac{\partial\,\cdot}{\partial t}\right|_x \tag{2.21}$$

The relation between material and spatial time derivatives is now extended to include the referential time derivative. With the help of mapping □, the transformation from the referential description f* (χ, t) of the scalar physical quantity to the material description f** (X, t) can be written as

$$f^{**} = f^{*} \circ \Psi^{-1} \tag{2.22}$$

and its gradient can be easily computed as

$$\frac{\partial f^{**}}{\partial(X,t)}(X,t)=\frac{\partial f^{*}}{\partial(\chi,t)}(\chi,t)\frac{\partial \Psi^{-1}}{\partial(X,t)}(X,t) \tag{2.23}$$

or, in matrix form

$$\begin{pmatrix} \dfrac{\partial f^{**}}{\partial X} & \dfrac{\partial f^{**}}{\partial t} \end{pmatrix}=\begin{pmatrix} \dfrac{\partial f^{*}}{\partial \chi} & \dfrac{\partial f^{*}}{\partial t} \end{pmatrix}\begin{pmatrix} \dfrac{\partial \chi}{\partial X} & w \\ 0^{T} & 1 \end{pmatrix} \tag{2.24}$$

which renders, after block multiplication,

$$\frac{\partial f^{**}}{\partial t}=\frac{\partial f^{*}}{\partial t}+\frac{\partial f^{*}}{\partial \chi}\cdot w \tag{2.25}$$

Note that this equation relates the material and the referential time derivatives. However, it also requires the evaluation of the gradient of the considered quantity in the referential domain. This can be done, but in computational mechanics it is usually easier to work in the spatial (or material) domain. Moreover, in fluids, constitutive relations are naturally expressed in the spatial configuration and the Cauchy stress tensor, which will be introduced next, is the natural measure for stresses. Thus, using the definition of w given in equation (2.14), the previous equation may be rearranged into

$$\frac{\partial f^{**}}{\partial t} = \frac{\partial f^{*}}{\partial t} + \frac{\partial f^{*}}{\partial x} \cdot c \tag{2.26}$$

The fundamental ALE relation between material time derivatives, referential time derivatives, and spatial gradient is finally cast as (stars dropped)

$$\left.\frac{\partial f}{\partial t}\right|_{X} = \left.\frac{\partial f}{\partial t}\right|_{\chi} + \frac{\partial f}{\partial x} \cdot c = \left.\frac{\partial f}{\partial t}\right|_{\chi} + c \cdot \nabla f \tag{2.27}$$

and shows that the time derivative of the physical quantity f for a given particle X, that is, its material derivative, is its local derivative (with the reference coordinate χ held fixed) plus a convective term taking into account the relative velocity c between the material and the reference system. This equation is equivalent to equation (2.19) but in the ALE formulation, that is, when (χ, t) is the reference.

2.3.2 Time derivative of integrals over moving volumes

To establish the integral form of the basic conservation laws for mass, momentum, and energy, we also need to consider the rate of change of integrals of scalar and vector functions over a moving volume occupied by fluid. Consider thus a material volume V_t bounded by a smooth closed surface S_t whose points at time t move with the material velocity v = v(x, t) where x $\in$ S_t. A material volume is a volume that permanently contains the same particles of the continuum under consideration. The material time derivative of the integral of a scalar function f (x, t) (note that f is defined in the spatial domain) over the time-varying material volume V_t is given by the following well-known expression, often referred to as Reynolds transport theorem

$$\begin{aligned}\frac{d}{dt}\int_{V_t} f(x,t)dV = \int_{V_c \equiv V_t} \frac{\partial f(x,t)}{\partial t} dV \\ + \int_{S_c \equiv S_t} f(x,t) v \cdot n\, dS\end{aligned} \tag{2.28}$$

which holds for smooth functions f (x, t). The volume integral in the right-hand side is defined over a control volume V_c (fixed in space), which coincides with the moving material volume V_t at the considered instant, t, in time. Similarly, the fixed control surface S_c coincides at time t with the closed surface S_t bounding the material volume V_t . In the surface integral, n denotes the unit vector outward normal to the surface S_t at time t, and v is the material velocity of points of the boundary S_t. The first term in the right-hand side of expression (2.28) is the local time derivative of the volume integral. The boundary integral represents the flux of the scalar quantity f across the fixed boundary of the control volume $V_c \equiv V_t$.

Noting that

$$\int_{S_c} f(x,t) v \cdot n\, dS = \int_{V_c} \nabla \cdot (f\, v)\, dV \tag{2.29}$$

one obtains the alternative form of Reynolds transport theorem:

$$\frac{d}{dt}\int_{V_t} f(x,t)dV = \int_{V_c \equiv V_t} \left(\frac{\partial f(x,t)}{\partial t} + \nabla \cdot (f\, v) \right) dV \tag{2.30}$$

Similar forms hold for the material derivative of the volume integral of a vector quantity. Analogous formulae can be developed in the ALE context, that is, with a referential time derivative. In this case, however, the characterizing velocity is no longer the material velocity v, but the grid velocity $\hat{v}$.

2.4 The ALE forms of governing equations

The ALE description is a hybrid approach combining the advantages of the Lagrangian and Eulerian formulations. In Lagrangian approach, each node of computational mesh is attached to continuum particles and moves with them, while, in Eulerian approach, mesh nodes remain fixed as continuum particles pass through them. Considering the fact that some grain particles are eroded due to the burnback of propellant surface, neither Lagrangian nor Eulerian approach can properly describe the process of solid propellant burning. In the ALE approach, numerical simulation is firstly conducted in Eulerian manner while deformation of computational mesh is described by Lagrangian pattern. It thus provides a numerical setting suitable for simulating the burning of solid propellant [11].

Since the ALE transformation procedure is well described in some of the previous researches [12], we are going to present the final modified ALE form of the Navier-Stokes equations for fluid simulation and the virtual work equation for structure simulation. Firstly, the modified ALE form of the Navier-Stokes equations can be written as follows.

$$\left.\frac{\partial}{\partial t}\right|_{\chi} \int_V \rho dV + \int_S \rho c \cdot n dS = 0 \quad ,$$

$$\left.\frac{\partial}{\partial t}\right|_{\chi} \int_V \rho v dV + \int_S \rho v c \cdot n dS = \int_V \left(\nabla \cdot \sigma + \rho b\right) dV \quad ,$$

$$\left.\frac{\partial}{\partial t}\right|_{\chi} \int_V \rho E dV + \int_S \rho E c \cdot n dS = \int_V \left(v \cdot \rho b + \nabla \cdot (\sigma \cdot v)\right) dV \quad , \qquad (2.31)$$

where ρ is the mass density, v is the material velocity vector, σ denotes the Cauchy stress tensor, b is the specific body force vector, E is the specific total energy, and c is the relative velocity between material and mesh velocity. Arbitrary motion of computational mesh is reflected into the convective terms of the left-hand-side of the governing equations, which makes the numerical implementation of the ALE description quite efficient.

Secondly, the virtual work equation for solid analysis is given as follows.

$$\int_V \rho \frac{\partial^2 \hat{u}_i}{\partial t^2} \delta u_i dV + \int_V \sigma_{ij} \frac{\partial \delta u_i}{\partial X_j} dV = \int_{\partial V_T} f_i \delta u_i da \tag{2.32}$$

Like the preceding Navier-Stokes equations, only the acceleration term of the virtual work equation (the first term of Eqn. (2.32)) is converted into the ALE form (or the first eight terms of the left-hand side of Eqn. (2.33)) as follows [13].

$$\begin{aligned}
&\int_V \rho \frac{\partial^2 \hat{u}_i}{\partial t^2} \delta u_i dV - 2\int_V \rho \frac{\partial^2 \hat{u}_i}{\partial t \partial \xi_\alpha} \frac{\partial \xi_\alpha}{\partial X_j} \frac{\partial \widehat{X}_j}{\partial t} \delta u_i dV \\
&+ \int_{\partial V} \rho \frac{\partial u_i}{\partial X_j} \frac{\partial \widehat{X}_k}{\partial t} \frac{\partial \widehat{X}_j}{\partial t} n_k \delta u_i da - \int_V \rho \frac{\partial u_i}{\partial X_j} \frac{\partial^2 \widehat{X}_k}{\partial t \partial \xi_\alpha} \frac{\partial \xi_\alpha}{\partial X_k} \frac{\partial \widehat{X}_j}{\partial t} \delta u_i dV \\
&- \int_V \rho \frac{\partial u_i}{\partial X_j} \frac{\partial \widehat{X}_k}{\partial t} \frac{\partial^2 \widehat{X}_j}{\partial t \partial \xi_\alpha} \frac{\partial \xi_\alpha}{\partial X_k} \delta u_i dV - \int_V \rho \frac{\partial u_i}{\partial X_j} \frac{\partial \widehat{X}_k}{\partial t} \frac{\partial \widehat{X}_j}{\partial t} \frac{\partial \delta u_i}{\partial X_k} dV \\
&+ 2\int_V \rho \frac{\partial u_i}{\partial X_k} \frac{\partial^2 \widehat{X}_k}{\partial t \partial \xi_\alpha} \frac{\partial \xi_\alpha}{\partial X_j} \frac{\partial \widehat{X}_j}{\partial t} \delta u_i dV - \int_V \rho \frac{\partial u_i}{\partial X_j} \frac{\partial^2 \widehat{X}_j}{\partial t^2} \delta u_i dV \\
&+ \int_V C_{ijkl} \frac{\partial u_k}{\partial X_j} \frac{\partial \delta u_i}{\partial X_j} \delta u_i dV = \int_{\partial V_T} f_i \delta u_i da
\end{aligned} \tag{2.33}$$

Here, ρ is the solid density, $\frac{\partial u}{\partial X}$ is the displacement vector, $\frac{\partial \widehat{X}}{\partial t}$ is the mesh velocity, ξ is the coordinate of reference domain, and C_{ijkl} is the elastic modulus of solid. The first term of Eqn. (2.33) is the ALE mass matrix, the second term is the damping force vector and the others of the left-hand side are related to the internal force. The right-hand-side term indicates the specific external force.

Chapter III

NUMERICAL METHODS II

3.1 Fluid solver

We consider two-dimensional axisymmetric compressible flows for the interior combustion chamber. Since the mass flux from the exposed grain boundary will sweep away boundary layer, we may assume viscous effect after ignition is relatively small near grain surface, and thus the inviscid flow solver can provide basic flow features. At the early stage of ignition process, however, flow physics including viscous and turbulence effects does influence the outbreak of the burning at grain surface and ignition delay time. Thus, both inviscid and viscous simulations have been performed. The modified ALE form of the two-dimensional Navier-Stokes equations is as follows.

$$u_t + div(F) = div(K)\,, \tag{3.1}$$

where u is the state vector, and F and K are the inviscid and viscous flux vectors, respectively.

$$K = \begin{pmatrix} 0 \\ \tau_{xx} \\ \tau_{yy} \\ u\tau_{xx} + v\tau_{yy} - q_x \end{pmatrix} \hat{i} + \begin{pmatrix} 0 \\ \tau_{xy} \\ \tau_{yy} \\ u\tau_{yx} + v\tau_{yy} - q_y \end{pmatrix} \hat{j}.\cdot$$

$$K = \begin{pmatrix} 0 \\ \tau_{xx} \\ \tau_{yy} \\ u\tau_{xx} + v\tau_{yy} - q_x \end{pmatrix} \hat{i} + \begin{pmatrix} 0 \\ \tau_{xy} \\ \tau_{yy} \\ u\tau_{yx} + v\tau_{yy} - q_y \end{pmatrix} \hat{j}. \tag{3.2}$$

Here, v_{xc}, v_{yc} is the relative velocity between the material velocity and the mesh velocity, and K = 0 if the flow is inviscid. The 3rd-order TVD Runge-Kutta explicit scheme and Point Gauss-Seidel implicit scheme are used for time marching. As a spatial flux scheme, AUSMPW+ by Kim et al. is used to accurately capture physical discontinuities without numerical oscillation [14-16].

3.1.1 Spatial Discretization

As shown in Eq. (3.2), the governing equations can be decomposed to the inviscid flux term and the viscous flux term. The inviscid flux term F can be separated in the x-, y-, and z- directions and are discretized with a finite volume method based approach. For convenience Inviscid flux term F divided into three direction terms of E, F, and, G. The local flux balance of each cell is

$$\left(\frac{\partial E}{\partial x}+\frac{\partial F}{\partial y}+\frac{\partial G}{\partial z}\right)_{i,j,k}=\tilde{E}_{i+\frac{1}{2},j,k}-\tilde{E}_{i-\frac{1}{2},j,k}+\tilde{F}_{i,j+\frac{1}{2},k}-\tilde{F}_{i,j-\frac{1}{2},k}+\tilde{G}_{i,j,k+\frac{1}{2}}-\tilde{G}_{i,j,k-\frac{1}{2}} \tag{3.3}$$

Because Eq. (3.3) is in a central-differenced form and in non-dissipative by itself, the inviscid fluxes should be modified to cell surface fluxes by explicitly adding the numerical dissipation term as follows:

$$\tilde{E}_{i+\frac{1}{2},j,k}=\frac{1}{2}\left[\hat{E}(Q_i)+\hat{E}(Q_{i+1})-\left|\hat{A}(Q_i,Q_{i+1})\right|(Q_{i+1}-Q_i)\right] \tag{3.4}$$

where the matrix $\hat{A}(Q_i,Q_{i+1})$ is the flux Jacobian matrix, and the inviscid flux is upwind-differenced. In this work, two types of flux schemes of Roe's FDS and RoeM are usually used for the spatial discretization

3.1.1.1 Roe's Flux Difference Splitting

Roe's Flux Difference Splitting (FDS) scheme is based on the approximate solution of Riemann problem. Instead of solving the exact Riemann problem iteratively, Roe linearized the Jacobian matrix to satisfy the following properties:

(1) $\hat{A}$ is a linear mapping to $\hat{E}$ in a vector space Q

(2) $\hat{A}$ satisfies consistency condition, so $\hat{A}(Q_i, Q_{i+1}) = \hat{A}(Q_{i+1/2})$

(3) $\hat{A}$ has linearly independent eigenvectors and real eigenvalues.

(4) $\hat{A}(Q_i, Q_{i+1})(Q_{i+1} - Q_i) = \hat{E}_{i+1} - \hat{E}_i$ for any Q_i, Q_{i+1}

From the condition (4), the linearized flux Jacobian $\hat{A}$ can be expressed in terms of Roe-averaged properties $\overline{\rho}$ and $\overline{Q}$ as:

$$\overline{\rho} = \sqrt{\rho_i \rho_{i+1}} \tag{3.5}$$

$$\overline{Q} = \frac{Q_i \sqrt{\rho_i} + Q_{i+1} \sqrt{\rho_{i+1}}}{\sqrt{\rho_i} + \sqrt{\rho_{i+1}}} \tag{3.6}$$

From the eigenmatrix $\hat{X}$ of $\hat{A}$, the diagonal matrix Λ composed of eigenvalues, and the condition (2), the third term on the right-hand side of Eq. (3.4) is replaced into vector calculation as:

$$\left|\hat{A}(Q)\right|(Q_{i+1} - Q_i) = \left(\hat{X}|\Lambda|\hat{X}^{-1}\right)\hat{X}\hat{\alpha} = \hat{X}|\Lambda|\hat{\alpha} = \hat{\alpha}_k |\lambda_k| \hat{e}_k \tag{3.7}$$

By using these Roe-averaged properties the flux can be calculated as follows:

$$\tilde{E}_{i+\frac{1}{2}} = \frac{1}{2}\left[\hat{E}\left(Q_i\right)+\hat{E}\left(Q_{i+1}\right)-\hat{\alpha}_k\left|\lambda_k\right|\hat{e}_k\right] \tag{3.8}$$

$$\hat{\alpha}_k\left|\lambda_k\right|\hat{e}_k = \begin{bmatrix} \alpha_4 \\ \bar{u}\alpha_4 + x_x\alpha_5 + \alpha_6 \\ \bar{v}\alpha_4 + x_y\alpha_5 + \alpha_7 \\ \bar{w}\alpha_4 + x_z\alpha_5 + \alpha_8 \\ \bar{H}\alpha_4 + \left(\bar{U} - x_t\right)\alpha_5 + \bar{u}\alpha_6 + \bar{v}\alpha_7 + \bar{w}\alpha_8 - \dfrac{\bar{a}^2}{\gamma - 1}\alpha_1 \\ \alpha_9 \\ \alpha_{10} \end{bmatrix}. \tag{3.9}$$

The coefficients of α are

$$\begin{aligned} \alpha_1 &= \left|\lambda_1\right|\left(\Delta\rho - \frac{\Delta p}{\bar{a}^2}\right), & \alpha_2 &= \left|\lambda_4\right|\left(\frac{\Delta p + \bar{\rho}\bar{a}\Delta U}{2\bar{a}^2}\right) \\ \alpha_3 &= \left|\lambda_5\right|\left(\frac{\Delta p - \bar{\rho}\bar{a}\Delta U}{2\bar{a}^2}\right), & \alpha_4 &= \alpha_1 + \alpha_2 + \alpha_3 \\ \alpha_5 &= \bar{a}\left(\alpha_2 - \alpha_3\right), & \alpha_6 &= \left|\lambda_1\right|\left(\bar{\rho}\Delta u - x_x\bar{\rho}\bar{U}\right) \\ \alpha_7 &= \left|\lambda_1\right|\left(\bar{\rho}\Delta v - x_y\bar{\rho}\bar{U}\right), & \alpha_8 &= \left|\lambda_1\right|\left(\bar{\rho}\Delta w - x_z\bar{\rho}\bar{U}\right) \\ \alpha_9 &= \left|\lambda_1\right|\bar{\rho}\Delta k, & \alpha_{10} &= \left|\lambda_1\right|\bar{\rho}\Delta w \end{aligned} \tag{3.10}$$

where,

$$\lambda_1 = \lambda_2 = \lambda_3 = \frac{|\nabla x|}{J}\bar{U}, \qquad \lambda_{4,5} = \frac{|\nabla x|}{J}\left(\bar{U} \pm \bar{a}\right)$$
$$\bar{U} = x_t + x_x\bar{u} + x_y\bar{v} + x_z\bar{w}, \quad x_{t,x,y,z} = \frac{x_{t,x,y,z}}{|\nabla x|} = \frac{x_{t,x,y,z}}{\sqrt{x_x + x_y + x_z}}. \tag{3.11}$$
$$H = {\left(e_t + p\right)}\big/{\rho}$$

The flux vectors $\tilde{F}_{j+1/2}$ and $\tilde{G}_{j+1/2}$ respectively on the *y*- and *z*-directions can be determined with similar flux calculation.

3.1.1.2 RoeM Scheme

Although Roe scheme shows remarkable accuracy, it is hard to distinguish a shock and an expansion discontinuity because entropy condition is violated. The carbuncle phenomena also suffer the robustness of the original Roe scheme. In order to overcome these problems, Kim et al [47]. proposed an improved Roe scheme that is free from the shock instability and preserves the accuracy and efficiency of the original Roe scheme.

The flux can be calculated by:

$$\begin{aligned}\tilde{E}_{i+1/2} = &\frac{b_1 \times \hat{E}\left(Q_i\right) + b_2 \times \hat{E}\left(Q_{i+1}\right)}{b_1 - b_2} + \frac{b_1 \times b_2}{b_1 - b_2}\Delta Q^* \\ &- g\frac{b_1 \times b_2}{b_1 - b_2} \times \frac{1}{1 + |\bar{M}|}B\Delta Q\end{aligned} \tag{3.12}$$

$$\Delta Q^{*}=\Delta\begin{pmatrix}\rho\\ \rho u\\ \rho v\\ \rho w\\ \rho H\end{pmatrix},\quad B\Delta Q=\left(\Delta\rho-f\frac{\Delta p}{\hat{c}^{2}}\right)\begin{pmatrix}1\\ \bar{u}\\ \bar{v}\\ \bar{w}\\ \bar{H}\end{pmatrix}+\bar{\rho}\begin{pmatrix}0\\ \Delta u-\Delta U\\ \Delta v-\Delta U\\ \Delta w-\Delta U\\ \Delta H\end{pmatrix} \tag{3.13}$$

Where

$$\bar{M}=\bar{U}/\bar{a},\quad b_{1}=\max\left(0,\bar{U}+\bar{a},U_{i+1}+\bar{a}\right),\quad b_{2}=\max\left(0,\bar{U}-\bar{a},U_{i-1}+\bar{a}\right)$$

And the functions f and g can be expressed by:

$$f=\begin{cases}1 & ,\bar{u}^{2}+\bar{v}^{2}+\bar{w}^{2}=0\\ \left|\bar{M}\right|^{h} & ,elsewhere\end{cases},$$
$$h=1-\min\begin{pmatrix}P_{i+1/2,j,k},P_{i,j+1/2,k},P_{i,j-1/2,k},P_{i,j,k+1/2},P_{i,j,k-1/2},\\ P_{i+1,j+1/2,k},P_{i+1,j-1/2,k},P_{i+1,j,k+1/2},P_{i+1,j,k-1/2}\end{pmatrix} \tag{3.14}$$

$$g=\begin{cases}\left|\bar{M}\right|^{1-\min\left(\frac{p_{i,j}}{p_{i+1,j}},\frac{p_{i+1,j}}{p_{i,j}}\right)} & ,\bar{M}=0\\ 1 & ,\bar{M}\neq 0\end{cases} \tag{3.15}$$

The differentiation of the flux function becomes more complicated than the original Roe scheme because of the function *f*, which considers 10 cells around the interface in the case of structured grid.

3.1.1.3 AUSMPW+

The AUSMPW+ flux scheme was designed to remove the non-monotonic pressure oscillations of the AUSM-type schemes near a wall or behind shock waves by introducing pressure-based weighting functions at a cell interface. Weight function f is introduced to treat the oscillations near a wall, and to remove the oscillation across a strong shock. The flux vector at a cell interface can be represented as:

$$\hat{F}_{1/2} = \bar{M}_L^{+} c_{1/2} \hat{\Phi}_L + \bar{M}_R^{-} c_{1/2} \hat{\Phi}_R + (P_L^{+} \hat{p}_L + P_R^{-} \hat{p}_R) \tag{3.16}$$

Where

$$\hat{\Phi} = (\rho \;\; \rho u \;\; \rho v \;\; \rho w \;\; \rho H)^T, \quad \hat{p} = (0 \;\; \bar{n}_x p \;\; \bar{n}_y p \;\; \bar{n}_z p \;\; 0)^T .$$

To obtain Mach numbers on the left and right side of the cell-interface, Mach number at the cell interface is first defined by

$$M_{1/2} = M_L^{+} + M_R^{-} \tag{3.17}$$

and Mach numbers on the left and right side are expressed respectively:

if $m_{1/2} \geq 0$,

$$\begin{aligned} \bar{M}_L^{+} &= M_L^{+} + M_R^{-} \cdot [(1-w)\cdot(1+f_R) - f_L] \\ \bar{M}_R^{-} &= M_R^{-} \cdot w \cdot (1+f_R) \end{aligned} \tag{3.18}$$

If $m_{1/2} < 0$,

$$\begin{aligned} \bar{M}_L^{+} &= M_L^{+} \cdot w \cdot (1+f_L) \\ \bar{M}_R^{-} &= M_R^{-} + M_L^{+} \cdot [(1-w)\cdot(1+f_L) - f_R] \end{aligned} \tag{3.19}$$

pressure based weight function $f_{L,R}$ and w are defined as

$$f_{L,R} = \begin{cases} \left(\dfrac{p_{L,R}}{p_s} - 1\right) \times \min\left(1, \dfrac{\min(p_{1,L}, p_{1,R}, p_{2,L}, p_{2,R})}{\min(p_L, p_R)}\right)^2 & \mathit{if}\ p_s \neq 0\ , \\ 0 & \mathit{if}\ p_s = 0 \end{cases} \tag{3.20}$$

Where $p_s = P_L^{+} p_L + P_R^{-} p_R$ and $p_{1,*}$, $p_{2,*}$ are the pressure values at each edge of a cell interface.

Equations from (3.18) to (3.19) use the split Mach number and pressure across a cell interface as the input values. These values are introduces as

$$M^{\pm} = \begin{cases} \pm\dfrac{1}{4}(M \pm 1)^2, & |\mathrm{M}| \leq 1 \\ \dfrac{1}{2}(M \pm |\mathrm{M}|), & |\mathrm{M}| > 1 \end{cases} \tag{3.21}$$

$$p^{\pm} = \begin{cases} \frac{1}{4}(M \pm 1)^2 \cdot (2 \mp M), & |\mathrm{M}| \le 1 \\ \frac{1}{2}(1 \pm \mathrm{sign(M)}), & |\mathrm{M}| > 1 \end{cases} \tag{3.22}$$

The Mach number on each side is defined as follows:

$$M_{L,R} = \frac{U_{L,R}}{c_{1/2}} \tag{3.23}$$

Here, $c_{1/2}$ is the speed of sound at a cell interface and computed as

$$c_{1/2} = \min\left[\frac{a^{*2}}{\max(|U_L|, a^*)} \, , \, \frac{a^{*2}}{\max(|U_R|, a^*)} \right] \tag{3.24}$$

where the critical speed of sound a^* is defined to satisfy the isoenergetic condition,

$$a^* = \sqrt{\frac{2(\gamma - 1)}{(\gamma + 1)} H} \, , \tag{3.25}$$

with H as the total enthalpy and U as the velocity component normal to a cell interface

3.1.1.4 Higher Order Spatial Accuracy

Monotone Upstream-centered Schemes for Conservation Laws (MUSCL) can provide highly accurate numerical solution for a given system, even in the cases where the solutions exhibits shocks, discontinuities occurs [41]. The MUSCL scheme is adopted as:

$$\begin{aligned} q^{Left}_{i+1/2} &= q_i + \frac{1}{4}\left[\left(1-\kappa\right)\phi^{+}_{i-1/2}\left(q_i - q_{i-1}\right) + \left(1+\kappa\right)\phi^{-}_{i+1/2}\left(q_{i+1} - q_i\right)\right] \\ q^{Right}_{i+1/2} &= q_{i+1} + \frac{1}{4}\left[\left(1+\kappa\right)\phi^{-}_{i+1/2}\left(q_{i+1} - q_i\right) + \left(1-\kappa\right)\phi^{+}_{i+3/2}\left(q_{i+2} - q_{i+1}\right)\right] \end{aligned} \tag{3.26}$$

where q denotes the primitive variables. When a constant κ=1/3, the order of spatial accuracy is third, and the second order accuracy is achieved with κ=-1, 0, 1. Especially at κ=1, it becomes a central difference scheme of the second order. Values of the primitive variables at the cell interface are modified by extrapolation, which cause an oscillation near physical discontinuities. To suppress this overshoot phenomenon of the solution, several limiters can be applied by using a function ϕ.

3.1.1.5 Sparlart-Allmaras turbulence model

The Sparlart-Allmaras turbulence model solves a single transport equation that determines the turbulent viscosity. This situation is in contrast to many of the early one-equation models that solve an equation for the transport of turbulent kinetic energy and required an algebraic prescription of a length scale.

The original model was developed primarily for the aerospace engineering , and has the advantage of being readily implemented in an unstructured CFD solver, unlike the more traditional aerospace models such as Baldwin-Lomax and Johnston-King. This advantage has resulted in its popularity increasing as the use of unstructured CFD methods has grown more widespread in the aerospace fields.

The author of the original Sparlart-Allmaras turbulence model presented results for attached boundary layer and flows with mild separation (such as flow past a wing). It is reasonable to expect that these cares are the types of flows for which the model yields the best results. Wilcox presents free-shear spreading rates for the model. While acceptable results are obtained for wake, mixing layer and radial jet flows, the predicted spreading rates for plane and round jets are inaccurate. [44, 57]

In this research, we should consider the computational cost of each solver, because FSbI simulations have many components to be computed in their own process. Therefore, we choose Sparlart-Allmaras model among 1-equation models because of its simplicity and relatively higher accuracy. The governing equations are follows.

$$\begin{aligned}\frac{D(\tilde{v})}{Dt} &= c_{b1}[1 - f_{t2}]\tilde{S}\tilde{v} + \frac{1}{\sigma}[\nabla \cdot ((v + \tilde{v}) + c_{b2}(\nabla \tilde{v}^{2})))] \\ &\quad - [c_{w1} f_{w} - \frac{c_{b1}}{\kappa^{2}} f_{t^{2}}]\left[\frac{\tilde{v}}{d}\right]^{2} + f_{t1}(\Delta q)^{2}\end{aligned} \tag{3.27}$$

The first term of right of Eqn. (3.27) means the advection, the second term is the production , the third is diffusion, and the last is trip (but in this research, the last trip term is ignored). The right-hand-side term indicates the specific external force.

The $\tilde{\nu}$ is an working variable and, finally, the turbulent viscous coefficient could be obtained using following relations.

$$\mu_t = \rho\tilde{\nu}\frac{\chi^3}{\chi^3 + c_{c1}^3}, \quad \chi = \frac{\tilde{\nu}}{\nu} \tag{3.28}$$

3.1.2 Time Integration Method

In this chapter, by replacing *t* with *τ*, the implicit methods to solve the pseudo-time equation, Eq. (3.1), is represented with the vector of the residual *R(Q)* to easily consider the time integrating formulation as:

$$\frac{1}{J}\frac{\partial Q}{\partial \tau} = -R(Q) \tag{3.29}$$

A first-order Euler implicit formula is used for pseudo-time derivative to form the matrix equation. The next consideration is the formation of the Jacobian matrix of the residual vector of the flux terms required for the implicit side of the resulting equation. However, the exact Jacobian of the flux vectors is very costly to form.

Instead, an approximate Jacobian of the residual vector can be used with different levels of approximation. Then, the matrix equation is solved using Point Gauss-Seidel (PGS) relaxation / TVD Runge-Kutta scheme.

3.1.3 Pseudo-Time Discretization

From Eq. (3.29) in the previous, the system of governing equations can be rewritten as:

$$\frac{1}{J}\frac{\partial Q^{n+1}}{\partial \tau}+\left[\frac{\partial}{\partial \xi}\left(\hat{E}-\hat{E}_v\right)+\frac{\partial}{\partial \eta}\left(\hat{F}-\hat{F}_v\right)+\frac{\partial}{\partial \zeta}\left(\hat{G}-\hat{G}_v\right)\right]+\hat{S}=0 \tag{3.30}$$

Consider a Taylor series expansion about time level *n* as follows:

$$E^{n+1}=E^n+\left[\frac{\partial E}{\partial Q}\right]\Delta Q+O(\Delta t^2)\cong E^n+A\Delta Q \tag{3.31}$$

In a similar fashion the other flux vectors can be linearized as:

$$\begin{aligned} F^{n+1} &\cong F^n+B\Delta Q \\ G^{n+1} &\cong G^n+C\Delta Q \end{aligned} \tag{3.32}$$

The viscous flux Jacobian in the implicit part is neglected since it does not influence the solution’s accuracy. Thus, the viscous flux vectors are approximated as follows:

$$\begin{aligned} E_v^{n+1} &\cong E^n \\ F_v^{n+1} &\cong F^n \\ G_v^{n+1} &\cong G^n \end{aligned} \tag{3.33}$$

Substituting the above linearizations to obtain

$$\begin{aligned} &\frac{1}{J}\frac{\partial Q^{n+1}}{\partial \tau}+\left[\frac{\partial}{\partial \xi}\left(\hat{E}+A\Delta Q\right)+\frac{\partial}{\partial \eta}\left(\hat{F}+B\Delta Q\right)+\frac{\partial}{\partial \zeta}\left(\hat{G}+C\Delta Q\right)\right] \\ &-\left(\frac{\partial E_v}{\partial \xi}+\frac{\partial F_v}{\partial \eta}+\frac{\partial G_v}{\partial \zeta}\right)+\hat{S}=0 \end{aligned} \tag{3.34}$$

Rewriting the Eq. (3.33)

$$\begin{aligned} &\frac{1}{J}\frac{\partial Q^{n+1}}{\partial \tau}+\frac{\partial}{\partial \xi}\left(A\Delta Q\right)+\frac{\partial}{\partial \eta}\left(B\Delta Q\right)+\frac{\partial}{\partial \zeta}\left(C\Delta Q\right) \\ &=-\left(\frac{\partial}{\partial \xi}\left(\hat{E}+E_v\right)+\frac{\partial}{\partial \eta}\left(\hat{F}+F_v\right)+\frac{\partial}{\partial \zeta}\left(\hat{G}+G_v\right)\right)^n-\hat{S} \end{aligned} \tag{3.35}$$

and is factored as

$$\left(\frac{1}{J\Delta\tau}+\frac{\partial A}{\partial\xi}+\frac{\partial B}{\partial\eta}+\frac{\partial C}{\partial\zeta}\right)\Delta Q$$
$$=-\left(\frac{\partial}{\partial\xi}\left(\hat{E}+E_v\right)+\frac{\partial}{\partial\eta}\left(\hat{F}+F_v\right)+\frac{\partial}{\partial\zeta}\left(\hat{G}+\hat{G}_v\right)\right)^n-\hat{S}=-R^n \tag{3.36}$$

where *I* is the identity matrix and *R* stand for the residual vector including viscous and turbulence terms. The flux Jacobian matrices are split according to the signs of the eigenvalues of the flux Jacobian matrices as:

$$\left(\frac{1}{J\Delta\tau}+\delta_\xi^+A^+ +\delta_\xi^-A^- +\delta_\eta^+B^+ +\delta_\eta^-B^- +\delta_\zeta^+C^+ +\delta_\zeta^-C^-\right)\Delta Q=-R^n \tag{3.37}$$

Where, δ denotes a finite difference operator in each direction.

3.1.4 Dual Time Stepping

For time-accurate unsteady problems, pseudo-time sub-iteration strategy is adopted to solve the unsteady systems given by:

$$\frac{1}{J}\frac{\partial\hat{Q}}{\partial t}=-\hat{R}. \tag{3.38}$$

The time derivative term is differenced using a backward second-order three-point implicit formula and moved to the right-hand side of the equation:

$$0 = -\frac{1.5Q^{n+1} - 2Q^{n} + 0.5Q^{n-1}}{J\Delta t} - \hat{R}^{n+1} \tag{3.39}$$

A pseudo-time derivative of Q is added on the left-hand side of Eq. (3.38):

$$\frac{1}{J}\frac{\partial Q^{n+1}}{\partial \tau} = -\hat{R}^{n+1} - \frac{1.5Q^{n+1} - 2Q^{n} + 0.5Q^{n-1}}{J\Delta t} = -\hat{R}^{n+1} - \hat{S}^{n+1} \tag{3.40}$$

Since the first-order discretization has better convergence properties than higher-order in general, the pseudo-time derivative term is discretized using the first-order Euler implicit formula :

$$\frac{1}{J}\frac{Q^{n+1,m+1} - Q^{n+1,m}}{\Delta \tau} = -\hat{R}^{n+1,m+1} - \hat{S}^{n+1,m+1} \tag{3.41}$$

where a superscript m denotes the pseudo-time iteration level. The time accuracy of the solution is necessary in terms of the physical time, but not in terms of the pseudo-time. Therefore, the dual time stepping method adopted here has second-order time accuracy. Now, Eq. (3.41) can be rewritten as:

$$\frac{1}{J\Delta\tau}+\left[\frac{\partial\hat{R}}{\partial Q}+\frac{\partial\hat{S}}{\partial Q}\right]^{n+1,m}\Delta Q^{n+1,m}=-\hat{R}^{n+1,m}-\hat{S}^{n+1,m} \tag{3.42}$$

For steady-state calculations, the source-like term S dropped from the equation because Δt is set to infinity. Then Eq. (3.42) is simplified for the steady-state calculation as:

$$\frac{1}{J\Delta\tau}+\left[\frac{\partial\hat{R}}{\partial Q}\right]^{m}\Delta Q^{m}=-\hat{R}^{m} \tag{3.43}$$

3.2 Structural solver

The structure part of this study was mainly performed by dedicated and competent co-workers. The authors appreciate the support provided by Prof. Jeeho Lee and the members of LASCOM of DGU. Additionally support from Prof. Changyu Hwang of SVU is also appreciated.

3.2.1 Material models

In general, solid propellant grain exhibits visco-elastic characteristics. In this work, its mechanical response is simulated using the 2nd order Mooney-Rivlin model[17, 18] that has been shown to be quite successful in capturing the small and large strain response of filled elastomers, and the generalized Maxwell visco-elastic model [19] that has been developed to properly describe the energy absorbing behavior of dissipative materials, especially polymeric rubber materials [20].

As a hyper-elastic model, The first order Neo-Hookean model is obtained with N = 1:

$$\Psi = \Psi(J) + C_{10}(\bar{I}_1 - 3) \tag{3.44}$$

And the Cauchy stress can be written as follows.

$$\sigma = pI + 2J^{-1}C_{10}dev(\bar{b}) \tag{3.45}$$

Finally we have the elasticity stress tensor as like

$$c = \tilde{p}1 \otimes 1 - 2pI + J^{-1}\left[\frac{4}{3}C_{10}tr(\bar{b})P - \frac{4}{3}C_{10}(1 \otimes dev(\bar{b}) + dev(\bar{b}) \otimes 1\right]. \quad (3.46)$$

The strain energy density function for the general Mooney-Rivlin model can be written as

$$W = \sum_{j+1}^{N} C_{ij}(\bar{I}_1(C)-3)^i(\bar{I}_2(C)-3)^j + KU(J(C)). \quad (3.47)$$

Then, the consistent tangent stiffness tensor for the 2nd-order Mooney-Rivlin [58] becomes

$$\frac{\partial \sigma}{\partial \varepsilon} \leftarrow 4\frac{\partial^2 W}{\partial C^2} = 4\left(\frac{\partial^2 W_1}{\partial C^2} + \frac{\partial^2 W_2}{\partial C^2}\right) \quad (3.48)$$

$$\begin{aligned}\frac{\partial^2 W}{\partial C^2} &= 2C_{20}(\bar{I}_1 - 3)\frac{\partial^2 \bar{I}_1}{\partial C^2} + 2C_{20}\frac{\partial \bar{I}_1}{\partial C} \otimes \frac{\partial \bar{I}_1}{\partial C} + C_{02}(\bar{I}_2 - 3)\frac{\partial^2 \bar{I}_2}{\partial C^2} \\ &+ 2C_{02}\frac{\partial \bar{I}_2}{\partial C} \otimes \frac{\partial \bar{I}_2}{\partial C} + C_{11}(\bar{I}_2 - 3)\frac{\partial^2 \bar{I}_1}{\partial C^2} + C_{11}\frac{\partial \bar{I}_1}{\partial C} \otimes \frac{\partial \bar{I}_2}{\partial C} \\ &+ C_{11}(\bar{I}_1 - 3)\frac{\partial^2 \bar{I}_2}{\partial C^2} + C_{11}\frac{\partial \bar{I}_2}{\partial C} \otimes \frac{\partial \bar{I}_1}{\partial C}\end{aligned} \quad (3.49)$$

According to the generalized Maxwell visco-elastic model [19] constituted by arbitrary N parallel Maxwell devices, the stress function could be separated into an elastic component and a visco-elastic component as follows.

$$\sigma_i^{n+1} = \sigma_0^{n+1} + \sum_{j=1}^{N} h_j^{n+1} \quad , \tag{3.50}$$

where σ_0^{n+1} is the elastic component, and h_j^{n+1} (the visco-elastic stress contribution of the Maxwell element j) can be written as

$$\begin{aligned} h_j^{n+1} &= \int_0^{t_{n+1}} \gamma_j \exp\left(-\frac{t_{n+1}-s}{\tau_j} \right) \frac{\mathrm{d}\sigma_0(\mathrm{s})}{\mathrm{ds}} \mathrm{ds} \\ &= \exp(-\frac{\Delta t}{\tau_j}) h_j^n + \gamma_j \int_{t_n}^{t_{n+1}} \exp\left(-\frac{t_{n+1}-s}{\tau_j} \right) \frac{\mathrm{d}\sigma_0(\mathrm{s})}{\mathrm{ds}} \mathrm{ds} \quad . \\ &\approx \exp(-\frac{\Delta t}{\tau_j}) h_j^n + \gamma_j \frac{1-\exp(-\frac{\Delta t}{\tau_j})}{\frac{\Delta t}{\tau_j}} [\sigma_0^{n+1} - \sigma_0^n] \end{aligned} \tag{3.51}$$

Here, $d\sigma_0(s)/ds$ is approximated as

$$\frac{d\sigma_0(s)}{ds} = \lim_{\Delta s \to 0} \frac{\Delta\sigma_0(s)}{\Delta s} = \lim_{\Delta t \to 0} \frac{\sigma_0^{n+1} - \sigma_0^n}{\Delta t} \quad . \tag{3.52}$$

τ is the ratio of the damping coefficient to the spring coefficient, and $\gamma_j\left(=\frac{\mu_j}{\mu_0}\right)$ is the ratio of the Maxwell device modulus to the elastic behavior modulus.

3.2.2 WLF models for temperature influence

Temperature has great influence on viscoelastic behavior of a material. The temperature effects can be replaced by a shift factor in time ([59, 60]). For instance, for a E modulus, we have

$$E(T,t)=E(T_0,\xi) \tag{3.53}$$

E (T, t) = E (T_0,x), where T is the current temperature, T_0 the reference temperature, x a reduced time defined by

$$\xi=\int_0^t \frac{dt^{'}}{a_T(t^{'})} \tag{3.54}$$

The a_T coefficient is the shift factor. The chosen behavior is the WLF model developed by Williams, Landel and Ferry [61] from experiments:

$$\log a_T = \frac{-C_1(T-T_0)}{C_2+(T-T_0)} \tag{3.55}$$

where C1 and C2 are constants. These constants, for a large number of polymer materials, are C1 = 17.4 and C2 = 51.6, the implemented shift factor is thus

$$\log a_T = \frac{-17.4(T-T_0)}{51.6+(T-T_0)} \tag{3.56}$$

Note that the temperatures have to be given in Celsius degrees to be coherent with the C1 and C2 numerical values. The validity of this model is for a temperature between T_0 and T_0+100:

$$T_0 < T < T_0 + 100 \tag{3.57}$$

3.3 Combustion solver

While burning modeling is one of the crucial components in simulating a solid rocket motor, actual burning rate of the contained solid propellant is determined by complex physical and chemical combustion phenomena. There are several factors that decide the burning rate of grain, such as chamber pressure, gas velocity along the grain surface, and grain temperature. Although chemical reactions between grain and gases should be fully taken into account [21, 22] for an accurate simulation of the combustion process, this is too complicated and costly. Thus, in this work, pressure and temperature of the grain surface are considered as the key variables of the burning process. The reason not to include the erosive burning caused by gas velocity is that its influence on overall burning rate is relatively small, and some material constants can be obtained only by experiments. The present simulation is based on the assumption of homogeneous propellant grain though most solid propellants used today are classified as composite propellants. Ordinary composite propellant generally consists of an organic fuel that also serves as a binder and a solid oxidizer. High-energetic composite propellants also contain combustible metal particles (ex. Al particle) which increase the energy available for propulsion. Composite propellant has irregular constitution patterns of AP and HTBP, and show non-uniform flame temperature distribution on the grain surface [23, 24]. Thus, it is extremely difficult to draw a realistic and practical numerical modeling for a full-burning simulation. On the other hand, it is reported that, by using well-adjusted assumption of homogeneous model, the overall tendency of internal ballistics of NAWC motor no. 13 could be obtained [25].

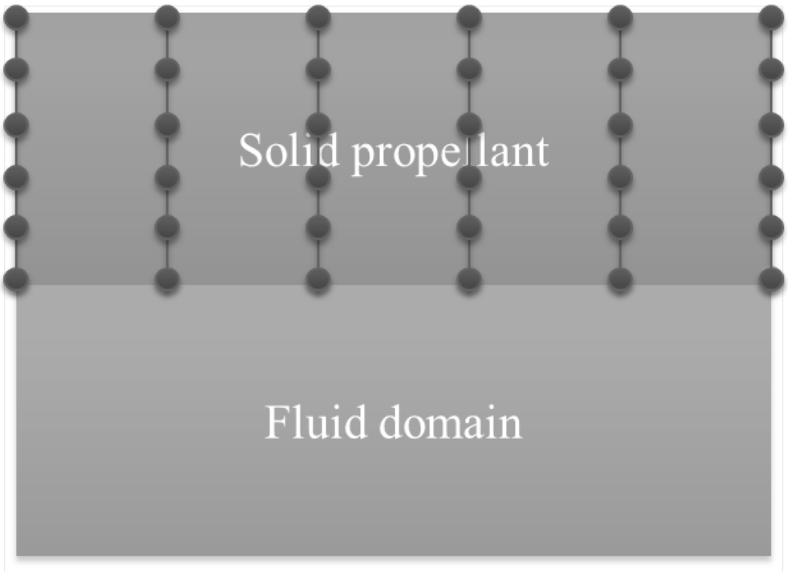

Figure 3.1 Combustion area locates between solid and fluid interface.

A one-dimensional transient burning model [13] is used to efficiently simulate the burning process at an interface between the fluid domain and propellant grain. Though this model is based on the 1-D assumption for regression behavior and homogeneous propellant property, it could be applied to 2-D and 3-D grain geometry by considering independent 1-D lines from each node of propellant surface (see Figure 3.1). This model satisfies Piobert's Law [26]. We assume that grain is heated by hot gas and ignited on its exposed inner surface when the temperature of the grain surface exceeds some specific value. All chemical reactions are assumed to take place within a very short time scale, so that the flow field can be simulated using non-reacting equations. The regression speed of solid propellant surface, r_b, is related to the surface temperature through the following pyrolysis law:

$$r_b = A_c \exp\left(-\frac{E_c}{R_u T_s} \right) . \tag{3.58}$$

If propellant is assumed to be homogeneous, and temperature varies along the direction normal to the surface, so we may assume the burning process to be locally one-dimensional phenomenon. Letting x represent the normal distance from grain surface, the temperature equation for solid propellant grain is given by

$$\rho_s c_p \frac{\partial T}{\partial t} + M c_p \frac{\partial T}{\partial x} = \lambda_s \frac{\partial^2 T}{\partial x^2} , \tag{3.59}$$

where, c_p is the specific heat, $M = \rho_s r_b$ is the mass flux per unit area, and λ_s is the thermal conductivity. The boundary conditions are

$$T\left(-x_{end}\right)=T_{\infty},\quad \left.\frac{\partial T}{\partial x}\right|_{x=0^-}=g(t)$$

$$\text{with } g(t)=\begin{cases}\dfrac{h}{\lambda_s}(T_e-T_s) & : \textit{not ignited}\\[2ex] \dfrac{c_pM}{\lambda_c}\left(T_*^0-T_\infty+T_s-T_*\right) & : \textit{ignited}\end{cases} \tag{3.60}$$

Here, T_e is the temperature at fluid domain surface, T_s is the temperature at solid surface. h is the film coefficient, T_* is the flame temperature, and T_*^0 is the adiabatic flame temperature. T_*^0 is associated with T_* as follows.

$$\frac{\theta}{2}\left[\frac{1}{T_*^0}-\frac{1}{T_*}\right]=\frac{E_c}{R_{uc}}\left[\frac{1}{T_s^0}-\frac{1}{T_s}\right]\ . \tag{3.61}$$

The steady state surface temperature T_s^0 is evaluated by comparing the pyrolysis law, Eqn. (3.58), to the experimental power law.

$$r_{bs}=A_c\left(\frac{P_e}{p_{ref}}\right)^{n_p}\ , \tag{3.62}$$

where p_{ref} is the reference pressure, r_{bs} is the steady state burning rate, P_e is the pressure of fluid domain, and A_c and n_p are constants [13].

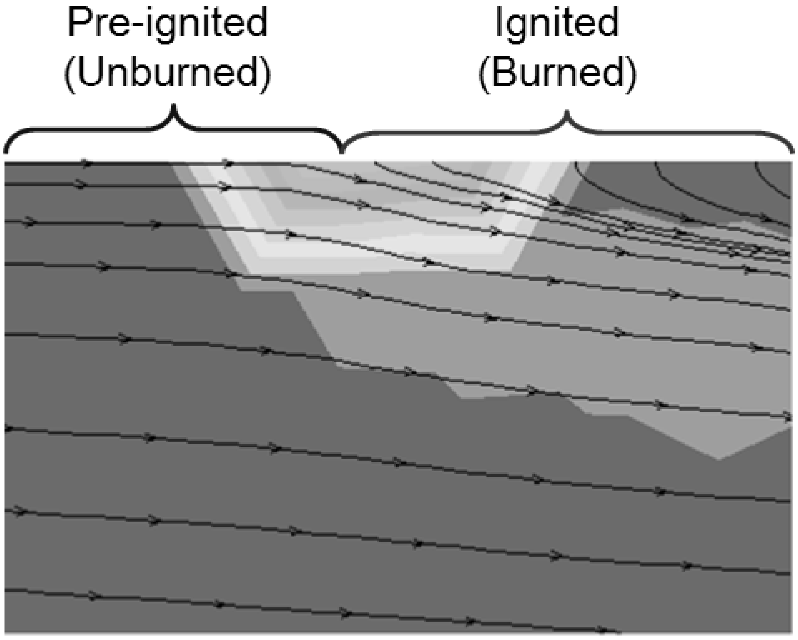

Figure 3.2 The difference of boundary conditions of fluid region: pre-ignited wall condition versus ignited mass flow rate condition

3.4 Spatial and temporal data transfer scheme

In FSI simulation, a flow solver needs deformation data of structural surface, while a solid solver needs pressure data of fluid interface. Since mesh size between fluid and solid domain is not generally the same, a non-matching interface between fluid and solid domain should be assumed. Accurate data transfer along the non-matching mesh interface is an indispensable condition for successful FSI simulations [24]. This requires a non-oscillatory and conservative 1-D data transfer scheme along the non-matching interface. In addition, re-meshing process in fluid and solid domain is necessary to maintain the initial mesh quality, which requires a 2-D data transfer scheme between old and new meshes.

The essential requirements of data transfer scheme are accuracy and conservation. For accuracy, the magnitude of some error norm must be minimal, and for conservation, the sum of transferred property at both fluid and solid interface must be the same. Non-conservative schemes, such as TPS, MQ, and Cubic-spline, may ensure accuracy, but suffer from the conservation requirement. With non-conservative schemes, we need fine meshes for both fluid and solid domain. Conservative schemes, such as node projection or quadrature projection schemes, may suffer from the accuracy requirement when fluid-solid grids mismatch along the interface. The lack of accuracy and/or conservation can affect computed results not only along the interface but also over the entire computational domain. From this perspective, common refinement data transfer scheme [25] is attractive since its error is almost independent of the element mismatch along the interface. Thus, we adopted the common refinement data transfer scheme for 1-D data transfer at which conservation is a crucial requirement [26]. In case of 2-D data transfer, accuracy is much more important than conservation, and thus the cubic spline interpolation scheme is employed to provide a sufficient accuracy with an acceptable computational cost.

While the time step size should be determined by the CFL condition in both fluid and solid domain, the allowable time step of each domain is not the same [13, 18]. The temporal mismatch may become even larger if implicit time marching scheme is employed. As an efficient and robust integrated algorithm to couple temporally unmatched solvers, we adopt conventional serial staggered scheme [27, 28]. Dirichlet velocity boundary condition and Neumann momentum boundary condition are implemented along the fluid-solid interface.

$$u_s = u_f \quad \text{: Dirichlet condition for displacement,}$$

$$t_s = t_f \text{, where } t_f = p_f n_f - \sigma_f \cdot n_f \text{ and } t_s = \sigma_s \cdot n_s \text{ : Neumann condition for traction.} \qquad (3.63)$$

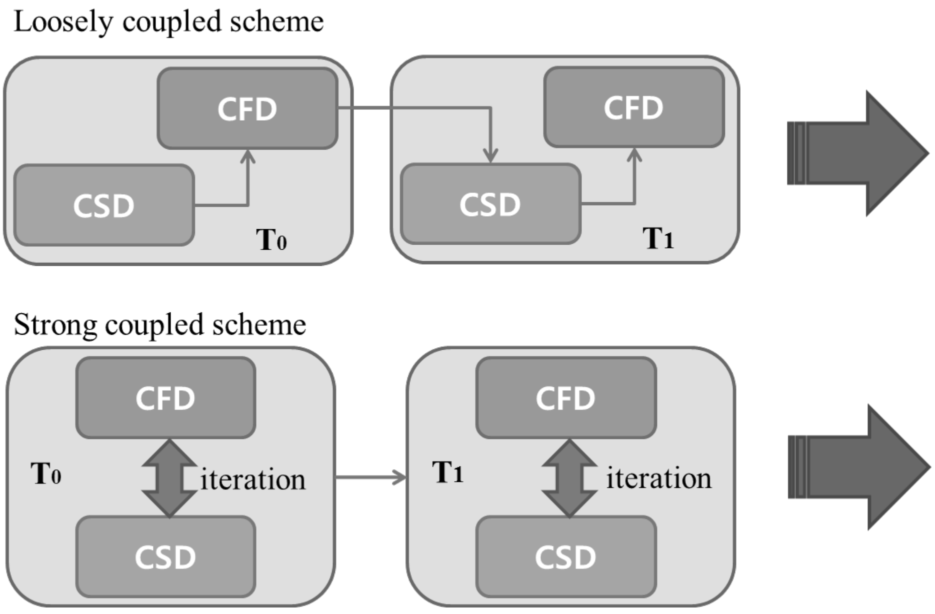

Figure 3.3 Loosely coupled scheme and strong coupled scheme for FSI time marching

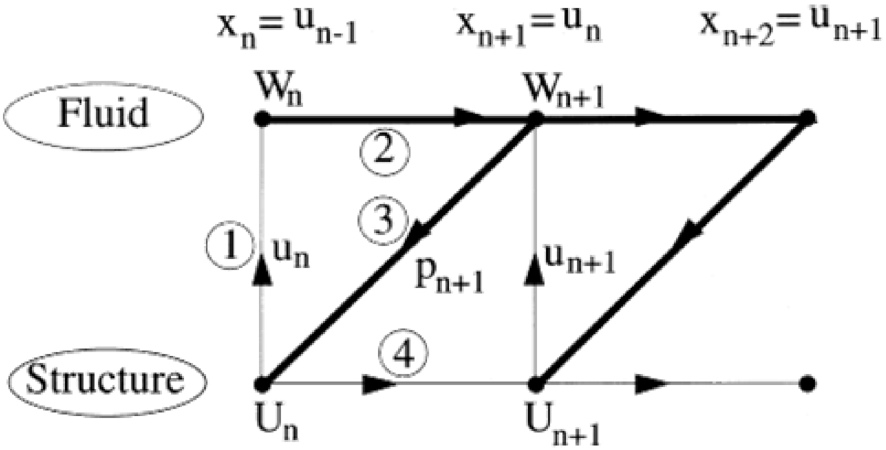

Figure 3.4 Conventional serial staggered procedure

3.5 Dynamic mesh treatment

For fluid simulation, unstructured mesh is adopted to handle complex geometry. Dynamic analysis in solid domain is performed using a 4-node rectangular element. The initial meshes of fluid domain are generated by the Delaunay-based triangular mesh generation technique with the Rebay's point insertion method [29]. In order to treat substantial geometrical changes due to the deformation and burnback of grain, an automatic mesh update procedure has been implemented to guarantee a high quality mesh during simulation. The mesh regeneration procedure is performed locally when a certain local geometric change occurs, and entirely when global or excessive geometric change takes place so that the local mesh handling cannot maintain mesh quality any longer. The Rebay's point insertion technique combined with the Delaunay triangulation based smoothing [30, 31] is used as a baseline re-meshing for fluid domain. For solid domain, we regenerate 4-node meshes using the Paving method. [62, 63]

3.6 Surface regression model

During burnback process, the solid propellant grain with slot geometry usually leads to a topological change into two sub-regions. After a while, one of the separated lumps is fully burned away while the other sub-region still remains. The integrated simulation needs the capability to handle such topological change. In addition, solid propellant grain has two types of corners (convex and concave corner), and each has a different burn back characteristic [32]. According to solid grain burning experiments, convex corner, from a solid grain point of view, maintains its initial corner angle, while concave corner is evolved into a curved surface (see Fig. 3.5). For the accurate shape tracking of the solid propellant grain while satisfying the Piobert's burnback law [23], we developed a regression model by reproducing and/or redistributing the surface nodes of solid propellant to maintain high quality initial meshes.

Figure 3.6-(a) shows the typical problem case of convex corner. If it is burned with same distance along normal to the surface, the corner point loose its initial angle and distort the corner shape. So regression model cure this problem using neighbor points and their angle as shown in Figure 3.6 (b).

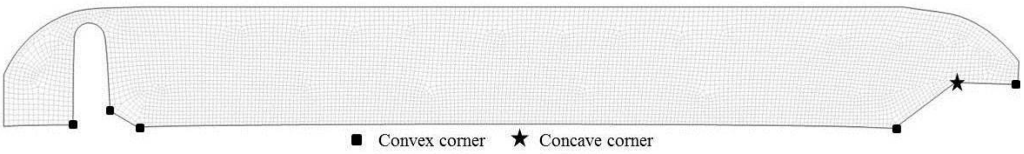

Figure 3.5 Solid domains with corners

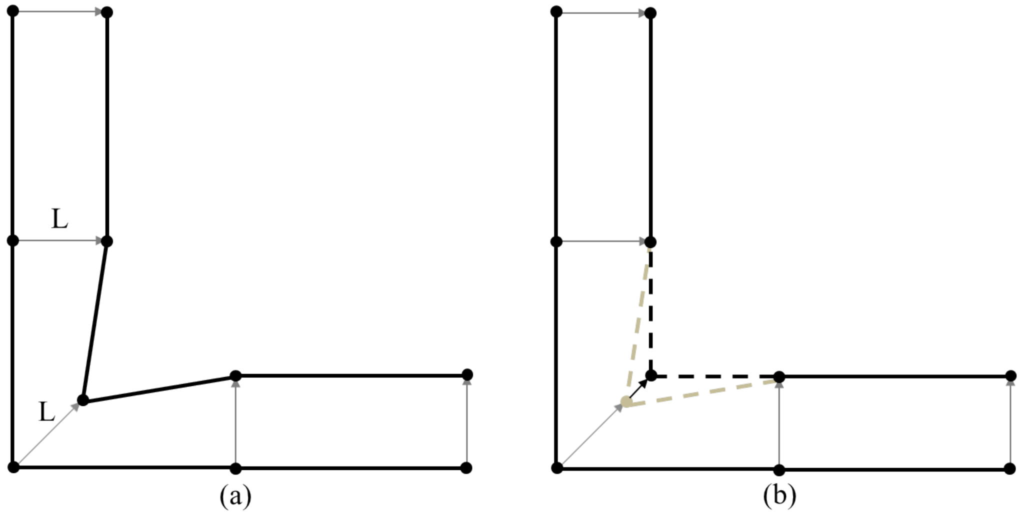

Figure 3.6 (a) problem of convex corner (b) re-positioning concept of regression model

3.7 Virtual contact line method

As shown in Fig. 3.7, most solid rocket motors have a narrow crevice called the boots gap between the propellant grain and the rocket case. The role of the boots gap is known to prevent an unexpected structural failure due to severe thermal deformation. Thus, the unsteady behavior of the boots gap must be included in the FSbI simulation. The hot gas created by the propellant burning rapidly propagates to the rocket nozzle area. The gas flow passing the boots entrance produces a series of expansion fan and shock wave due to geometric constraint. In particular, the shock impingement and reflection act as a strong pressure load on the grain surface, and the propellant grain is pushed toward the vertical direction. As a result, the boots gap becomes progressively narrower to lead a structural contact problem. The boots contact problem is physically quite reasonable, but it imposes a numerically challenging situation. Under the boots contact situation, the mesh size in fluid domain is infinitesimally small and the time step size becomes practically zero.

In order to prevent the contact situation while maintaining the boots effect, a technique based on a virtual contact line is introduced. The basic idea is quite simple in a sense that the boots gap is required to maintain a minimal distance to make fluid analysis possible. We set a virtual boundary line as shown in Fig. 3.7, across which the grain movement is prohibited. In other words, if the grain surface touches the line, it is regarded as the contact condition and further movement across the line is prohibited. The propellant surface is then pushed back by a sufficiently high-pressure load from the boots gap inside. The virtual contact condition is then negated, and the grain is allowed to move normally.

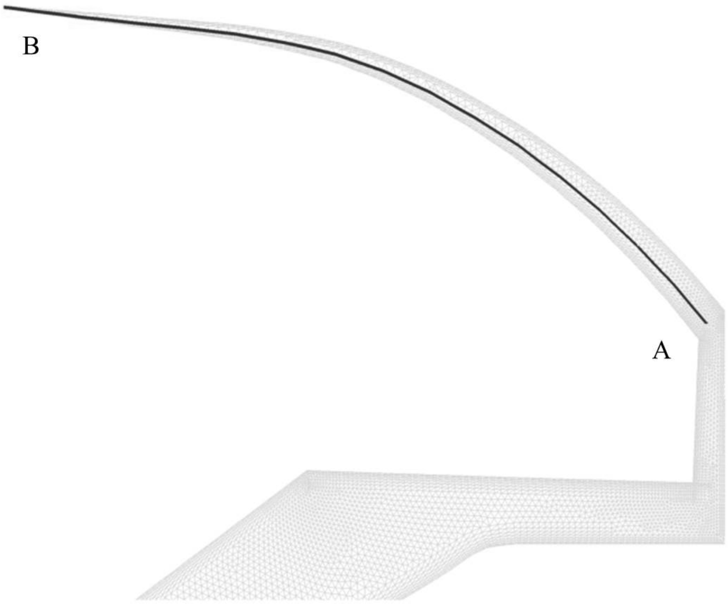

Figure 3.7 Virtual contact line

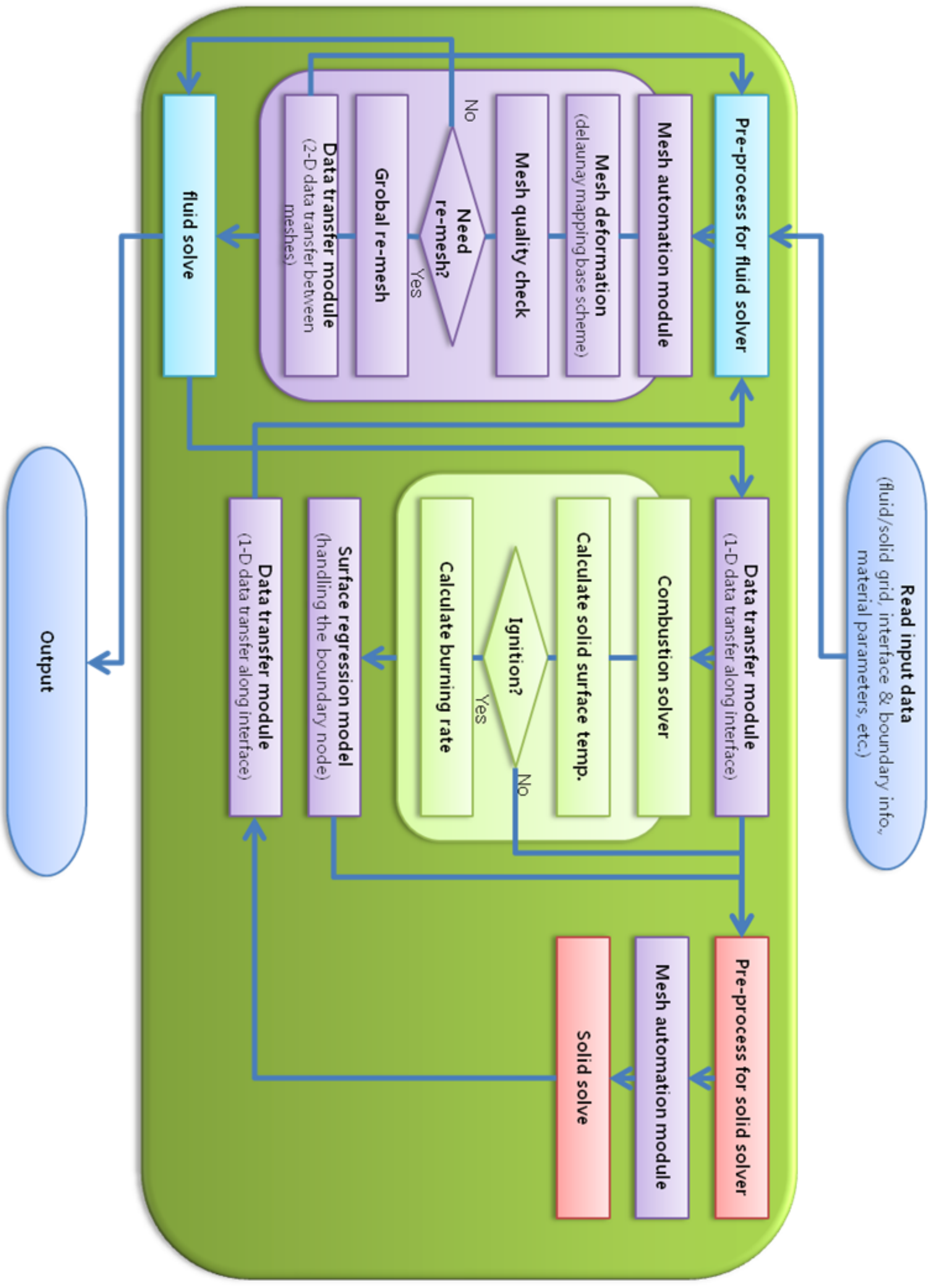

Figure 3.8 Integration flow chart for FSI rocket simulation

Chapter IV

SIMULATION RESULTS

4.1 Validation problem

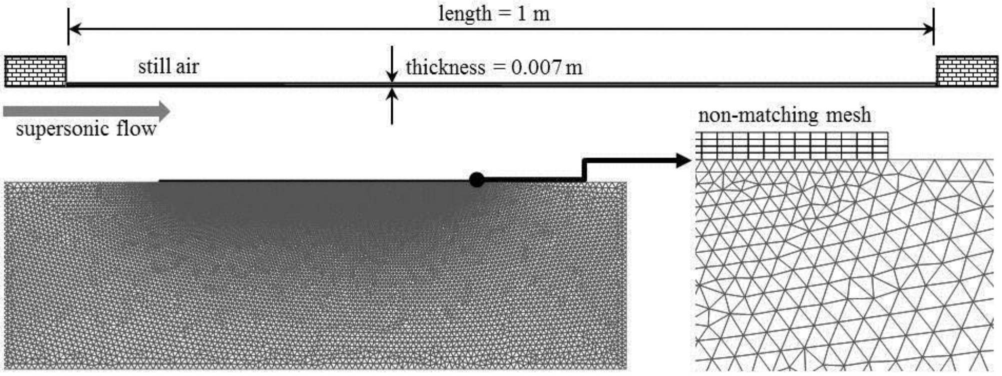

Figure 4.1 Geometry of panel flutter and non-matching fluid-solid interface

In order to examine the reliability of the present FSI simulation, we firstly perform a problem of panel flutter as a validation case. Nelson and Cunningham studied this problem with some assumptions to analytically determine the effect of the Mach number on the stability boundary of a panel subjected to low and high supersonic air flow passing below while its upper surface is exposed to still air [33]. Figure 4.1 shows the geometry of the panel flutter used for this simulation. The length of the panel is 1 m and its thickness is 0.007 m. The plate is assumed to be elastic with a Young's modulus of 77.28 Gpa, a Poisson's ratio of 0.33, and a density of 2710 kg/m3. The panel is made of flexible material but both ends are clamped like a bridge. In this work, the supersonic air flow has a free stream Mach number of 1.2 to 1.7, a uniform initial pressure of 0.1 Mpa, and a density of 1.225 kg/m3. To initiate the dynamic response of the plate, the following panel displacement is introduced as a small incipient perturbation.

$$\delta(x) = \frac{\delta_{\max}}{2}\left[1-\cos\left(2\pi\frac{x}{l}\right)\right] \quad . \tag{4.1}$$

Here, $\delta_{\max}$ is taken to be 3 mm, and l is the length of panel (1 m). The maximum displacement is located at the center of the panel, and the initial displacement is magnified or subdued through the interaction between supersonic external flow and elastic panel structure. Nelson and Cunningham analyze this problem to show the theoretical result in Fig. 4.2. The horizontal axis shows the Mach number of external supersonic flow, and the vertical axis is the ratio of thickness to panel length. By analyzing the 1st and 2nd vibrational mode of the panel, a stable and unstable region can be obtained. The bold dotted line in Fig. 4.2, which combines the stability boundary of each mode, is the borderline between the stable and unstable region. We compare the computed results with the theoretical analysis. The theoretical critical Mach number separating the stable and unstable region is approximately 1.432.

Figure 4.3 shows the simulation results of the displacement at the panel center where the maximum temporal deformation can be observed. The dynamic response at the panel center is used to judge whether the initial deformation is going to be stable or not. We change the external supersonic flow from the Mach number of 1.2 to 1.7 with 0.1 steps and assume the flow is inviscid. As shown in Fig. 4.3, from the Mach number 1.2 to 1.3, the initial displacement of the center point increases and unstable behavior appears. The result of the Mach number 1.4 shows a nearly neutral stable condition by almost maintaining the initial displacement. If the Mach number is close to 1.5, the initial displacement is completely subdued. This indicates that the critical Mach number is located near 1.4, showing a little discrepancy with 1.432 of the theoretical result. Nelson and Cunningham obtained the pressure perturbation of the external flow by introducing the velocity potential [34]. In other words, the theoretical result is based on the assumption of the shock-free inviscid flow with small incidence, so that the linearized flow theory is applicable. In computed results, however, the nonlinear effect by shock waves is observed, particularly in cases of high incidence and high Mach number flows where the linearized theory with small perturbation is somewhat limited. The pressure force induced by shock wave pushes the panel in the opposite direction to the panel oscillation, so that it brings an effect to attenuate the panel oscillation. This seems to be the reason for the small discrepancy observed between the computed result and the theoretical analysis. Even though the nonlinear effect is not included in the theoretical analysis, the stability behavior predicted by the two results is almost the same.

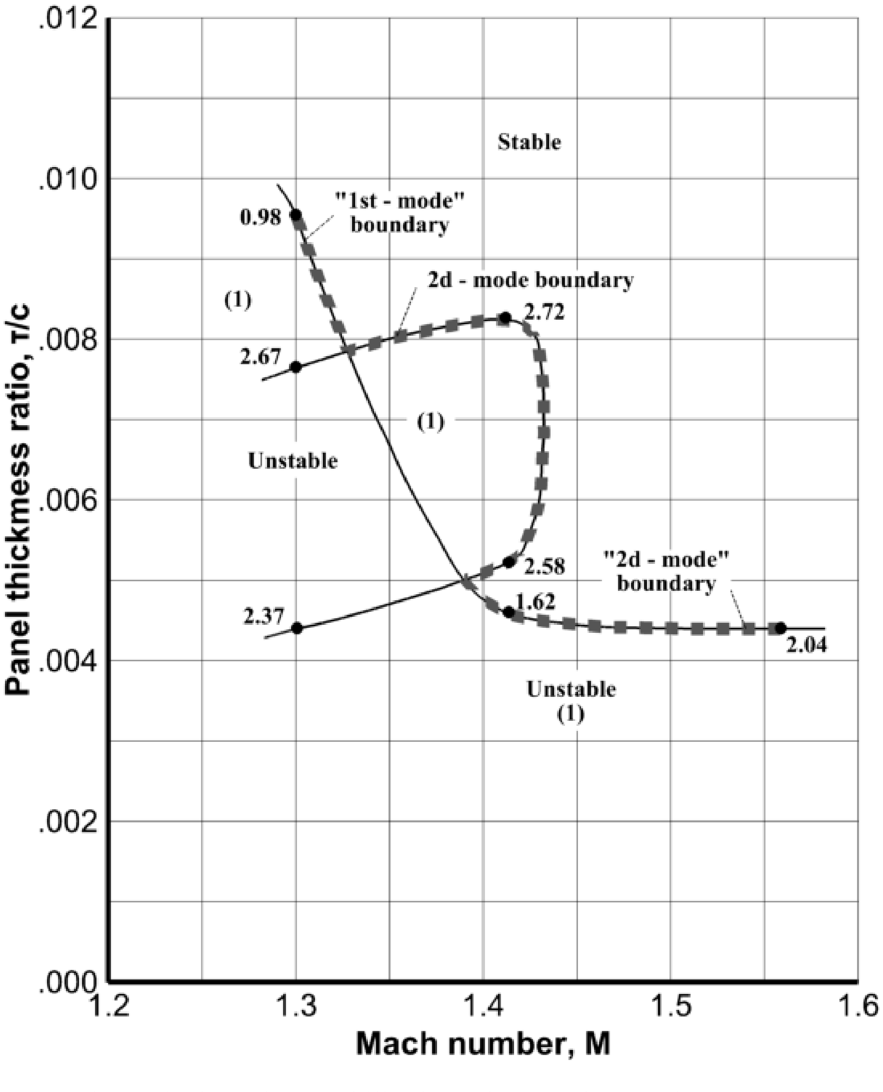

Figure 4.2 Theoretical result of stability boundary (Nelson and Cunningham, Ref. 28)

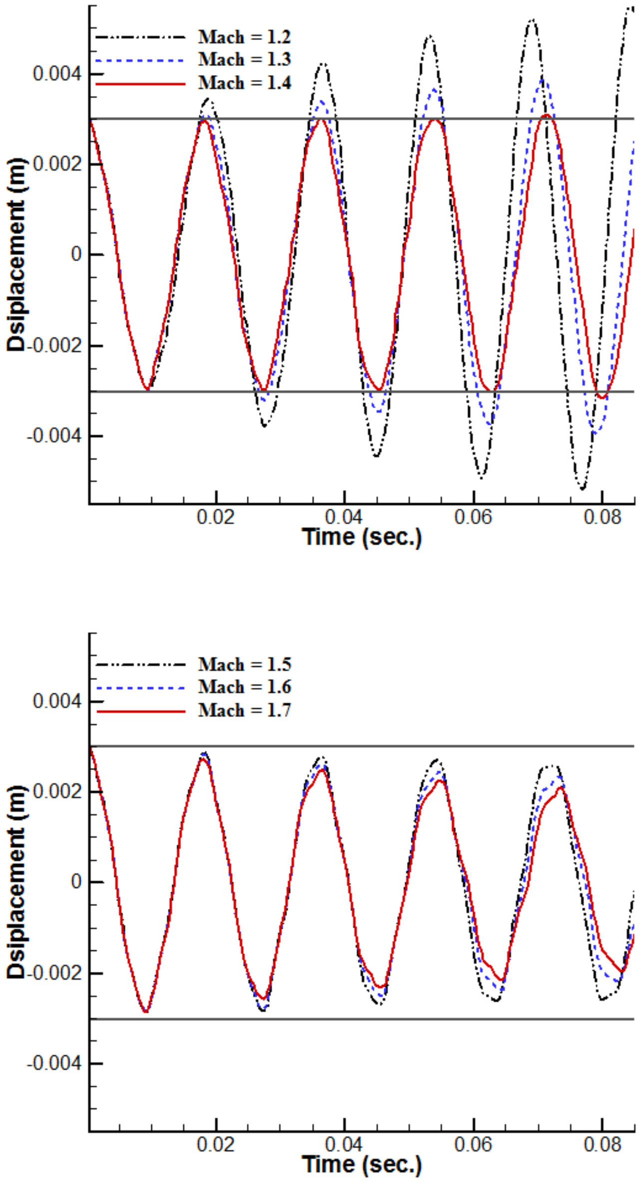

Figure 4.3 Numerical results: dynamic response at the panel center

4.2 Validation problem

The panel flutter problem as a validation case was chosen to confirm the FSI ability of the integrated code. We agree with the reviewer’s comment in a sense that this validation case was not enough to demonstrate that the code is ready to apply to rocket burning simulations. At the same time, however, it is very difficult, even for academic purpose, to obtain experimental data of solid rocket motor containing structural responses.

In order to demonstrate the fidelity of the integrated code, we carry out another validation test using ground firing test data of the following rocket motor. This experimental test was carried out by Agency of Defense of Development (ADD), Korea, and it has been published by H. Han [41]. Figure 4.4 shows the axisymmetric shape of the rocket motor used in the experimental and numerical research. Distinctive feature of this rocket is that the forepart of propellant grain has a curved surface and it changes the burning area of propellant surface. At the forehead of chamber, there is narrow lengthy hole to measure the chamber pressure in the experiment. Therefore, in the numerical simulation, the pressure history was measured in this point (see Fig. 4.4). The rocket cases, nozzle, and other rocket components ware included to the FSbI simulation. Table 4.1 shows the propellant characteristics for burning model based on Han’s work [41].

In the experiment, the ignition was took place by additional explosive material but the exact location was not stated and assumed to be at the center of combustion chamber. Therefore we started ignition at some points artificially as shown in figure 4.5. Figure 4.5 also show the flame propagation process of propellant surface.

Figure 4.6 shows the intermediate temperature and displacement distributions of the FSbI simulation. All grain surfaces produce the mass flow to fluid domain but temperature distribution at the center part and backside cavity of the combustion chamber is relatively lower, while density distribution is relatively higher. Displacement distribution indicates that solid propellant is being pushed to the radial direction but other rocket components do not show a noticeable deformation. This is because TPEM motor was designed for ground firing test and thus the rocket case is thicker. Figure 4.7 shows a shape just before the full-burning of contained propellant. Figure 4.8 compares the pressure history between experimental data and computed results. The pressure development history of both results exhibits the same tendency, though there is a slight discrepancy. The difference is particularly visible at the early stage of simulation. Such discrepancy appears to come from the fluctuation caused by unsteady acoustic waves existing near the measuring point at the early stage of simulation. Nonetheless, the overall computed pressure history well matches experimental data, demonstrating that the developed integrated code is capable of predicting the general performance of solid rocket burning.

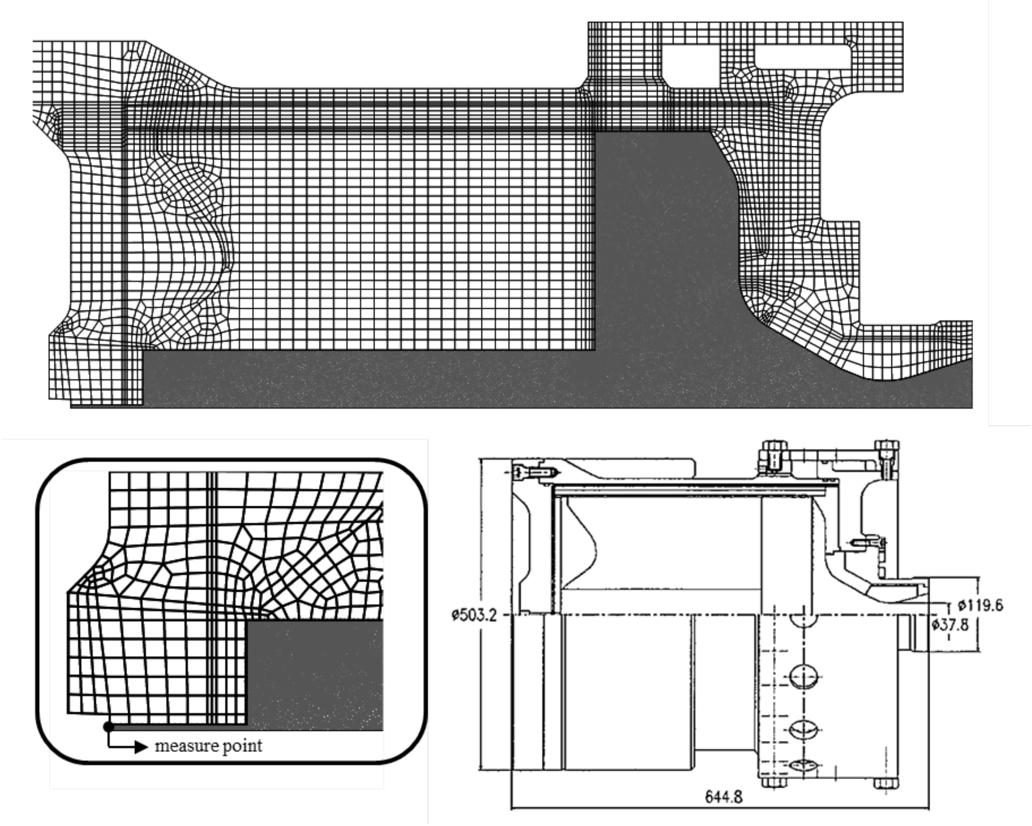

Figure 4.4. Geometric shape of TPEM solid rocket motor

Propellant properties	
a (of APN model)	0.0277 inch/sec
n (of APN model)	0.44
Reference pressure	1000 psia
Propellant density	1.8 g/cc
Adiabatic flame temperature	3539 K
Ignition temperature	850 K

Table 4.1 Propellant burning properties of TPEM rocket motor

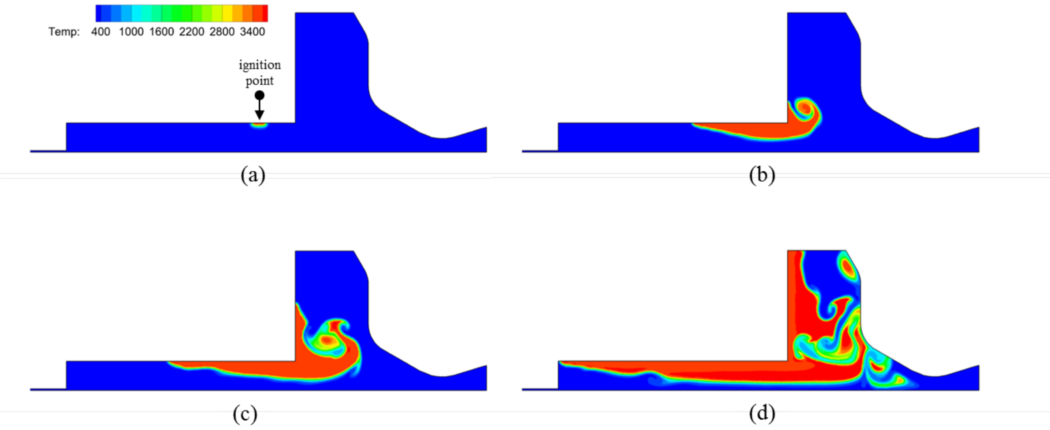

(a) (b)

(c) (d)

Figure 4.5 Flame propagation process of TPEM rocket motor

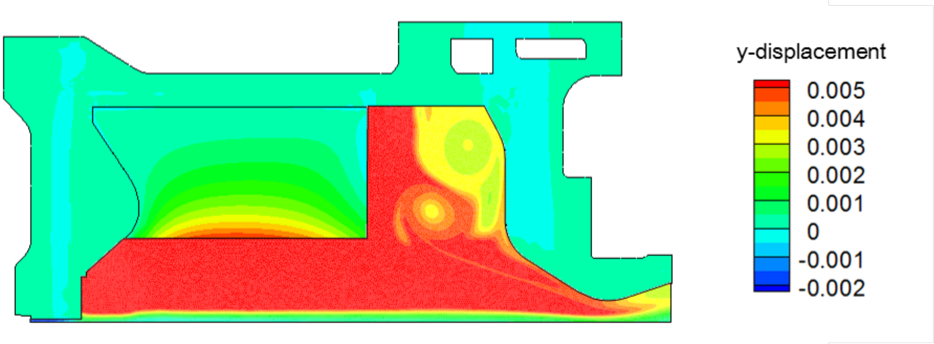

Figure 4.6 FSbI simulation results of TPEM motor (displacement legend for structural contour)

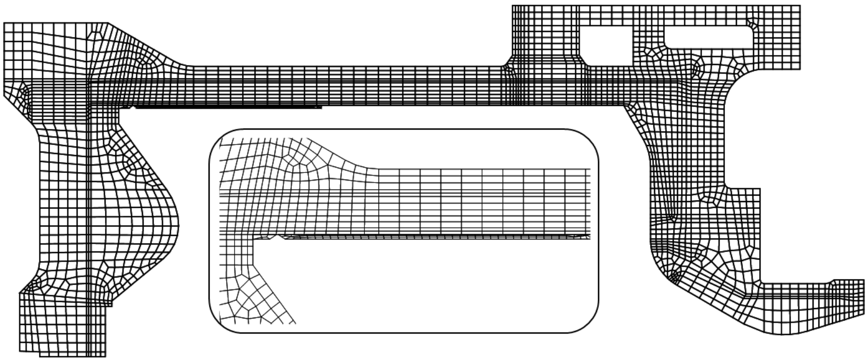

Figure 4.7 Full-burning shape of contained propellant

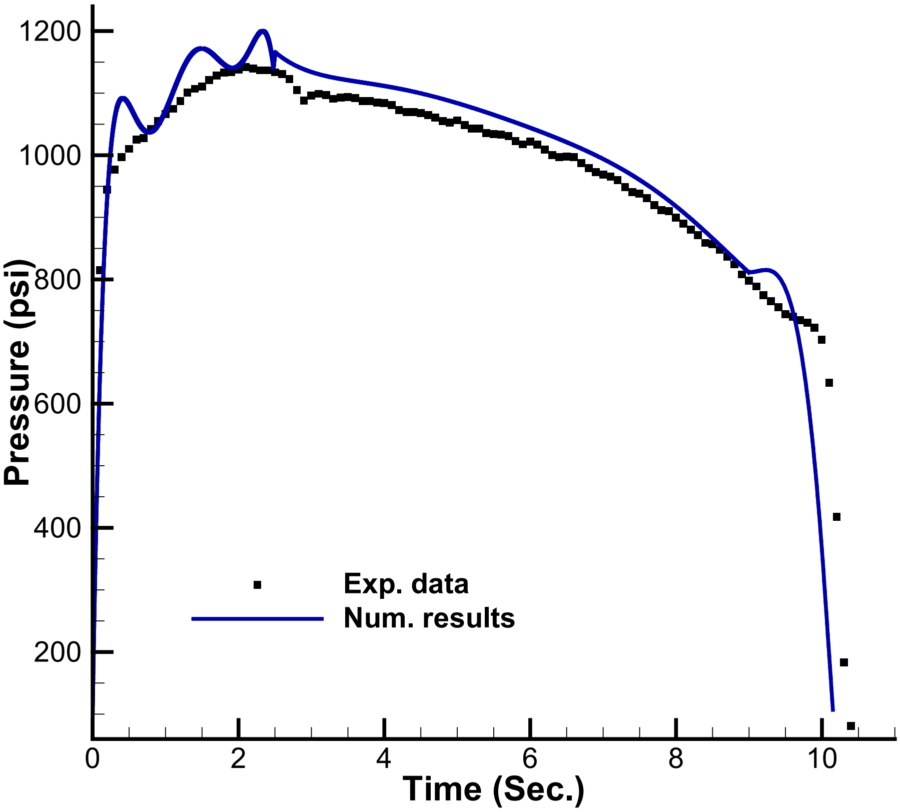

Figure 4.8 Pressure history between experimental data and numerical results

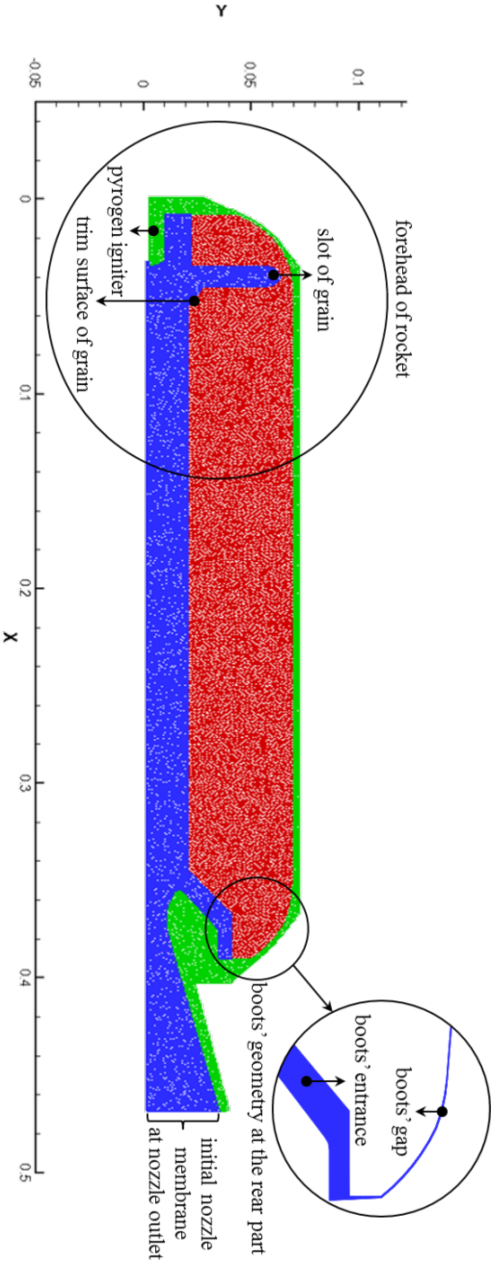

Figure 4.9 Rocket geometry for simulation

4.3 Rocket modeling and thermal analysis

Figure 4.9 shows a typical 2-D axisymmetric rocket geometry designed for the purpose of simulation. The blue color indicates the empty space of combustion chamber as an initial fluid domain, which is going to be enlarged as the propellant grain start to burn. The red color shows the deformable structure domain (or the solid propellant grain), and the green color is the undeformable structural part composed of the rocket case, igniter, and the nozzle. At the forehead of combustion chamber, there exist a pyrogen-type igniter and a slot geometry. The pyrogen-type igniter is modeled to eject an initial hot gas, which makes the grain ignited. At the rear part of the rocket motor, there are a boots geometry which is a narrow gap between the propellant grain and the rocket case, and a boots entrance part. At the nozzle outlet, there is a thin nozzle membrane that blocks the outflow through the nozzle. When the average pressure on the membrane reaches a specific value (6 atm), the nozzle membrane is broken and the pressurized flow is spouted out through the nozzle outlet. The boundary conditions for the flow analysis are listed in Table 4.2. The solid propellant is assumed to be elastic or visco-elastic with a Young's modulus of 63.039 Mpa, a Poisson' ratio of 0.499, and a density of 1800 kg/m3 The shear modulus of solid propellant is obtained from the following relation.

$$G = \frac{E}{2 \cdot (1+\nu)} \simeq \frac{E}{3} \tag{17}$$

The material properties for structural response are shown in Table 4.3 and Fig 4.10 shows its relaxation curves. The ignition temperature of propellant is 850K in this simulation. The hot gas from the igniter heats up the exposed surface by convection. Then, the surface temperature of combustible substance rises gradually. When it reaches 850K, the propellant surface takes fire spontaneously and continues to burn.

	Boundary conditions		
Igniter inflow	Constant mass flow rate		Inflow velocity = 1016m/sec Temp. = 2500K Pressure = 7.011E+06 Pa
Solid and propellant surface	Wall	Inviscid	Slip condition
		Viscous	No-slip condition
	Propellant	Before ignition ($T_s < 800$ K)	Wall condition
		After ignition (burning)	Mass flux from 1-D combustion module
Axis	Axisymmetric condition		
Nozzle outlet	Before membrane broken (P < 6 atm)		Wall condition
	After membrane broken		Supersonic outlet

Table 4.2 Boundary condition for FSbI analysis

Master relaxation curve	
P-material	$E_{rel}(t/a_T)/E0$ = 0.27585*exp(-x/1.E-6) + 0.39853*exp(-x/1.E-5) + 0.15701*exp(-x/1.E-4) + 0.0862*exp(-x/1.E-3) + 0.02623*exp(-x/1.E-2) + 0.02026*exp(-x/1.E-1) + 0.00916*exp(-x/1.E0) + 0.00555*exp(-x/1.E1) + 0.00213*exp(-x/1.E2) + 0.00322*exp(-x/1.E3) + 0.015863 E_0 = 630.393 bar, E_{eq} =10 bar, v = 0.499 Log(t/a_T) = -5.854(T(℃) - 20) / (170.47 + (T - 20)) Thermal expansion coefficient a = 0.87E-4 (/℃)
Stress free temperature T_0 = 60℃ for all materials	

Table 4.3 Material properties of solid propellant

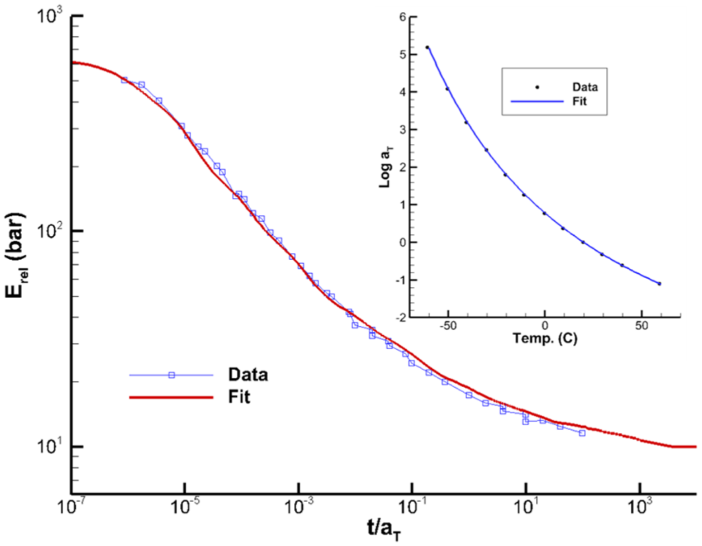

Figure 4.10 Relaxation curves of solid propellant

Before carrying out a full burning solid rocket FSbI simulation, we initially performed a thermal analysis of the propellant grain. It is known that the manufacturing temperature of the solid propellant grain is about 60 °C but the safekeeping temperature is about -40 °C. As a result, the propellant grain is deformed due to the thermal load induced by temperature discrepancy. Such structural deformation may provoke a change in the flow characteristics that could cause unexpected rocket failures. We firstly simulate this process to examine the effect of the thermal load and geometry deformation. The deformed geometry is then adopted as an initial shape in the full-burning FSbI simulation. Figure 4.11 shows the simulation result that is compared with Abaqus data. We decreased the temperature from 60 to -40 °C over 1400 minutes, and maintained the temperature for approximately 3000 minutes. The displacement was then obtained at the center of the grain surface. A slight difference is observed between the two results, but its magnitude is quite small (less than 1%) compared to the radial length of the propellant grain.

Figure 4.12 compares a geometrical change in combustion chamber before and after the thermal deformation. A noticeable change near the boots geometry can be observed. The boots geometry is generally designed to prevent failure due to the thermal load, like the gaps in railway line. During the thermal analysis, the propellant grain shrinks as the temperature decreases, and as a result, the boots gap grows as in Fig. 4.12. Since the boots gap may play a significant role in the dynamic response of fluid-structure interaction, it is included in the full-burning FSbI simulation.

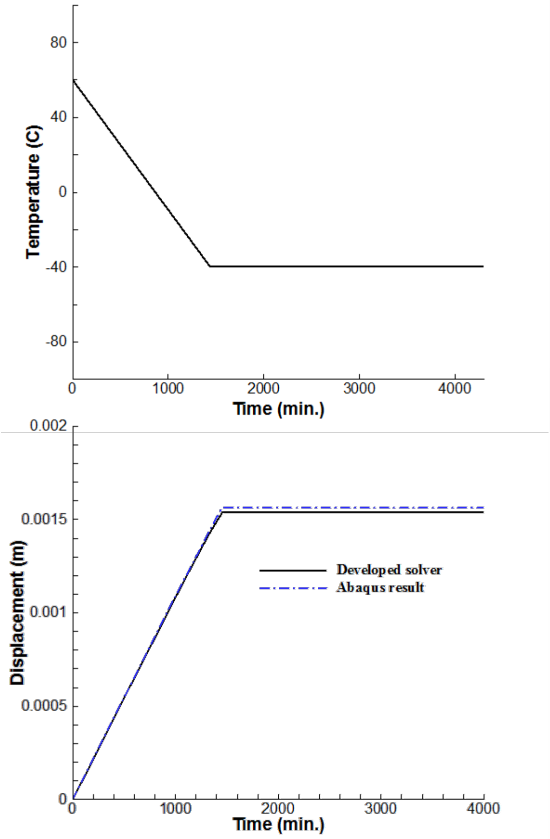

Figure 4.11 Numerical results: comparison of thermal analyses

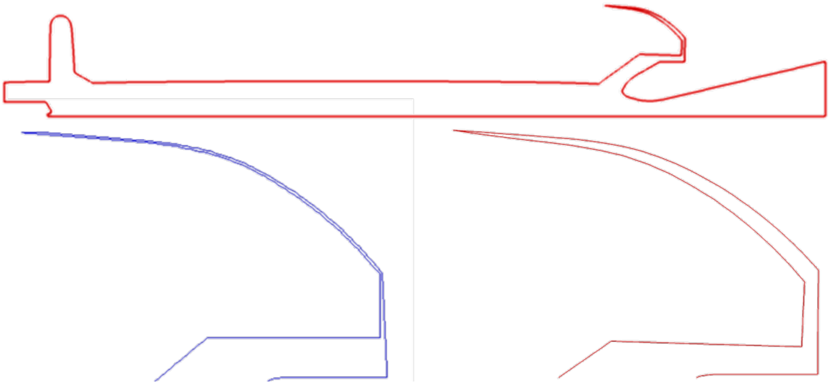

Figure 4.12 Numerical results: geometrical change of the boots' part due to thermal deformation

4.4 Rocket simulation results

Figure 4.13 shows the FSbI simulation results with the inviscid flow solver to examine the initial flow field development, the ignition process, and the flame propagation process along the grain surface in the forehead of combustion chamber. The initial flow field develops from the hot gas ejected from the pyrogen-type igniter (Fig. 4.13-(a)). The convection of the hot gas heats up the exposed grain surface near the trimmed slot surface (Fig. 4.13-(b)), and the area around the trimmed surface is firstly ignited to send out mass flux normal to the grain surface (Fig. 4.13-(c)). The flame from the ignited surface heats the surrounding region (Figs. 4.13-(d) and (e)), and the forehead of the propellant grain is ignited almost simultaneously with the trimmed surface (Fig. 4.13-(f)). The flame propagates rapidly along the grain surface while the propagation inside the slot is rather delayed. This is because the slot area is congested with the initial cold air (Fig. 4.13-(g)). At the end of initial stage, the chamber is finally filled with the hot emission gas and the entire grain surface produces a mass flux (Fig. 4.13-(h)).

From the inviscid simulation results in Fig. 4.13, the high temperature gas ejected from the igniter plays an important role in developing the initial flow fields and heating the exposed grain surface. This indicates that an accurate prediction of the initial flow physics is essential in determining the initial burning position and time of the grain surface. In general, mass flux sweeps away boundary layer on the grain surface, and viscous effect near the grain surface may be neglected. Reasonable results can be obtained by inviscid simulations only. At the early stage of ignition process (or ignition transient phase), however, complex unsteady flow physics influences the ignition at the grain surface, and the ignition delay time. Besides, the existence of the slot, nozzle and boots puts additional geometric complexity. The Navier-Stokes computations with the

Spalart-Allmaras turbulence model are thus carried out to include the viscous and turbulence effects [35-37].

Figure 4.14 is the integrated simulation results with the viscous flow solver. Though not taken at the same instant, the sub-figures in Fig. 4.14 are listed in chronological order as in Fig. 4.13 to compare the distinguishing flow development and ignition process with the inviscid results. From the view point of the overall flow development and flame propagation process, major flow physics observed in Fig. 4.14 is quite similar to the inviscid results of Fig. 4.13. The hot gas heats the trimmed surface to ignite firstly (Fig. 4.14-(c)), and the flame front spreads out along the grain surface (Fig. 4.14-(d)). The flow and flame development pattern that observed in the first four sub-figures of Fig. 4.14 corresponds to that of Fig. 4.13.

A closer look at the two cases, however, shows that the detailed flow pattern is somewhat different. In particular, temporal ignition and flame propagation along the grain surface are remarkably delayed in the viscous results. Though most of the cold gas that initially filled combustion chamber runs out, some of the initial cold gas remains inside chamber and causes the flame propagation delay. As shown in A and B of Fig. 4.14-(e), the burning gas and geometric shape of chamber blocks the passage of the initial cold gas. In other words, there is no passage as in region A or only a very narrow passage exists as in region B. Thus the initial cold gas in these regions is compressed and has a higher density. In fact, this is commonly observed in both viscous and inviscid results. However, the propagation delay induced by the compressed cold gas predominates in the viscous results, which seems to be caused by wall boundary condition. In the inviscid simulation, high temperature gas from the ignited surface can be readily transported into the neighboring un-ignited region by a tangential slip flow along the grain surface, while no slip boundary condition in the viscous simulation excludes the tangential velocity component.

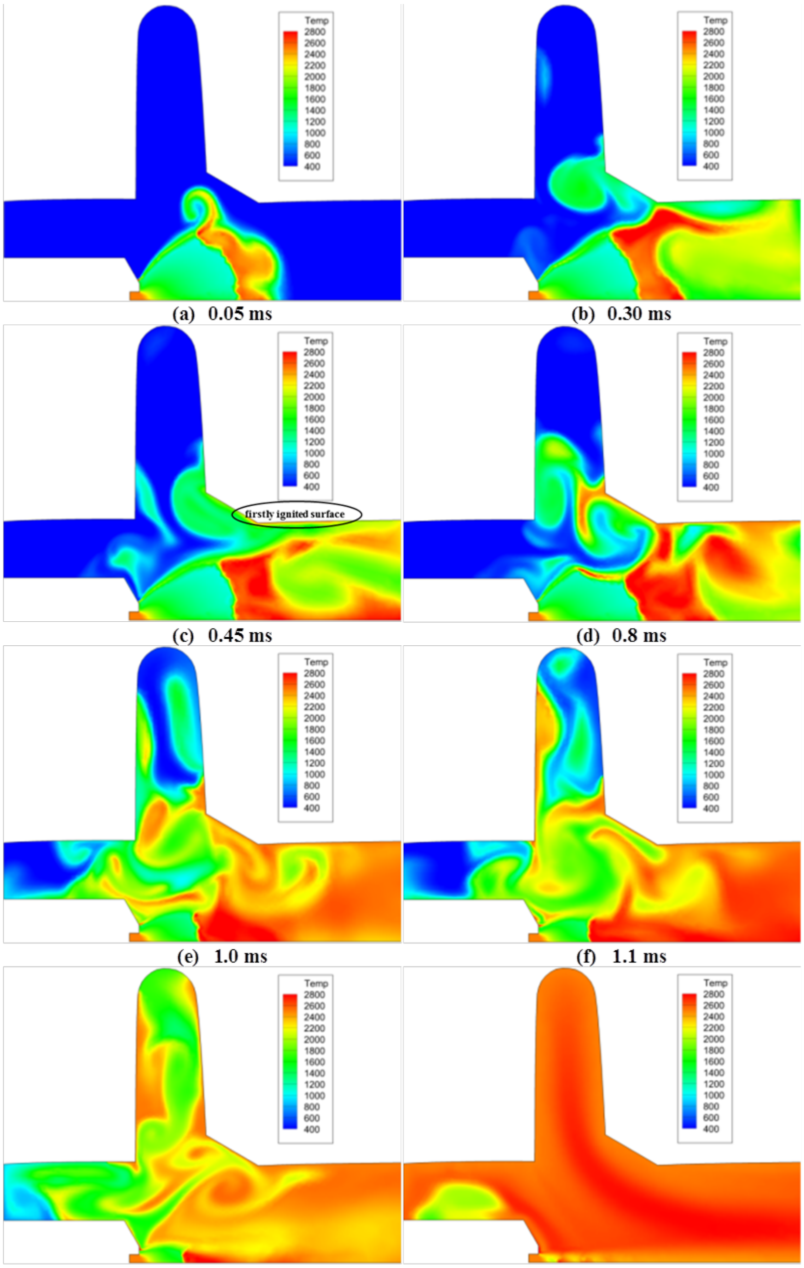

(a) 0.05 ms (b) 0.30 ms

(c) 0.45 ms (d) 0.8 ms

(e) 1.0 ms (f) 1.1 ms

(g) 1.3 ms (h) 5.0 ms

Figure 4.13 Numerical results: ignition, flame propagation, and flow development process in combustion chamber (inviscid flow solver)

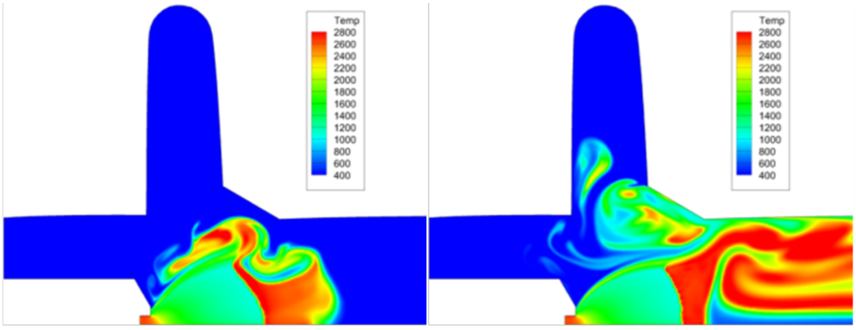

(a) 0.06 ms (b) 0.50 ms

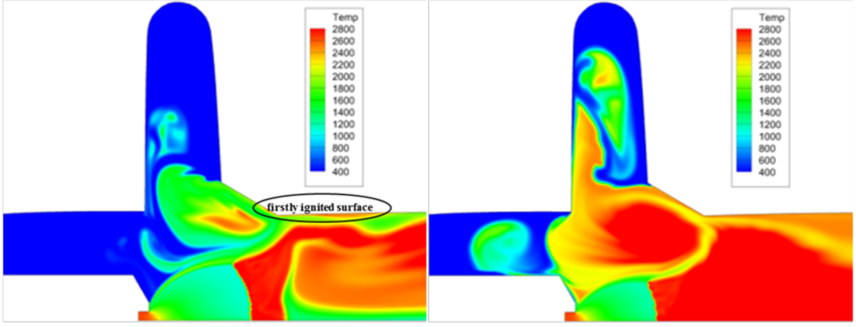

(c) 1.0 ms (d) 1.7 ms

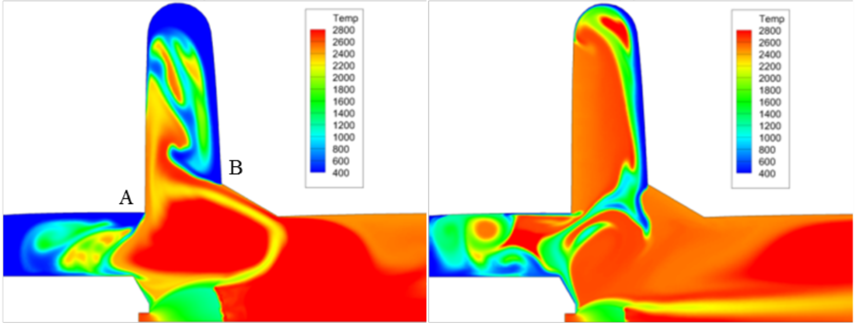

(e) 1.9 ms (f) 3.2 ms

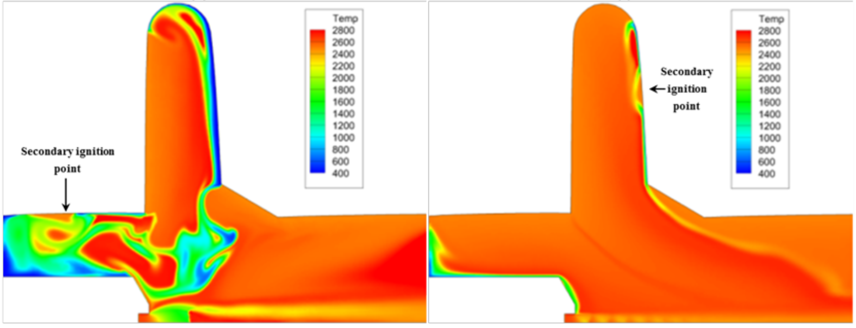

(g) 4.0 ms (h) 13.0 ms

Figure 4.14 Numerical results: FSbI simulation with viscous flow solver

Fig 4.15 compares the jet plume from ignitier at the same time (0.05 ms). The size and position of two results has almost same at a glance. However, detailed features has distinctive difference. Two results piled up in the Fig. 4. 16, from this figure we can see that the inviscid plume is little thicker and lengthy. This differnce causes from the outlet of igniter. At the wall of igniter outlet, N-S analysis decreases the mass flow rate because the boundary is no-slip condition. This decrease the effective area of igniter's outlet then the mass flow decreases in the N-S simulation. Fig 4.17 shows this phenomena clearly. And this phenomena should be a reason which provoke the difference of initial ignition time of Euler and N-S analysis. However, this is not sufficient explanation of initial burning time difference. Therefore, I think more effort should be need to compare the quantity of wall heat transfer.

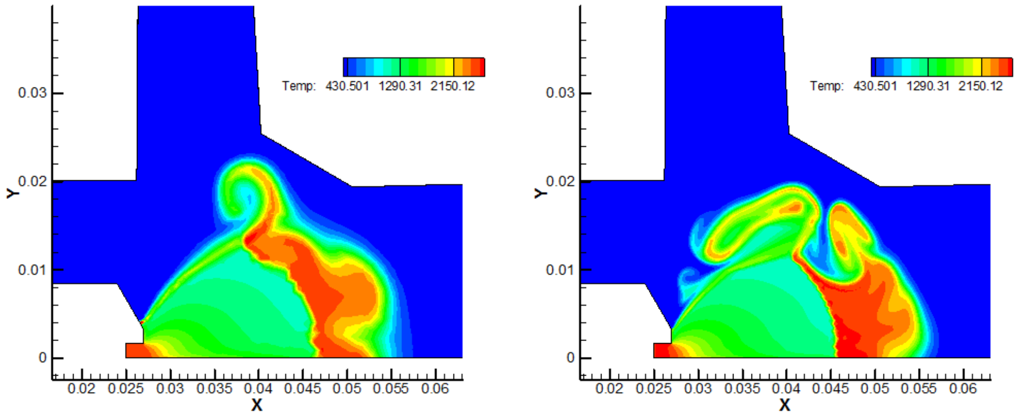

(a) Euler (b) N-S

Figure 4.15 Numerical results: comparison of Euler and N-S result at the 0.05ms

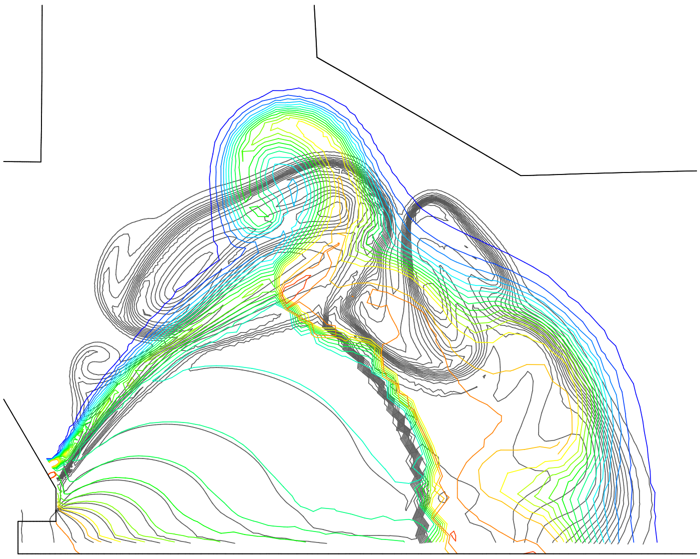

Figure 4.16 Numerical results: jet plume size comparisons

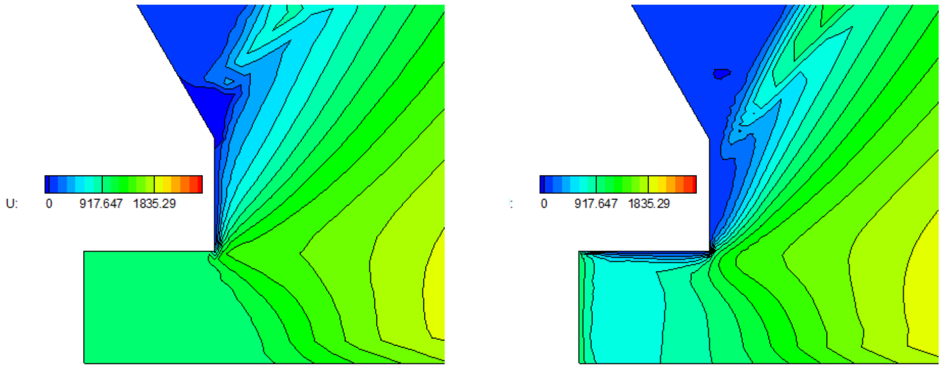

(a) Euler

(b) N-S

Figure 4.17 Numerical results: igniter outlet comparison
at the same time of Euler and N-S result

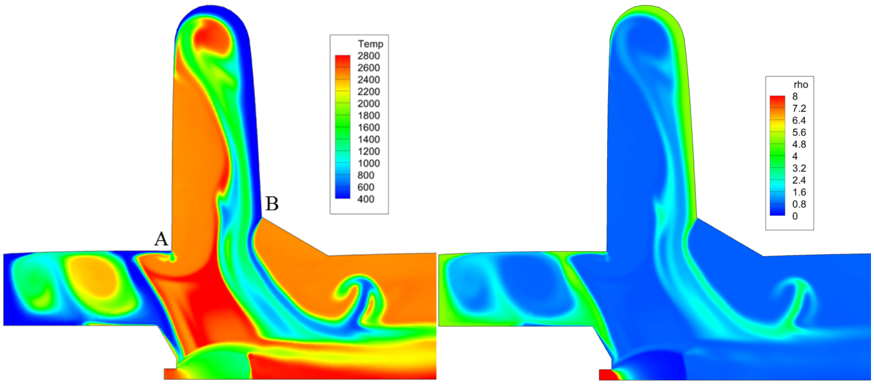

Temperature **Density**

(a) Viscous results at 2.2 ms

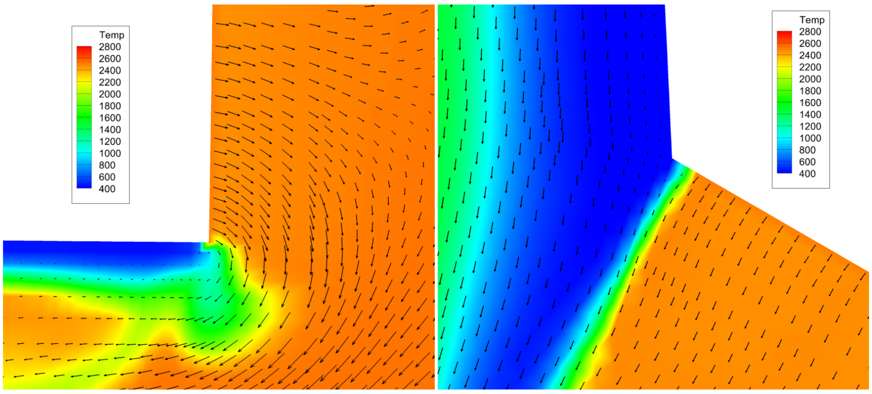

A region **B region**

(b) Viscous results

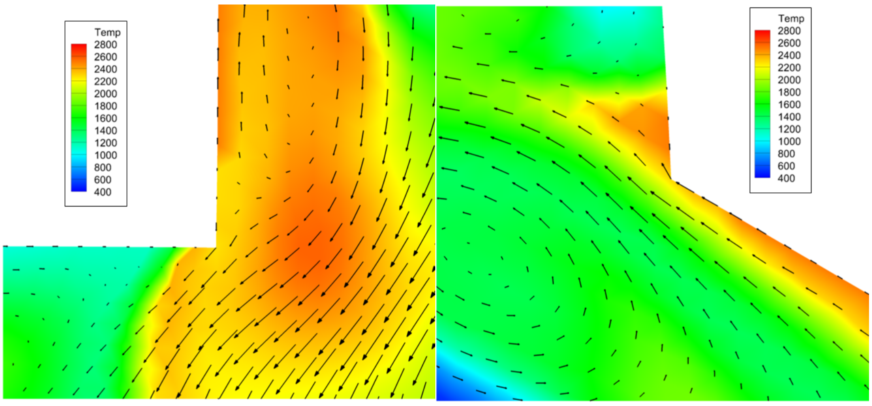

A region **B region**

(c) Inviscid results

Figure 4.18 Numerical results: flame propagation delay around the corners

Figure 4.18 highlights the flame propagation delay around corner. Figure 4.18-(a) is the temperature and density contour of viscous simulation results at 2.2 ms. The delay pattern is particularly observable at the corners A and B with some durability (see Figs. 4.14-(e) ~ (h)). In the inviscid simulation results of Fig. 4.13, the delay pattern at the corners is not observed. Figures 14-(b) and (c) are enlarged views at A and B to compare flow physics obtained by inviscid and viscous simulations. In Figures 14-(b), one side of corner is ignited first and produces high temperature burning gas. The hot gas on the ignited side cannot penetrate into the other side of corner because high density cold gas layers exist on the un-ignited side. In other words, the burning gas from the ignited surface does not have a sufficient velocity and pressure to pass through the cold gas area. In Figure 14-(c), a noteworthy difference is that there is relatively large velocity component around A and B with the tangential direction to the grain surface, pointing toward un-ignited surface. This tangential velocity component helps the high temperature gas enter into the high density cold gas layer easily, and the flame propagation delay is hardly observed in inviscid simulation. Thus, the flame propagation delay around corner comes from the numerical treatment of wall boundary. This suggests that viscous computation is essential to understand the flow physics at the ignition transient phase, because the characteristics of flame spreading along the grain surface are directly related to the internal pressure development at the early phase of rocket operation. At the same time, the other cause of the flame propagation delay is observed which is provided by the physical characteristic of viscous flow.

Figure 4.19 shows the flow field near the boots' entrance. Near the inclined propellant surface, the behavior of the flame propagation delay is observed again. The flame front propagated from the forehead of the grain reaches the corner of the boots' entrance. The geometric shape of the boots' entrance is like a divergent channel and thus the high temperature gas flow is separated near the corner and a separation bubble is formed. The separation bubble mostly contains relatively lower temperature fluids, and flame propagation is delayed on the inclined surface as shown in Figs. 4.19-(a) and (b).

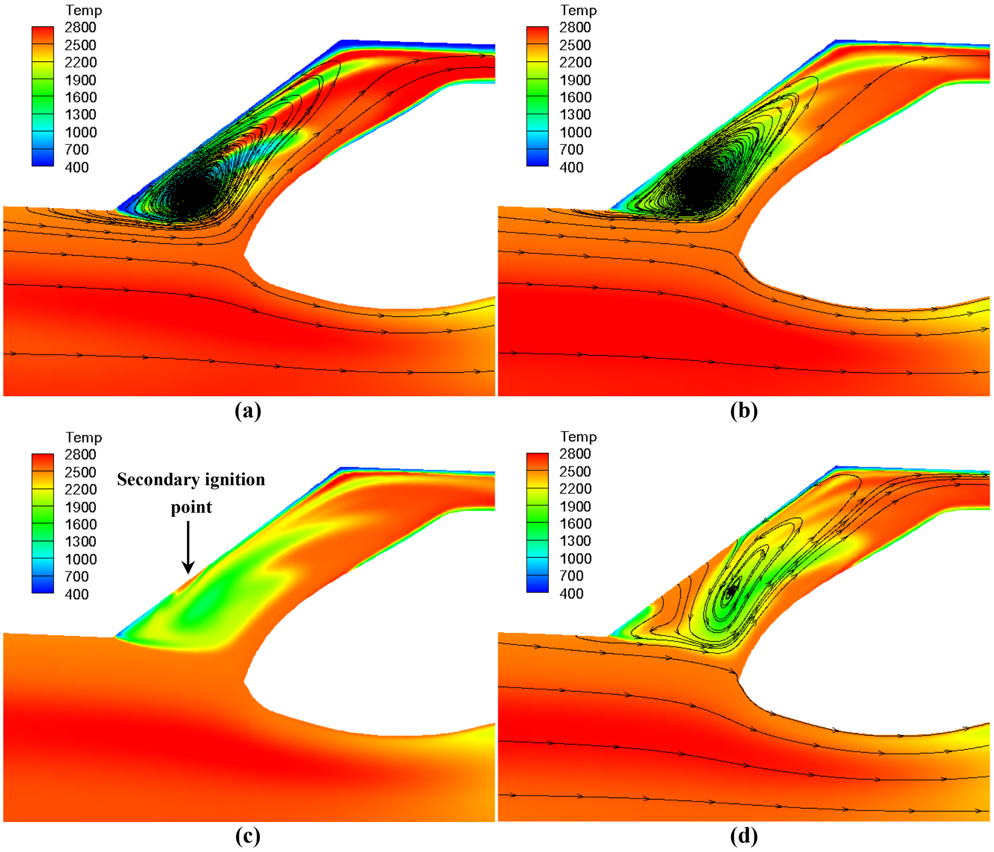

Figure 4.19 Numerical results: flow separation near boots' entrance and secondary burning on inclined grain surface

At the same time, however, the separation bubble also triggers so called the secondary burning [36] to relieve the flame propagation delay. As in Fig. 4.19-(c), the separation bubble induces an isolated-ignited spot on the inclined surface by inhaling high temperature flow from its surroundings. By continuously supplying the hot gas into the inclined grain surface, a point near the middle of the separation bubble is ignited even though the separation bubble mostly contains low temperature fluids. The secondary burning spot grows the burning surface and eventually detaches the separation bubble as in Fig. 4.19-(d). In fact, this secondary burning can also be seen in the slot region. As in Figs. 4.14-(g) and (h), an isolated-ignited spot is observed on the un-ignited face of the congested cold gas layer, but there is some difference between the two cases. The former case (Fig. 4.14) is provoked by a moving rotational flow, while the latter (Fig. 4.18) is due to the heat provided by the stationary rotational flow (separation bubble). Both of the secondary burnings have the common effect of relieving the flame propagation delay.

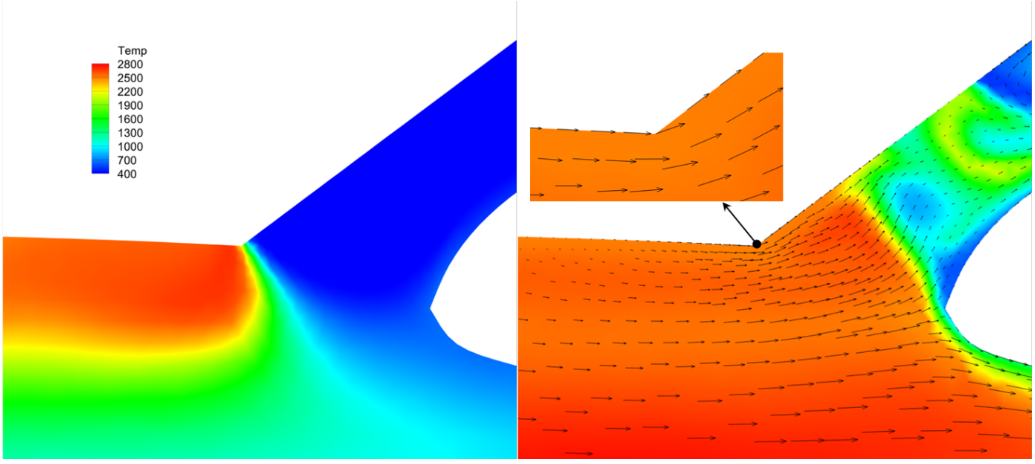

Figure 4.20 Numerical results: flame propagation near the boots' entrance using inviscid flow solver

Figure 4.20 shows the inviscid simulation results near the boots' entrance. In this figure, compared to the viscous results, a totally different physical feature is observed. Basically, inviscid simulation does not capture the flow separation induced by boundary layer. When flame front reaches the corner (Fig. 4.20-(a)), the tangential velocity component makes the high temperature gas smoothly pass the corner without inducing separation bubble (Fig. 4.20-(b)), and thus the flame propagation delay is not observed. As a result, inviscid simulation cannot provide the flame propagation delay and accompanying secondary burning. Compared to the full duration time of rocket motor operation, the flame propagation delay takes place only within a few milliseconds. However, the flame propagation delay may affect the pressure build-up mechanism of the propellant grain and bring a significant change in the ignition transient phase. Furthermore, the flame propagation delay also increases the pressure imbalance on the grain surface which may lead to a fatal structural failure, such as crack propagation. Considering the fact that ignition transient is critical in rocket motor operation and rocket failures may take place in this period, an accurate prediction of flame front spreading along the grain surface is important and the flame propagation delay is closely connected to this problem [3, 38, 39]. In this regard, the flow characteristics provided by inviscid and viscous simulations should be selectively adopted, particularly at the ignition transient phase.

Figure 4.21 shows the density development history at three points inside the combustion chamber. Point A locates on axis, B is on the grain surface in the slot geometry, and C is at the forehead end. As shown in top of Fig. 4.21, B and C point locate in the above- mentioned congested cold gas area. In bottom of Fig. 4.21, point B and C shows a density fluctuation with high peak because of the congested initial cold gas during an ignition phase. However, soon thereafter, these density fluctuations disappear and show stable increase tendency, because the flame spreads all surface of these area. However, Fig 4.22, which is the pressure variation of same place, same time, does not show the distinctive feature of those phenomena (congestion of initial cold gas). Thus, from the perspective of that experimental measurement of density is relatively limited than numerical method, therefore, numerical approach should give more practical information to a researcher for interpreting the physics of combustion chamber.

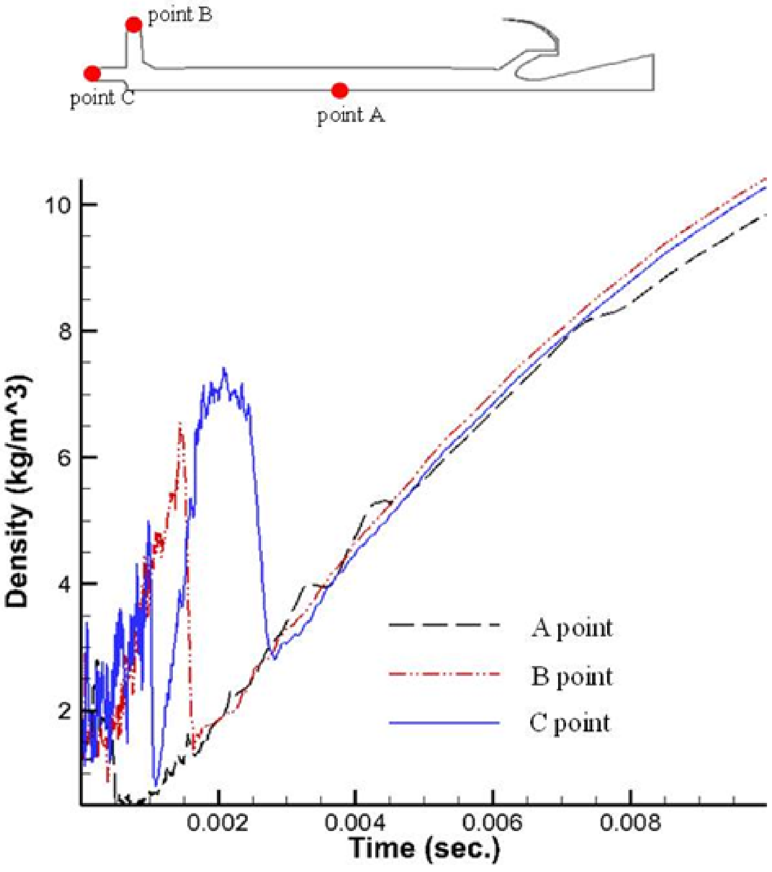

Figure 4.21 Numerical results: locations of measurement & density history in the chamber

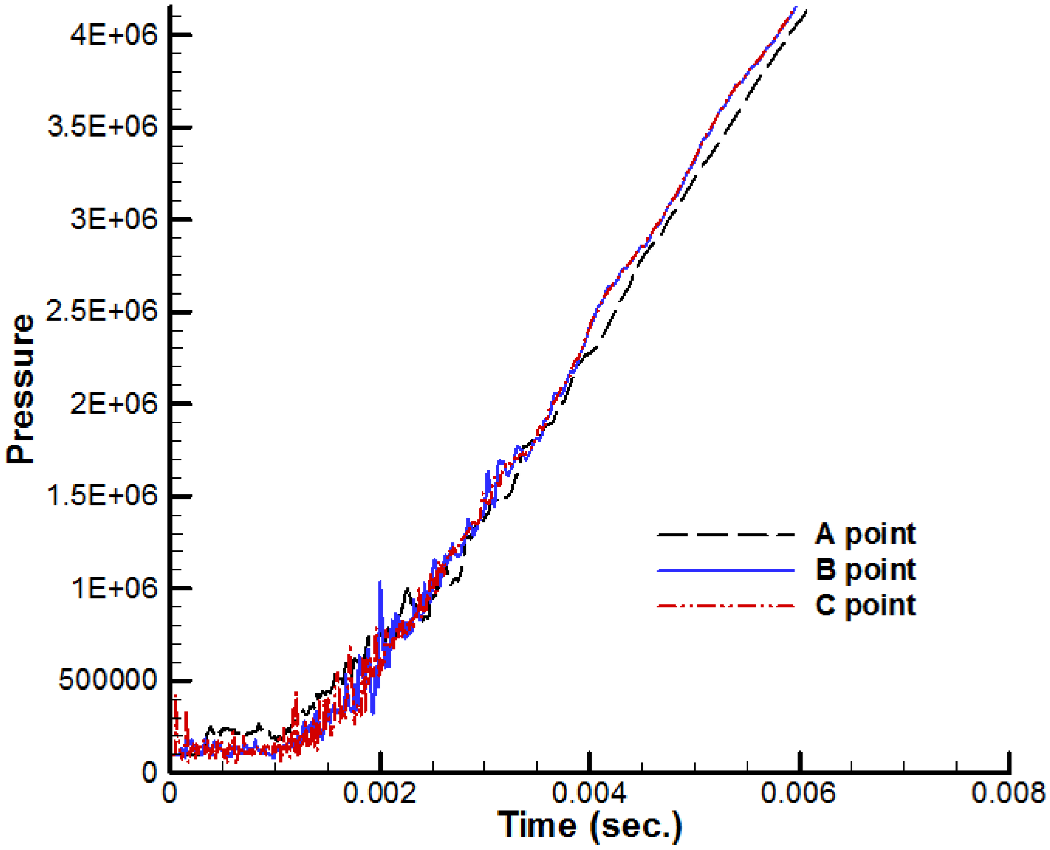

Figure 4.22 Numerical results: FSbI simulation with viscous flow solver

Figure 4.23 shows the pressure development history of three simulation cases at the center of axis during the ignition phase. First case is the FbI (fluid-combustion coupling without solid analysis) simulation, and there is no deformation and volumetric change of the propellant grain. The highest pressure level is maintained until it reaches a steady state. Second case is the FSbI simulation with the inviscid flow solver. Overall pressure level is somewhat lower than the FbI case, and the steady state pressure is approximately 5 % lower than the FbI value. This is because the propellant surface absorbs some portion of pressure energy by deformation, and burning of the propellant grain enlarges the physical domain for fluid analysis. Last case is the FSbI simulation with the viscous flow solver. The simulation result exhibits a similar behavior to the second case except that the pressure build-up is rather delayed during the ignition phase. Accordingly, the time to reach the steady state (or the ignition transient phase) is rather elongated. This is due to the flame propagation delay as mentioned before.

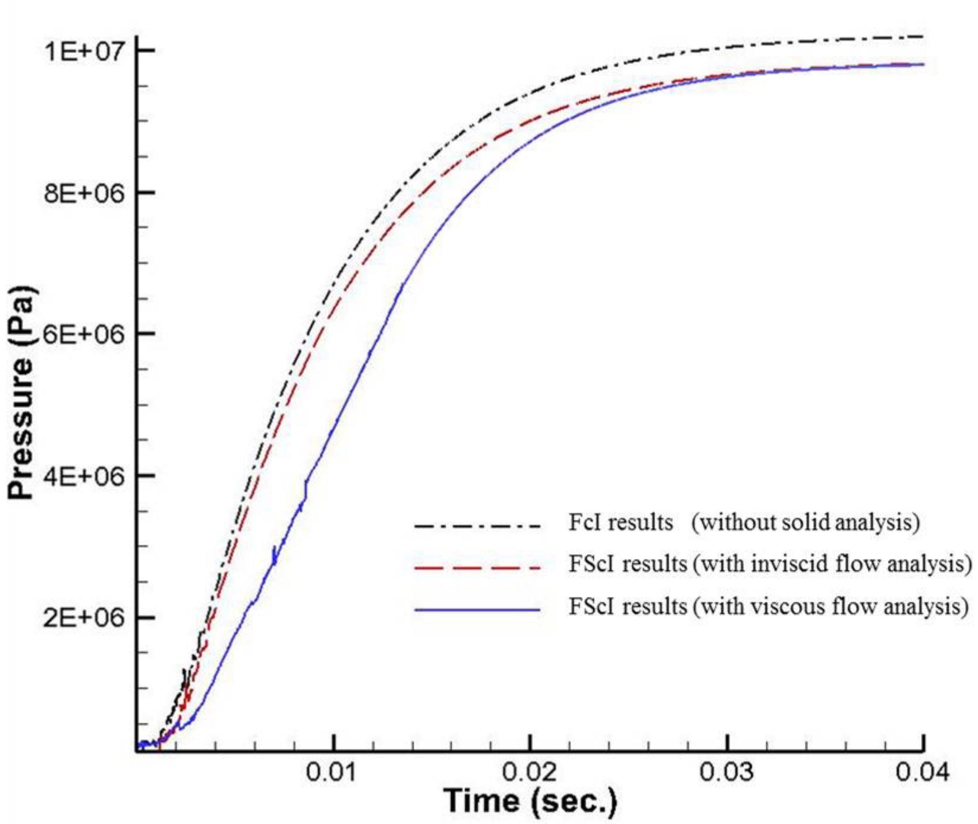

Figure 4.23 Numerical results: pressure development history during the ignition phase

Another cause of the propagation delay can be examined from the view point of the limited numerical modeling. The 1-D based combustion model employed in this research does not take into account the heat conduction along the grain surface. In the inviscid simulation, the hot gas from the ignited surface can be transported into the neighboring un-ignited face. The 1-D combustion model with no slip boundary condition has no way to reflect the heat transfer along the grain surface. This may accentuate a delay of the flame propagation in the viscous simulation. From this perspective, the development of an improved combustion model accounting for the heating effect along the grain surface direction by including the effects of erosive burning and radiation is essential for an accurate integrated simulation. Since experimental data concerning the combustion characteristics of the solid propellant grain is necessary to adjust the propagation speed, this is going to be dealt with as a future research topic.

Figure 4.24 shows the temperature, Mach number and pressure contour of the chamber forehead just prior to the ignition of the propellant surface. The Mach number contour shows that the flow ejected from the igniter is rapidly expanded to generate a supersonic region. The supersonic flow and the geometric constraint of the chamber produce a shock wave, as can be seen in Fig. 24-(a). The temperature field after the shock wave rapidly increases, especially near the trimmed surface, and thus the vicinity of the trimmed surface ignites first. Furthermore, the shock wave and the associated temperature rise accelerate the ignition process by increasing the heat flux transferring to the propellant surface. This indicates that the rapid increase of heat flux caused by shock wave is a major factor in determining the initial burning location when a pyrogen-type igniter is used as a starter. In the solid propellant rocket motor, the initial burning location and time is important to predict its performance and reliability. This is because the ignition delay time is strongly connected with the initial burning characteristics, and many of the unexpected rocket failures take place at the initial ignition phase. Moreover, at the initial ignition phase, the initial burning location induces the pressure imbalance on the grain surface that could trigger a fatal structural deformation [1, 38, 39]. By analyzing the flow physics at the initial ignition phase, better understanding can be obtained on the ignition mechanism of the propellant surface with a pyrogen-type igniter, and the performance and stability of solid rocket motors can be greatly improved.

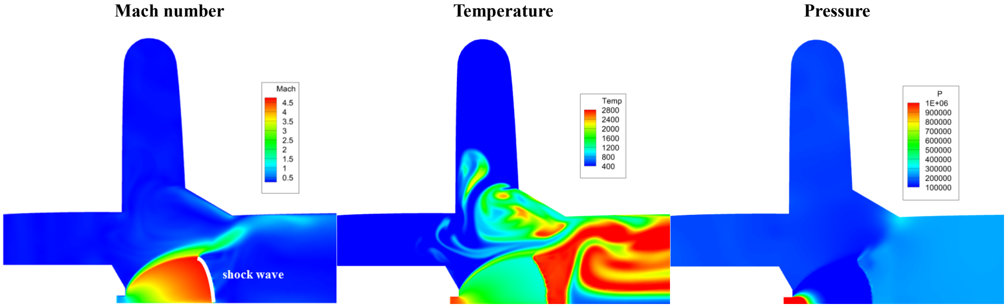

(a) Initial shock shape

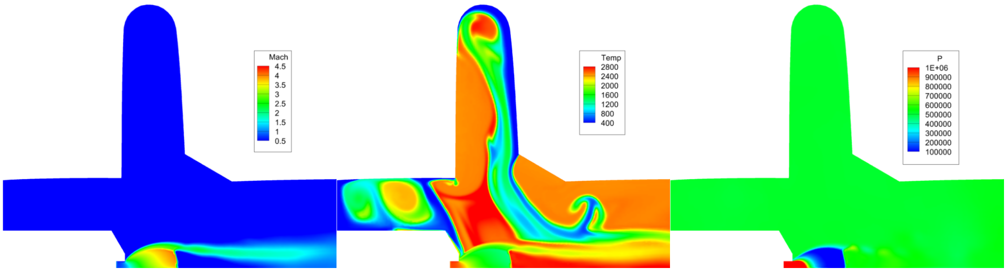

(b) Deformed shock shape

Figure 4.24 Numerical results: Mach number, temperature, and pressure contour at the chamber forehead

Afterwards, the pressure rise in the chamber due to the combustion gas weakens the expansion fan and significantly changes the initial shock shape (the left-hand-side of Figs. 4.24-(a) and (b)). From the center figure of Figs. 4.24-(a), (b), the shock wave and the trimmed grain surface confine the hot gas which is gradually developed into a rotational flow. The rotational hot gas continuously provides heat energy to the propellant surface to induce the flame propagation along the exposed grain surface.

During the flame propagation process, the role of the pyrogen-type igniter tends to gradually diminish. In other words, shortly after the initial combustion gas induces the pressure rise at the chamber forehead, the jet-plume size of the igniter is substantially down-sized, and the strong expansion fan and shock wave change into a typical shock diamonds (Mach disk) as shown in Fig. 4.24-(h). The effect of the igniter in terms of heating the propellant surface becomes negligible, while the rotational hot gas plays an important role.

Figure 4.25 shows the history of the structural displacement of the propellant grain. After ignition, pressure in combustion chamber rapidly increases, and it acts as a mechanical load on the grain surface. The propellant is then temporally deformed by the interaction between pressure load and grain elasticity. In other words, chamber pressure and grain elasticity induce mechanical vibration. The displacement history shown in Fig 4.25 depicts such physical behavior at two locations. Point A is located near the grain surface, and thus directly affected by the unsteady pressure fluctuation and burning of propellant. Point B, on the other hand, is near the rocket case, so it is less sensitive to the perturbation of external force. The elastic result is obtained from the Hyper-elastic model [17], and the visco-elastic result from the generalized Maxwell model [19]. The two results are qualitatively the same, but the quantitative difference confirms the dissipative nature of the visco-elastic material (or the solid propellant grain). The material viscosity absorbs some amount of pressure energy to subdue the dynamic response of grain.

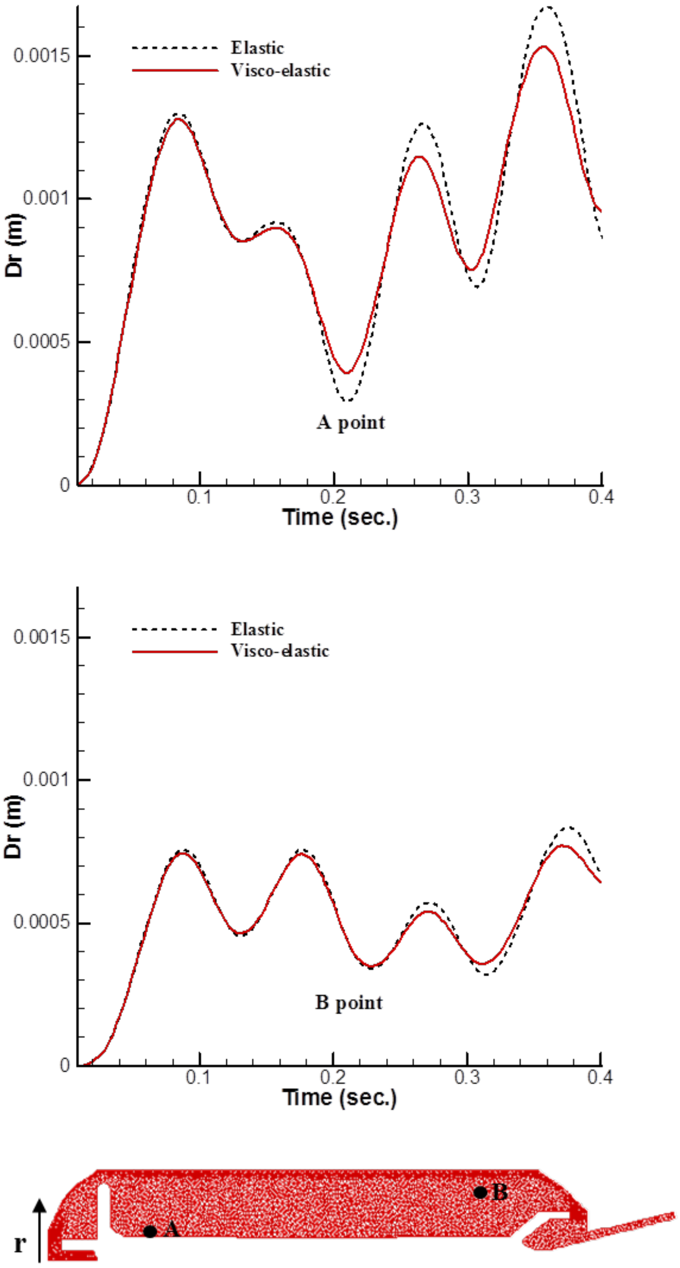

Figure 4.25 Numerical results: history of structural displacement

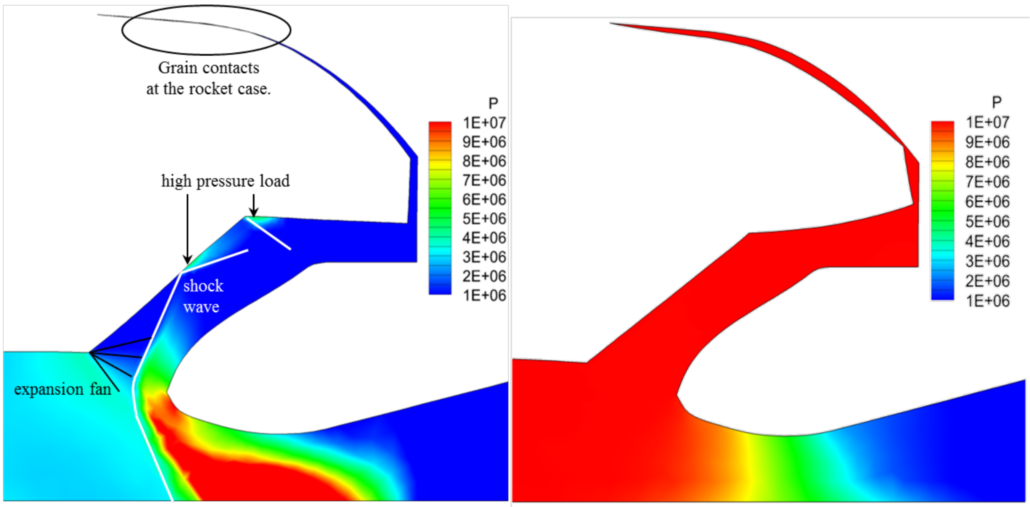

Elastic model **Visco-elastic model**

Figure 4.26 Numerical results: the boots' contact problem

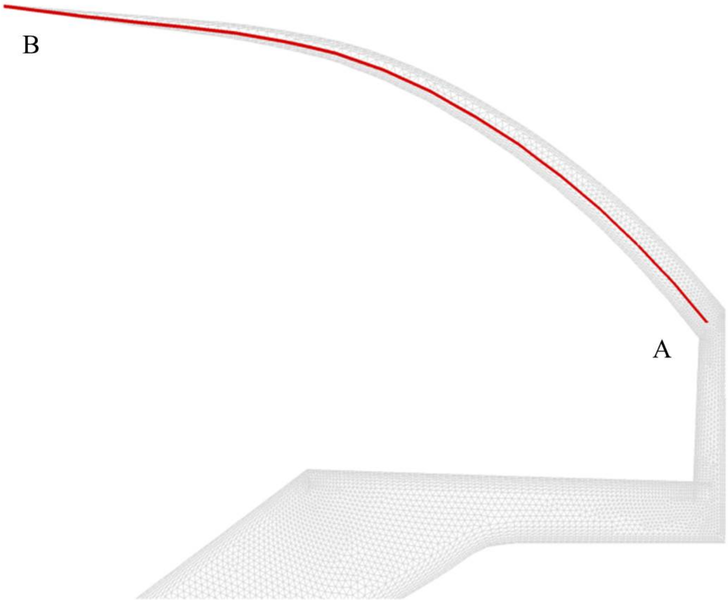

Figure 4.27 Virtual contact line

Besides the surface ignition process, another physically important phenomenon caused by the fluid-structure coupling is the boots' behavior in the transient burning phase. As shown in Fig. 4.26, most solid rocket motors have a narrow crevice called the boots gap between the propellant grain and the rocket case (or the region from point A to point B in Fig. 4.27). The role of the boots gap is known to prevent an unexpected structural failure due to severe thermal deformation. Thus, the unsteady behavior of the boots gap must be included in the FSbI simulation. The hot gas created by the propellant burning rapidly propagates to the rocket nozzle area. The gas flow passing the boots entrance produces a series of expansion fan and shock wave due to geometric constraint (see the left picture of Fig. 4.26). In particular, the shock impingement and reflection act as a strong pressure load on the grain surface, and the propellant grain is pushed toward the vertical direction. As a result, the boots gap becomes progressively narrower to lead a structural contact problem. The boots contact problem is physically quite reasonable, but it imposes a numerically challenging situation. Under the boots contact situation, the mesh size in fluid domain is infinitesimally small and the time step size becomes practically zero. The right-hand-side of Fig. 4.26 shows the result obtained by the visco-elastic material model, indicating that the structural deformation is concentrated on the boots head to create a contact problem.

In order to prevent the contact situation while maintaining the boots effect, a technique based on a virtual contact line is introduced. The basic idea is quite simple in a sense that the boots gap is required to maintain a minimal distance to make fluid analysis possible. We set a virtual boundary line as shown in Fig. 4.27, across which the grain movement is prohibited. In other words, if the grain surface touches the line, it is regarded as the contact condition and further movement across the line is prohibited. The propellant surface is then pushed back by a sufficiently high-pressure load from the boots gap inside. The virtual contact condition is then negated, and the grain is allowed to move normally. Figure 28 compares the displacement contour of the propellant grain without/with imposing the virtual contact situation. The highly concentrated unphysical deformation caused by the boots contact is clearly relieved and improved by introducing the virtual contact line. This indicates that the transient burning process for the propellant grain with the boots can be successively simulated by suitably imposing a virtual contact distance. According to the simulation results with the virtual contact line method, the propellant grain near the boots is pushed to the upward direction and touches the virtual contact line, and the grain movement is restricted by the virtual contact condition. Quickly afterwards, the contact condition is released by the pressure load from the boots gap inside, and the grain moves back to the downward direction. The pressure in the boots gap drops due to the volumetric change, and the grain moves again toward the upper direction. This mechanical vibration of the grain is sustained for a short time until the chamber pressure approaches a quasi-steady state.

Figure 4.29 shows the pressure history at the center of combustion chamber during the full-burning simulation. The chamber pressure increases instantly and reaches the maximum point, while the nozzle membrane, that is designed to contain the hot gas until the chamber pressure reaches a specific value, is finally broken, and the contained flow is spouted out through the nozzle. As a result, the pressure rise in the combustion chamber slows down and approaches a steady state by balancing the incoming mass flow from the burned grain and the outgoing mass flow through the nozzle. Afterwards, the internal gas pressure is maintained without any noticeable changes. During this period, the burning surface grows according to the burnback progress, and the volumetric expansion of fluid domain is accompanied. Each of the two is the main cause of rising and falling the chamber pressure. If the chamber pressure rises, the burning rate grows and the volumetric expansion rate of fluid domain increases, which should act as a counterbalance to decrease the chamber pressure. Finally, the small segment of the propellant grain is fully burned away, and the mass flux decreases accordingly. This phase is called a steady state. In the steady state, the burnback velocity of the propellant grain is nearly constant since the burning rate is decided by the fluid pressure via the pyrolysis law. As shown in Fig. 4.30, most of the combustion chamber has nearly constant temperature and pressure, and local change can be observed near the rocket forehead, the boots gap and the nozzle.

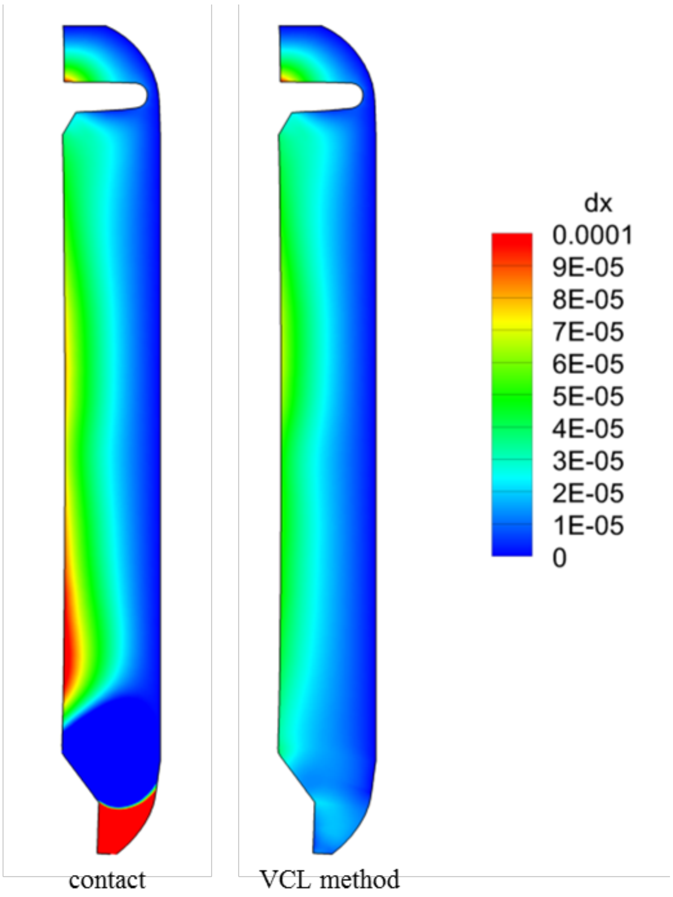

Figure 4.28 Numerical results: structural deformation contour of propellant grain without/with virtual contact line method

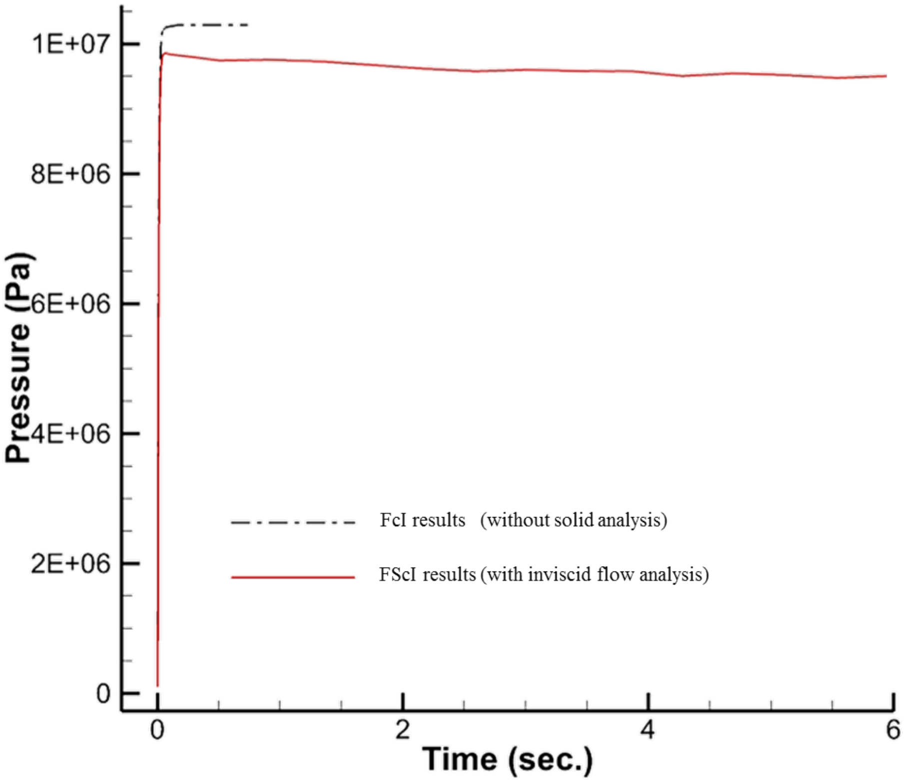

Figure 4.29 Numerical results: pressure history in the chamber during the FSbI simulation

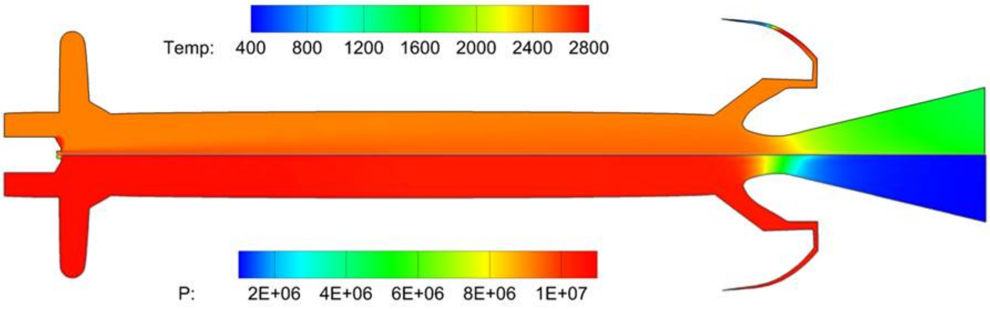

Figure 4.30 Numerical results: steady-state flow variable contours in the combustion chamber

During the combustion process, the propellant grain is burned away and deformed due to the burning mechanism and the structural load from the high-pressure gas in the combustion chamber. Figure 4.31 shows the progressive geometric change of the solid propellant grain during the full-burning rocket simulation. It is seen that the burning characteristic around convex and concave corner is different. The convex corner maintains its initial shape but concave corner becomes gradually round. Particularly, the shape change near the trimmed surface is noticeable, which is consistent with the previous research [32]. Figure 4.31 also compares the change of fluid domain at several burning stages. The initial solid propellant grain is topologically separated into two sub-grains. At the final burning stage, one of them is fully burned away and the other remains a little. From Fig. 4.31, the highly unsteady nature of the initial burning is clearly contrasted with the stable characteristic of the quasi steady state burning.

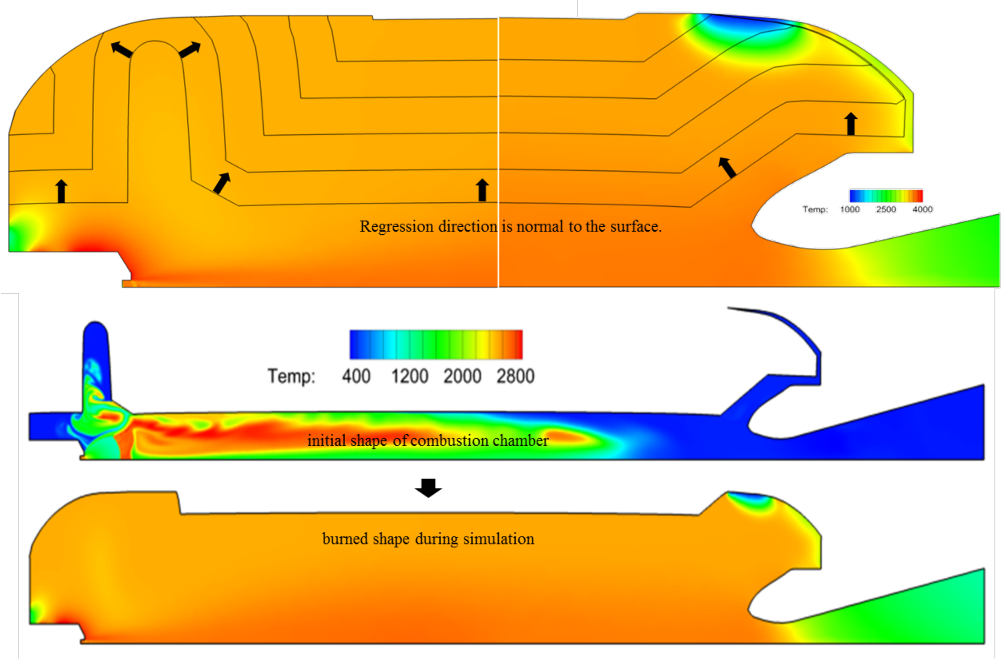

Figure 4.31 Numerical results: geometric changes process of propellant grain and fluidic domain

Chapter V

CONCLUDING REMARKS & FUTURE WORKS

5.1 Concluding Remarks

An integrated fluid-structure-combustion simulation to understand the multi-scale, multi-physics phenomena of solid rocket motor interior has been presented. To capture the progressive burning boundary of a propellant grain, the ALE kinematical description has been implemented into the fluid/solid formulation. Two-dimensional axisymmetric compressible flow is assumed for the combustion chamber flow, and the mechanical response of grain is obtained using the non-linear elastic/visco-elastic constitutive model. A 1-D transient burning model is adopted to efficiently simulate the burning process of an interface between fluid domain and grain surface. To account for the deformation and burning process of the propellant grain, an efficient mesh repair/regeneration algorithm and a regression model are implemented. Using the integrated program, the fluid-structure-combustion coupling is simulated during the burning process in the solid rocket combustion chamber. From the simulation results, we could observe the detailed flow physics of the initial burning and the flame propagation characteristics of the exposed grain surface, and investigate the ignition mechanism due to shock wave and expansion fan. Furthermore, we could understand the behavior of the structural deformation of the propellant grain. By examining inviscid and viscous flow simulation results, we also understand the flame propagation delay and the secondary burning effect by rotational flows. In addition, the virtual contact line is successfully introduced to prevent the boots' contact problem without compromising its effect.

Finally, I have conducted an integrated full-burning simulation of a solid rocket motor using the developed analysis program. While existing experimental tests can provide some limited data, various information regarding flow variables in the combustion chamber as well as solid variables of the propellant grain could be obtained.

5.2 Future work

To more accurate and robust 2-D integrated simulation, firstly, the in-depth investigation to the differences of ignition time between Euler and N-S simulation should be conducted. And the virtual contact method should be needed to be refined for realistic simulation. In this stage, there are lots of geometric limitations to apply contact line. However, if fluid solver could simulate in the zero cell area situation, the fields of application could be enlarged.

At the same time, there are several items to be improved for more accurate and reliable simulations and three-dimensional extension. These include adapting the advanced burning model which could consider erosive burning effect of propellant grain. Moreover, a heterogeneous characteristic should be included to the burning model to achieve more realistic simulation of combustion chamber, because most solid propellants used today are composite propellants (which have heterogeneous properties) and non-uniform temperature distribution of and alumina particle behavior of composite propellant did important role for solid rocket performance. And I should have a more effort for an elaboration of structural modeling to capture compressible effect caused by deformation of thin rocket case because it could differs the displacement tendency of solid propellant deformation significantly and not be ignored to more accurate prediction of real rocket performance.

Chapter V

Appendix

A1. Common refinement data transfer scheme for 3-D rocket

Among the data transfer methods, the common-refinement method (C-R method) has distinctive two characteristics as follows: constructing a common surface and numerical integration with minimizing a certain error norm. The common surface is constructed between non-matching meshes by referring geometry features of two computational meshes simultaneously. On the common surface, data interpolation is performed using minimizing certain error norm. Therefore, the C-R method is known to yield conservative and accurate data transfer for non-matching interface cases.

Figure A.1 shows the general procedure of C-R method which developed to use data transfer tools for 2D/3D shape of combustion chambers inside solid propellant rockets. The C-R procedure is consisted with two main categories; making common surfaces and data interpolation.

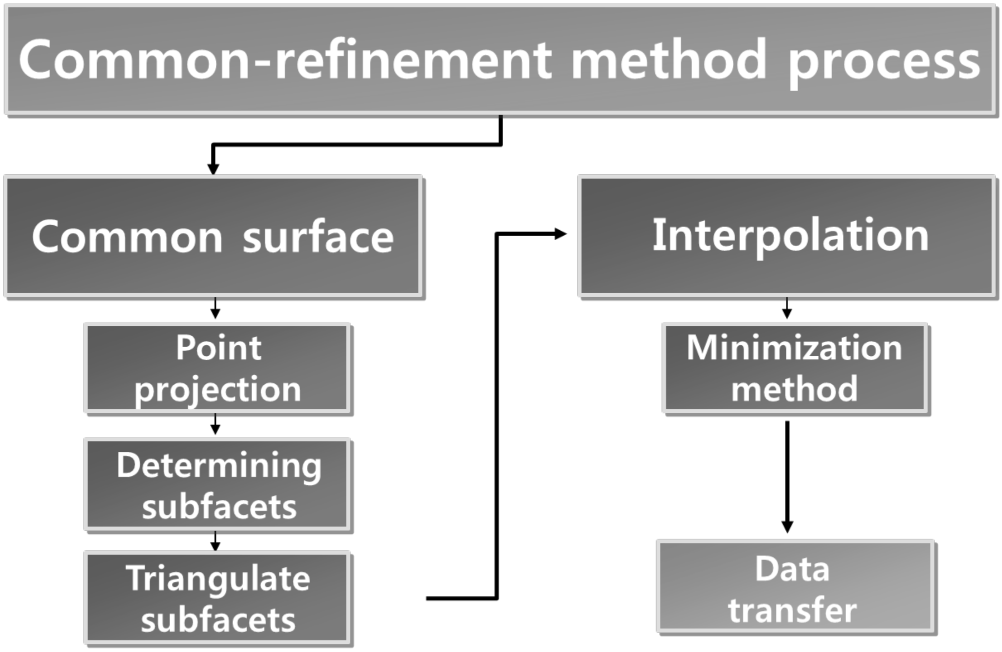

Figure A.1 General procedure of common-refinement method

A1.1 Mesh points projection

To construct a common surface, the source and target mesh nodes need to be projected to opposite mesh surfaces. Nodes project direction can be defined by averaging normal vectors of element surfaces which include a projecting node. Exact location of nodes projection has to be set as intersection points between mesh surfaces and project direction vectors.

The Common surface is consisted of common nodes which are made from linear interpolation process of projected nodes.

$$\alpha S+\beta T\equiv\left\{x=\alpha S+\beta T(s)\ \middle|\ s\in S\right\},(\alpha+\beta=1) \tag{A.1}$$

For (Eqn. A.1), α and β are positive constants and have condition of $\alpha+\beta=1$.

Fig. A.2 shows that subfacets on a common surface could have various polygon shapes for the case of structured quadrilateral (structure part) and unstructured triangular (fluid part) meshes combination.

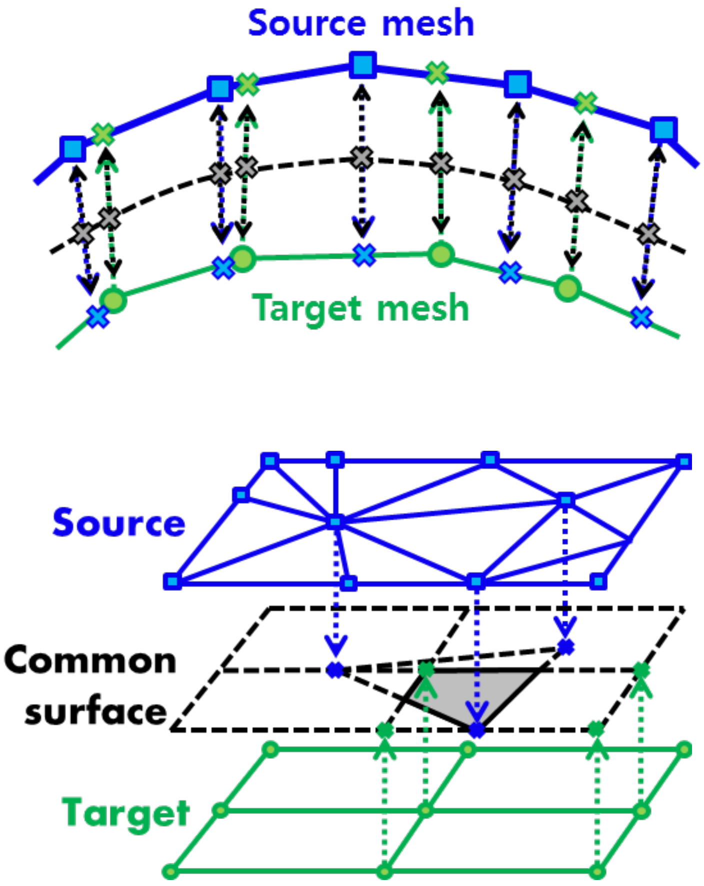

Figure A.2 Subfacets on a common surface

A1.2 Subfacets construction

Subfacets on a common surface are organized by linking common nodes with geometry information of source and target meshes. Common nodes which projected from each meshes to the common surface construct quadrilateral and triangular meshes.

After determining background elements overlapped to a standard element, intersection points of the background elements and the standard element segments are added as common nodes.

This process must be performed for all source mesh elements to construct common surface subfacets. Fig. A.3 shows the constructing subfacets process especially for the case of one triangular standard element has four quadrilateral background elements. Finding intersection points starts in a standard element node (a blue circle in Figure) and proceeds with direction of an arrow in Fig. A.3.

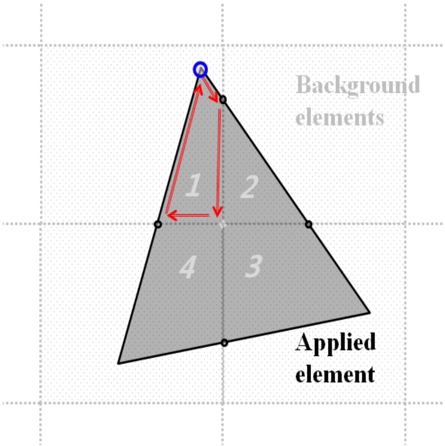

Figure A.3 Constructing subfacets process

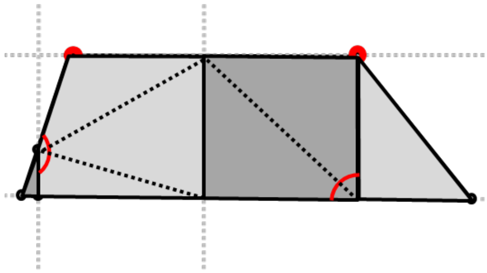

Figure A.4 Subfacet triangulation process

A1.3 Subfacets triangulation

In case of non-matching interfaces between quadrilateral and triangular meshes, subfacets may have various polygon shapes. Therefore, it is difficult to generalize of shape function which is used in data interpolation process with numerical integration. Triangulation of subfacets can be an efficient solution for data interpolation. By triangulation process, we obtained only one kind of shape function (triangular shape function). As a result of this process, data transfer process could be performed more effectively.

A1.4 Data interpolation methods

A1.4.1 L2 minimization

L2 minimization method minimize L2 norm of transferred data differences.

$$\frac{\partial \int_{\Omega} (g-f)^2 dx}{\partial g_i} = 0$$

$$\frac{\partial \int_{\Omega} (g-f)^2 dx}{\partial g_i} = 2\sum_{j=1}^{n} \int_{\Omega} \psi_i \psi_j dx g_i - 2\int_{\Omega} \psi_i f dx \qquad \text{(A.2)}$$

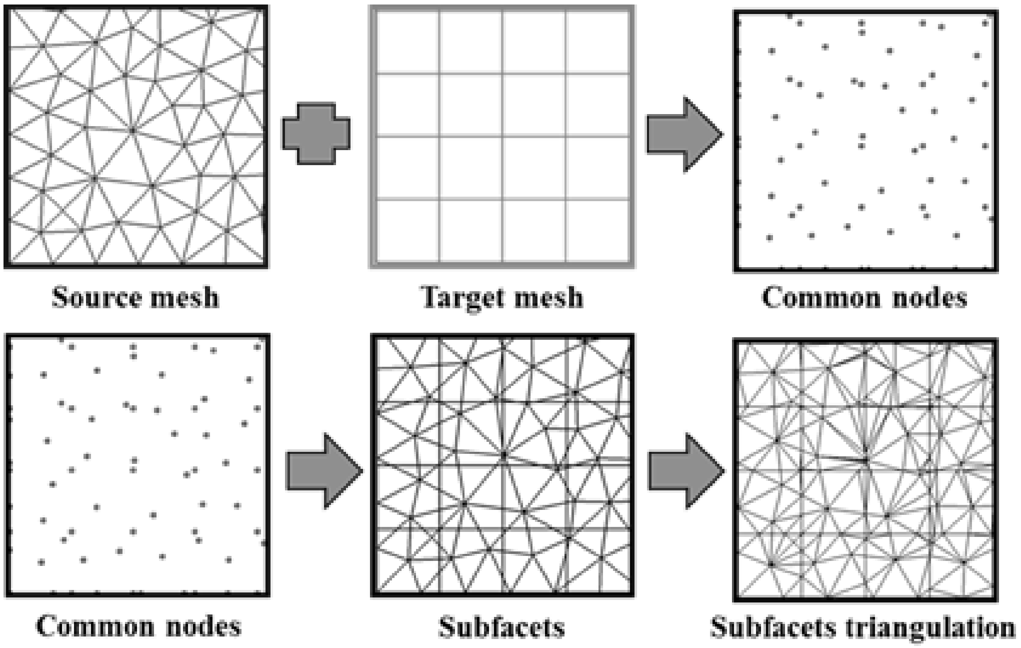

Figure A.5 Example of making common-refinement surface

In formula (A.2), ψ represents shape functions of target mesh nodes, g and f are quantities of transferred data and source data. We defined $M = \int \psi_i \psi_j dx$, $b = \int_\Omega \psi_i f dx$, $x = g_i$ so that (Eqn. A.2) could be expressed as a matrix equation $Mx = b$.

A1.4.2 Sobolev minimization

Gibb’s phenomena occur when transferring discontinuous data with L2 minimization. This problem causes inaccuracy of data transfer, especially in solid propellant rocket combustion chambers where internal flow generated strong shock waves frequently. To decrease numerical vibration, we examined data interpolations by minimizing first order sobolev norms.

$$\begin{aligned} &\frac{\partial \int_{\Omega} ((g-f)^2 + \alpha(g^{'} - f^{'}))dx}{\partial g_i} \\ &= 2\sum_{j=1}^{n} g_i \int_{\Omega} (\psi_i \psi_j + \alpha \psi_i^{'} \psi_j^{'})dx - 2\int_{\Omega} (\psi_i f + \alpha \psi_i^{'} f)dx \end{aligned} \tag{A.3}$$

A1.5 Validation of common refinement

Developed data transferred module is validated with Jiao and Heath’s results as shown in figure A.6~7. Fig. A.7 indicates the comparison of relative errors after 2^9 repeated data transfer computation and Fig. A.7 is a contour of the peaks function after 2^5 iterations. Based on these results, we confirmed that C-R method adaptation had been performed with proper validity and reliability.

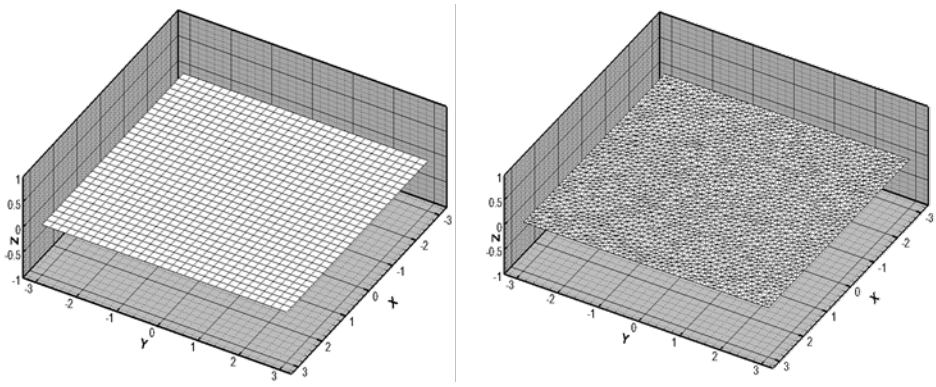

Figure A.6 Mesh condition for validation case

(left) source mesh, (right) target mesh

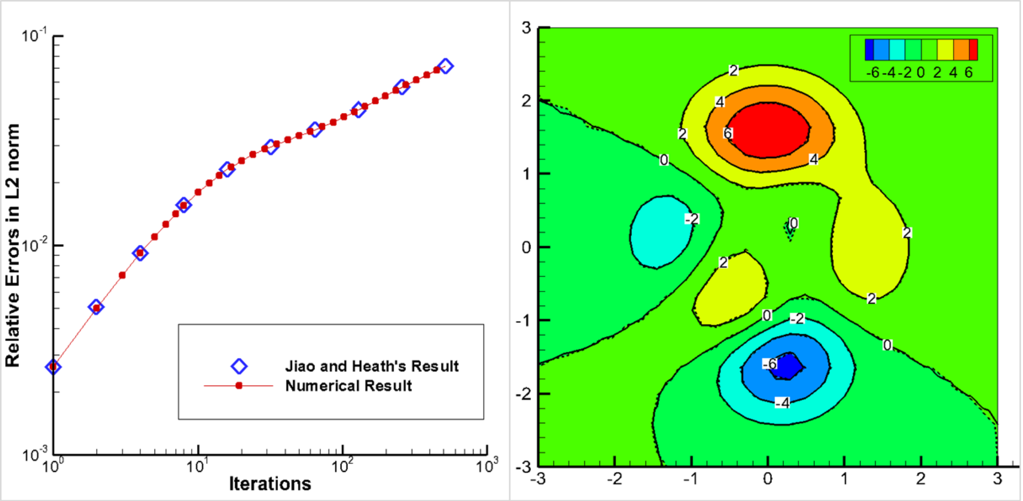

Figure A.7 Comparison of relative errors (left), Contour of peak function after repetitive data transfer (right, solid : exact solution , dashed : numerical result)

A1.5 Discontinuous function transfer between flat surfaces

We tested discontinuous data transfer between two flat surfaces. From this test, we could confirm that the conservative error of C-R method had been maintained while other methods derived non-conservative result (Fig.A.8). For the reason of conservation of C-R method is that interpolation process uses data integration on a common surface. The conservative feature of C-R method is effective especially in repeat data transfer computations. However, from Fig.A.9, C-R method had inaccurate result in relative error compared with other methods.

Consistent interpolation	**Thin plate splines**	**Multiquadric-biharmonic**	**Common-refinement**
1	9.74	10.68	16.34

Table A.1 comparison of relative time cost

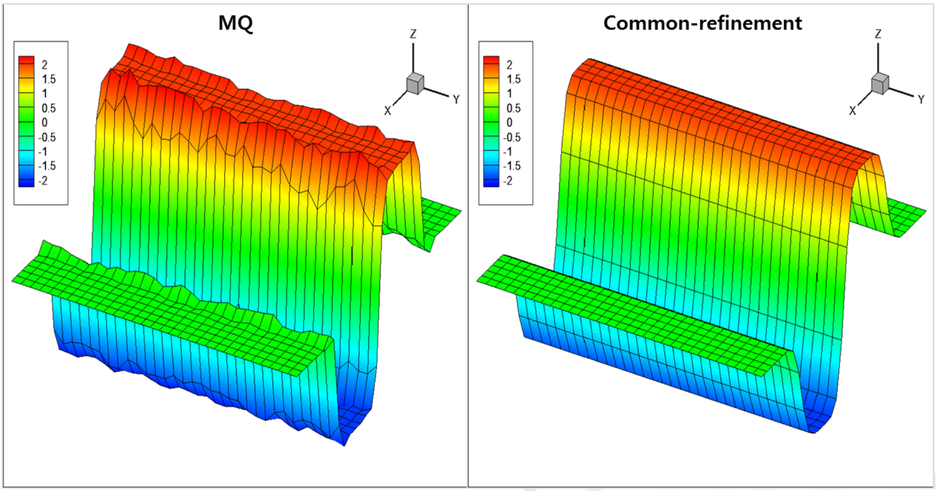

Figure A.8 Data transfer results

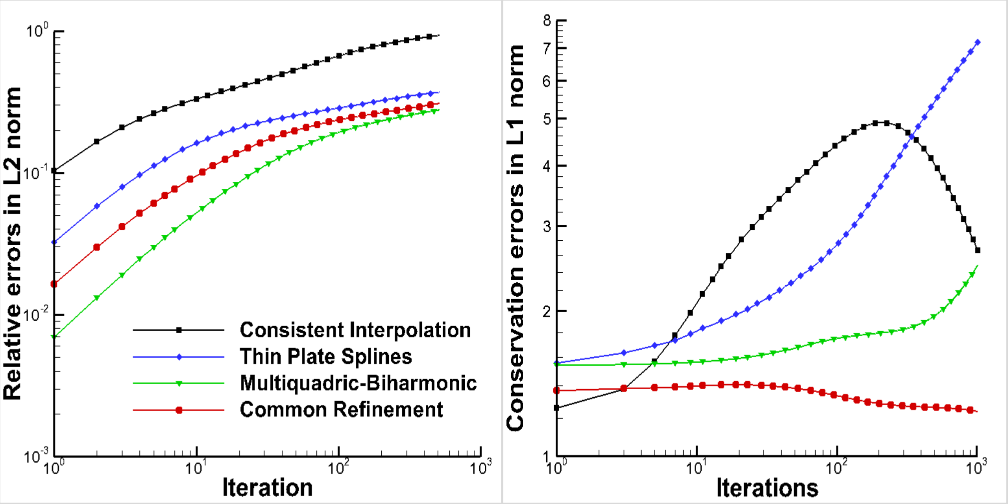

Figure A.9 Comparison of relative errors (left),

Comparison of conservation errors (right)

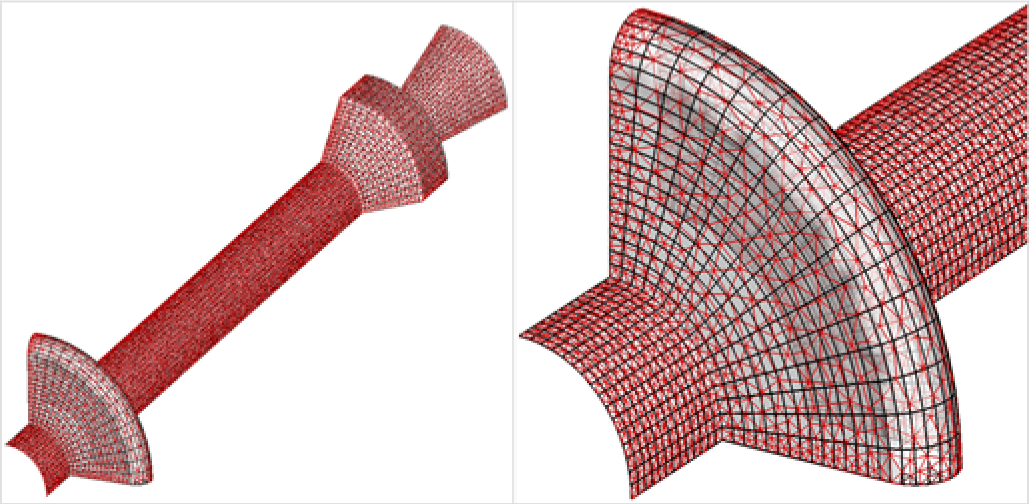

Figure A.10 Non-matching geometry of solid propellant rocket interior combustion chamber shape and examined discontinuous data transfer computations. The test shape is composited with flat and curved surface complicatedly. Furthermore, there are sharp edges which changes shape drastically so that robust construction of a common surface was essential. Structured quadrilateral mesh (327×17 nodes) and unstructured triangular mesh (392×20 nodes) are used as test meshes (Fig.A.10).

In conclusion, we could determine that C-R method was an outstanding method for repeated data transfer computations in complicated three dimensional shapes based on test results. Fig.A.11 indicates relative and conservative error after 2^9 iterations. C-R method outperformed other methods in a respect of both accuracy and conservation. TPS and MQ method generated numerical vibration from the beginning of iterations so that it could not satisfied accuracy and conservation. Comparing to consistent interpolation method, the C-R method produced more accurate and conservative results by accumulating relative error less. Fig.A.13 shows a comparison of L2 & Sobolev minimization test result in a transformed coordinate. The result of this test, we could confirm that Sobolev minimization suppressed numerical vibration efficiently.

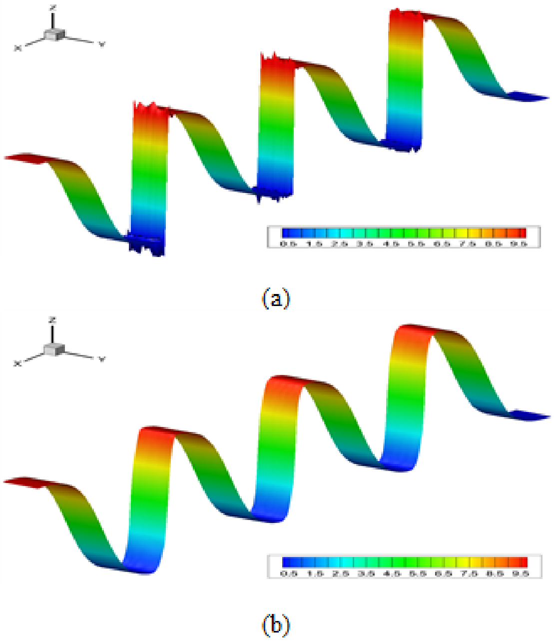

Figure A.11 Comparison of L2 & Sobolev minimization test
(a)L2 minimization (b) Sobolev minimization

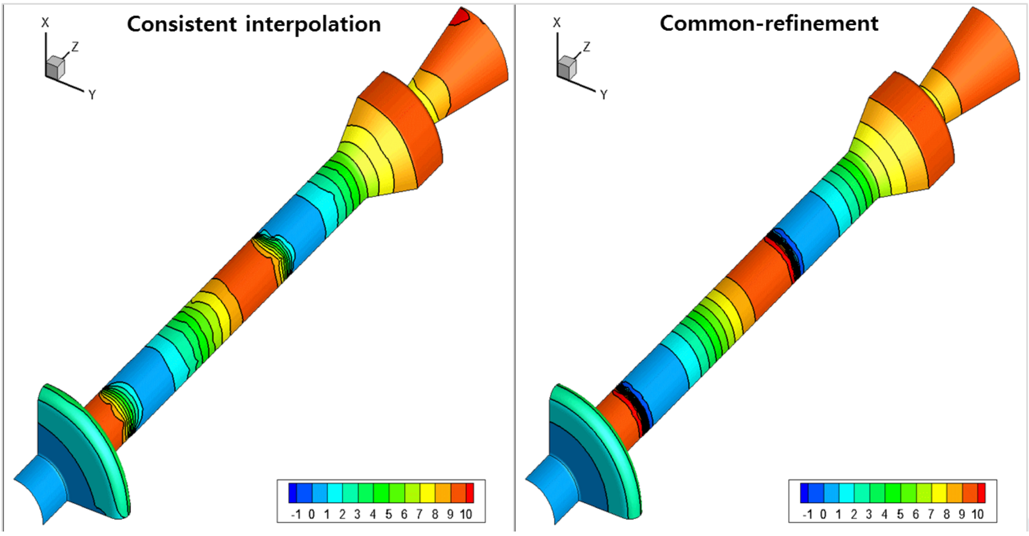

Figure A.12 Data transfer result

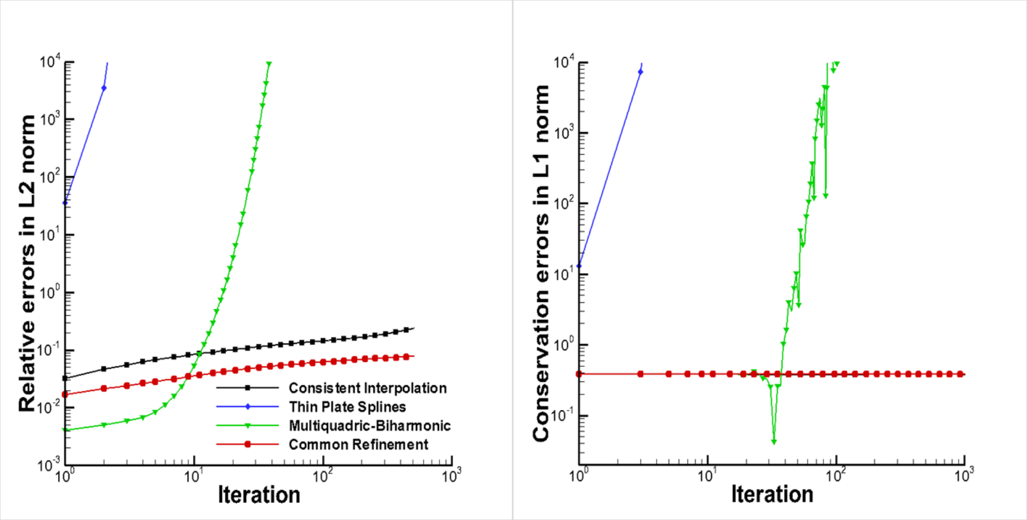

Figure A.13 Comparison of relative errors (left),

Comparison of conservation errors (right)

References

[1] Johnston, W. A., and Murdock, J. W., “Flow-Structural Interaction Inside a Solid Rocket Motor during Ignition Transient,” Journal of Propulsion and Power, Vol. 11, No. 5, 1995, pp. 998–1005.

[2] Willcox, M. A., Brewster, M. Q., Tang, K. C., Stewart, D. S., and Kuznetsov, I., “Solid Rocket Motor Internal Ballistics Simulation Using Three-Dimensional Grain Burnback,” Journal of Propulsion and Power, Vol. 23, No. 3, May-june 2007, pp. 575–584.

[3] Chang, I.-S., Patel, N. R., and Yang, S., “Titan IV Motor Failure and Redesign Analyses,” Journal of Spacecraft and Rockets, Vol. 32, No. 4, 1995, pp. 612 – 618.

[4] R. Fiedler, X. Jiao, A. Namazifard, A. Haselbacher, F. Najjar, I. Parsons, “Coupled fluid-structure 3-D solid rocket motor simulations,” AIAA Paper 2001-3954, July 2001.

[5] Kuo, K. K., and Zhang, B., “Transient Burning Characteristics of JA2 Propellant Using Experimentally Determined Zel’dovich Map,” Journal of Propulsion and Power, Vol. 22, No. 2, 2006, pp. 455–461.

[6] Zilberman, S., Albagli, D., and Katzir, A., “Experimental Characterization of Transient Burning Properties of RDX–XLDB Propellant,” Journal of Propulsion and Power, Vol. 29, No. 2, March–April 2013, pp. 306-312.

[7] Atwood, K. P. Ford, and Wheeler C. J., “High-Pressure Burning Rate Studies of Solid Rocket Propellants,” Progress in Propulsion Physics, Vol. 4, 2013, pp. 3-14.

[8] Victor, D. T., Zhang, j., Jackson, T. L., and Amir, H. G. Isfahani, “Numerical Study of Erosive Burning in Multidimensional Solid Propellant Modeling,” Journal of Propulsion and Power, Vol. 27, No. 4, July–August 2011, pp. 811-821.

[9] Hong J. S., Moon H.,-J., Sung H.-G., “Numerical Study on Vortex Driven Pressure Oscillation in a Solid Rocket Motor with Two Inhibitors,” AIAA Paper 2013-0568, Jan. 2013.

[10] Han, S., Choi, H., Kim, C., Hwang, C., Jung, G. and Oh, J., “ALE-Based FSI Simulation of Solid Propellant Rocket Interior,” AIAA Paper 2010-0052, Jan. 2010.

[11] Han, S., and Kim, C., “A full burning FSI simulation of solid propellant rocket interior,” AIAA Paper 2012-0038, Jan. 2012.

[12] Hirt, C. W., Amsden, A. A. and Cook, J. L., “An arbitrary Lagrangian-Eulerian method for all flow speeds,” J. Comput. Phys., Vol. 14, 1974, pp.227–253. Reprinted in J. Comput. Phys, Vol. 135, 1997, pp. 203–216.

[13] Donea, J., “Arbitrary Lagrangian-Eulerian finite element methods,” In Computational Methods for Transient Analysis, edited by Belytschko T and Hughes TJR ., North-Holland: Amsterdam, 1983, pp. 474–516.

[14] Hwang, C., Massa, R., Fiedler R., and Geubelle, P. H., “Simulation of convective burning and dynamic fracture in solid propellants,” AIAA Paper 2002-4342, July 2002.

[15] Kim, K. H., Kim, C., Rho, O.-H., “Methods for Accurate Computations of Hypersonic flows, PART Ⅰ: AUSMPW+ scheme,” J. Comput. Phys., Vol. 178, 2001, pp.38–80.

[16] Venkatakrishanan, V., "Convergence to steady state solutions of the Euler equations on unstructured grids with Limiters," J. Comput. Phys., Vol. 118, 1995, pp.120–130.

[17] Haselbacher, A., McGuirk, J. J., and Page, G. J., "Finite Volume Discretization Aspects for Viscous Flows on Mixed Unstructured Grids," AIAA Journal, Vol. 37, No. 2, Feb. 1999, pp. 177 – 184.

[18] Arruda, E. M., and Boyce, M. C., "A Three dimensional constitutive model for the large stretch behavior of rubber elastic material," Journal of the Mechanics and Physics of Solids, Vol. 41, No. 2, 1993, 1993, pp. 389–412.

[19] Geubelle, P. H., Hwang, C., Fiedler R., Breitenfeld, M. S., and Haselbacher, A., "Simulation of Dynamic Fracture Events in Solid Propellant Rockets," AIAA Paper 2001-3953, July 2001.

[20] Kalisko, M., and Rothert, H., 1997. "Formulation and Implementation of three-dimensional viscoelasticity at small and finite strains," Comput. Mechanics, Vol. 19, 1997, pp. 228–239.

[21] Lee, J., Kim, M. S., "A two-level parallel algorithm for material nonlinearity problems," Structural Engineering and Mechanics, Vol. 38, No. 4, 2011.

[22] Surzhikov, S. T., Krier, H., "Unsteady Dynamic Variables Method for Heterogeneous Solid Propellant Burning," AIAA Journal, Vol. 39, No. 12, Dec. 2001, pp. 2343 – 2350.

[23] Son, S. F., Brewster, M. Q., “Linear Burning Rate Dynamics of Solids Subjected to Pressure or External Radiant Heat Flux Oscillations,” Journal of Propulsion and Power, Vol. 9, No. 2, March-April 1993, pp. 222 – 232.

[24] L. D. Luca, E. W. Price, M. Summerfield, “Nonsteady Burning And Combustion Stability Of Solid Propellants,” AIAA progress series v143, 1992, ISBN-10: 1563470144

[25] E. W. Price, “Relevance of analytical models for perturbation of combustion of solid propellants,” AIAA Journal, Vol. 7, No. 1,1969, pp. 153-154

[26] R. L. Glick, “Heterogeneous propellant internal ballistics: criticism and regeneration,” Progress in Propulsion Physics, Volume 2, 2011, pp. 35-58

[27] T. L. Jackson and J. Buckmaster. "Heterogeneous Propellant Combustion", AIAA Journal, Vol. 40, No. 6 (2002), pp.1122-1130.

[28] S. N. Lee, S. W. Baek, and K. M. Kim, "Numerical Analysis of Quasi-Steady-Combustion Characteristics in a Solid Rocket Motor", Journal of Propulsion and Power, Vol.26, No.5, pp.980~986, 2010

[29] Lowe, C., “CFD Modeling of Solid Propellant Ignition,” Ph.D. Dissertation, College of Aeronautics, Cranfield Univ., Cranfield, UK, 1996.

[30] Marilyn, J. S., Dewey, H. H., and Carlos E.S.C., “Evaluation of Computational Algorithms Suitable for Fluid-Structure Interactions,” Journal of Aircraft, vol. 37, 2000, pp. 282–294.

[31] Jiao, X. and Heath, T. M, “Common-refinement-based data transfer between non-matching meshes in multiphysics simulations,” Int. J. Numer. Meth. Engng, Vol. 61, 2004, pp. 2402–2427.

[32] Jaiman, X. K., Jiao, X., Geubelle, P.H., and Loth, E., “Conservative load transfer along curved fluid-solid interface with non-matching meshes,” J. comput. phys, Vol. 218, 2006, pp.372–397.

[33] Park, K. C. and Felippa, C. A., “Partitioned transient analysis procedures for coupled-fields problems: accuracy analysis”, J. applied mechanics, Vol. 47, 1980, pp.919–926.

[34] Farhat, C., Lesoinne, M., “Two efficient staggered algorithms for the serial and parallel solution of three-dimensional nonlinear transient aeroelastic problems,” Comput.Methods Appl. Mech. Engrg, Vol. 182, 2000, pp.499–515.

[35] Rebay, S., “Efficient unstructured mesh generation by means of Delaunay triangulation and Boyer-Watson algorithm,” J. Comput. Phys., Vol. 106, 1993, pp.125–138.

[36] Baker, T. J., “Three dimensional mesh generation by triangulation of arbitrary point sets,” AIAA Paper 87-1124, 1987.

[37] Liu, X, Qin, N, Xia, H., “Fast dynamic grid deformation based on Delaunay graph mapping,” J. Comput. Phys., Vol 211, 2006, pp.405-423.

[38] Willcox, M. A., Brewster, M. Q., Tang, K. C., and Stewart, D. S., “Solid Propellant Grain Design and Burnback Simulation Using a Minimum Distance

Function," Journal of Propulsion and Power, Vol. 23, No. 2, March–April 2007, pp. 465–475.

[39] Nelson, H. C., Cunnigham, H. J., "Theoretical Investigation of Flutter of Two-Dimensional Flat Panels with One Surface Exposed to Supersonic Potential Flow," NACA Report No. 1280, 1956.

[40] Garrick, I. E., and Rubinow, S. I., "Flutter and Oscillating Air-Force Calculation for an Airfoil in a Two-Dimensional Supersonic Flow," NACA Rep. 846, 1946.

[41] Han, H., "A Study on the Thermal Response Characteristics of Carbon/Carbon Composites for Nozzle Throat Insert," Journal of the Korean Society of Propulsion Engineers, Vol. 10, No. 1, March 2006, pp.30-37

[42] Johnston, W. A., "A Numerical Procedure for the Analysis of the Internal Flow in a Solid Rocket Motor during the Ignition Transient Period," AIAA Paper 91-1655, 1991.

[43] Sanal Kumar, V. R., Raghinandan, B. N., Kim, H. D., Sameen, A., Setoguchi, T., and Raghunathan, S., "Starting Transient Flow Phenomena in Inert Simulators of SRMs with Divergent port," Journal of Propulsion and Power, Vol. 22, No, 5, Sept.-Oct.-Feb. 2006, pp.1138–1141.

[44] Spalart, P. R., Allmaras, S. R., "A one-equation turbulence model for aerodynamic flows," La Recherche Aerospatiale, Vol. 1, 1994, pp.5–21.

[45] Kumar, M., and Kuo, K. K., "Flame Spreading and Overall Ignition Transient," Fundamentals of Solid Propellant Combustion edited by K. K. Kuo and M. Summereld,

Vol.90, Progressing Astronautics and Aeronautics, AIAA, New York,1984, pp. 305–360.

[46] Caveny, L. H., Kuo, K. K., Shackelford, B. W., "Thrust and Ignition Transients of the Space Shuttle Solid Rocket Motor," J. Spacecraft, Vol. 17, No. 6, Nov.-Dec. 1980, pp.489-494.

[47] Sung-soo Kim, Chongam Kim, Oh-Hyun Rho, and Seung Kyu Hong, "Cures for the Shock Instability: Development of Shock-Stable Roe Scheme," *Journal of Computational Physics,* 2003. 2

[48] Belytschko T, Kennedy JM and Schoeberle DF. Quasi-Eulerian finite element formulation for fluid-structure interaction. J. Press. Vessel Technol.-Trans. ASME 1980; 102:62–69.

[49] Donea J, Fasoli-Stella P and Giuliani S. Lagrangian and Eulerian finite element techniques for transient fluid-structure interaction problems. In Trans. 4th Int. Conf. on Structural Mechanics in Reactor Technology, Paper B1/2, San Francisco, 1977.

[50] Pijaudier-Cabot G, Bod´e L and Huerta A. Arbitrary Lagrangian-Eulerian finite element analysis of strain localization in transient problems. Int. J. Numer. Methods Eng. 1995; 38(24): 4171–4191.

[51] Ponthot JP and Belytschko T. Arbitrary Lagrangian-Eulerian formulation for element-free Galerkin method. Comput. Methods Appl. Mech. Eng. 1998; 152(1–2):19–46.

[51] Donea J and Huerta A. Finite Element Methods for Flow Problems. Wiley: Chichester, 2003.

[52] Bonet J and Wood RD. Nonlinear Continuum Mechanics for Finite Element Analysis. Cambridge University Press: Cambridge, 1997.

[53] Noh WF. CEL:A time-dependent two-space dimensional coupled Eulerian-Lagrangian code. In Methods in Computational Physics, Alder B, Fernbach S and Rotenberg M (eds), vol. 3.Academic Press: New York, 1964; 117–179.

[54] Franck RM and Lazarus RB. Mixed Eulerian-Lagrangian method.In Methods in Computational Physics, Vol. 3: Fundamental methods in Hydrodynamics, Alder B, Fernbach S and Rotenberg M (eds). Academic Press: New York, 1964; 47–67.

[55] Trulio JG. Theory and Structure of the AFTON Codes. Report AFWL-TR-66-19, Air Force Weapons Laboratory: Kirtland Air Force Base, 1966.

[56] Hughes TJR, Liu WK and Zimmermann TK. Lagrangian-Eulerian finite element formulation for incompressible viscous flows. Comput. Methods Appl. Mech. Eng. 1981; 29(3):329–349; Presented at the U.S.-Japan conference on Interdisciplinary Finite Element Analysis, Cornell University, August 7–11, 1978.

[57] Wilcox D.C., “Turbulence modelling for CFD,” DCW Inc., 2002.

[58] M. Mooney. A theory of large elastic deformation. Journal of applied Physics, 11:582–a 592s, 1940.

[59] Geubelle, P. H., and Baylor, J., “Impact-induced delamination of composites: a 2-D simulation,” Composites B, Vol. 29, pp. 589-602, 1998.

[60] O. Rauna. Simulation de chocs dans les structures composites multicouches de révolution : Application à une structure sandwich tronconique de type adaptateur charge utile. CNAM, Paris, Juillet 2007.

[61] L. Afonso da Silva. Internal Variable and Temperature Modeling Behavior of Viscoelastic Structures - A Control Analysis. PhD thesis, Virginia Polytechnic Institute and State University, Blacksburg, Virginia, August 2003.

[62] Xueqiang Liu, Ning Qin, Hao Xia, “Fast dynamic grid deformation based on Delaunay graph mapping,” Journal of Computational Physics, Volume 211, Issue 2, 20 January 2006, Pages 405–423

[63] MESQUITE “Mesh Quality Improvement Toolkit User’s Guide”, The Sandia National Laboratories, http://software.sandia.gov/~jakraft/doc-2.1.4/users-guide.pdf

[64] Tong-Miin Liou and Wan-Yih Lien. "Numerical simulations of injection-driven flows in a two-dimensional nozzleless solid-rocket motor", Journal of Propulsion and Power, Vol. 11, No. 4 (1995), pp. 600-606.

[65] R. DUNLAP, P.G. WILLOUCHBY, and R.W. HERMSEN. "Flowfield in the Combustion Chamber of a Solid Propellant Rocket Motor", AIAA Journal, Vol. 12, No. 10 (1974), pp. 1440-1442.

[66] Tong-Miin Liou, Wan-Yih Lien, and Po-Wen Hwang. "Transition Characteristics of Flowfield in a Simulated Solid-Rocket Motor", Journal of Propulsion and Power, Vol. 14, No. 3 (1998), pp. 282-289.

[67] J. S. Sabnis, H. J. Gibeling, and H. Mcdonald. "Navier-Stokes analysis of solid propellant rocket motor internal flows", Journal of Propulsion and Power, Vol. 5, No. 6 (1989), pp. 657-664.

[68] Jayant S. Sabnis. "Numerical Simulation of Distributed Combustion in Solid Rocket Motors with Metalized Propellant", Journal of Propulsion and Power, Vol. 19, No. 1 (2003), pp. 48-55.

[69] R. Dunlap, A. M. Blackner, R. C. Waugh, R. S. Brown, and P. G. Willoughby. "Internal flow field studies in a simulated cylindrical port rocket chamber", Journal of Propulsion and Power, Vol. 6, No. 6 (1990), pp. 690-704.

[70] Bono Wasistho and R. D. Moser. "Simulation Strategy of Turbulent Internal Flow in Solid Rocket Motor", Journal of Propulsion and Power, Vol. 21, No. 2 (2005), pp. 251-263.

[71] Smith, T. M.; Roach, R. L.; Flandro, G. A., “Numerical study of the unsteady flow in a simulated solid rocket motor,” AIAA, Aerospace Sciences Meeting and Exhibit, 31st, Reno, NV, Jan. 11-14, 1993.

[72] Venugopal Prem, “Direct numerical simulation of turbulence in a model solid rocket motor,” ProQuest Dissertations And Theses; Thesis (Ph.D.)--University of Illinois at Urbana-Champaign, 2003.

[73] L. H. Caveny, K. Kuo, and B. W. Shackelford. "Thrust and ignition transients of the Space Shuttle solid rocket motor", Journal of Spacecraft and Rockets, Vol. 17, No. 6 (1980), pp. 489-494.

[74] D. Couton, F. Plourde, and S. Doan-Kim. "Cold gas simulation of a solid propellant rocket motor", AIAA Journal, Vol. 34, No. 12 (1996), pp. 2514-2522.

[75] Jiri Blazek, “Flow Simulation in Solid Rocket Motors Using Advanced CFD,” 39th AIAA/ASME/SAE/ASEE joint propulsion conference and exhibit, 20-23, July, 2003.

국문 초록

고체 추진제 방식의 로켓은 장기간 보관이 가능하고 즉각적인 사용이 가능하며 액체 로켓에 비해 상대적으로 신뢰성이 우수하여 군사 및 우주 추진체의 보조 로켓으로 주로 사용되고 있다. 하지만 능동적인 추력 제어가 어렵다는 단점을 갖고 있는 고체 로켓의 특성 상 추진제 자체의 연소 특성 및 연소실 내의 물리 현상을 파악하는 것은 고체 추진 로켓의 개발 및 운영에 있어서 매우 중요한 문제이다. 고체 로켓 연소실은 추진제 연소에 의한 고온, 고압의 연소 가스 발생과 유동 압력에 의한 추진제 그레인의 구조 변형 등 예측하기 어려운 매우 복잡한 물리 현상을 갖는다. 그리고 각 물리적 현상들은 서로에게 영향을 끼치기 때문에 유체나 구조만의 단일해석으로는 실제 현상을 예측하는데 있어 많은 제약이 따른다. 그리고 지상 연소 실험을 통한 현상 파악은 비용이 많이 들고 폭발의 위험이 있으며 연구자가 필요로 하는 물리량을 특정하여 정보를 획득함에 있어 많은 제약이 있다. 본 연구는 앞서 언급된 연구 방법의 단점을 보완하기 위한 방법의 일환으로 고체 추진 로켓 내부 연소실 내부 해석을 위한 유체-구조-연소 연동 해석을 목적으로 한다.

본 연구의 적용 대상인 고체 로켓 내부 연소실은 고체 추진제의 연소 및 유동압력에 의한 구조 변형으로 인해 의해 유동 영역과 구조 영역이 지속적으로 변화하게 된다. 그러므로 전산 해석에 있어서 영역 변화에 대응할 수 있는 기법이 필요하다. 본 연구에서는 ALE 기법을 적용하여 유동 해석 및 구조 해석에 있어서 해석 영역의 체적 변화를 모사하도록 하였다. 그리고 유동-구조 연동 해석에 있어서 각 영역의 경계 면에서의 정보 전달 기법 및 영역 변화에 따른 자동 격자 재생성 기법에 관한 연구가 수행되었으며 추진제 연소 특성에 알맞은 연소 모델 및 연소 과정 중 그레인의 형상 변화

를 잘 모사할 수 있는 표면 격자 추적 기법을 개발 및 적용하였다. 각 기법들은 통합 해석을 위해 하나의 프로그램으로 연동되었으며 이를 이용하여 연소실 내부 현상 해석을 수행하여 연소실 내부의 복합 물리 현상 발달 과정을 파악하였고 이 결과를 기반으로 파이로젠형 점화기의 초기 점화 위치 결정 특성, 화염면 전파 지연 현상 및 2차 연소면 생성 등의 물리 현상을 설명한다.

……

주요어 : Solid propellant rocket, Fluid-structure interaction, Arbitrary Lagrangian-Eulerian method, Common-refinement data transfer,

학 번 : 2007-30203